JOURNAL OF PETROLOGY | VOLUME 55 | NUMBER 9 | PAGES 1865–1903 | 2014 | doi:10.1093/petrology/egu044

# Dynamics of Magma Mixing in Partially Crystallized Magma Chambers: Textural and Petrological Constraints from the Basal Complex of the Austurhorn Intrusion (SE Iceland)

**DANIEL WEIDENDORFER*, HANNES B. MATTSSON AND PETER ULMER**

DEPARTMENT OF EARTH SCIENCES, INSTITUTE OF GEOCHEMISTRY AND PETROLOGY, SWISS FEDERAL INSTITUTE OF TECHNOLOGY (ETH ZURICH), CLAUSIUSSTRASSE 25, 8092 ZURICH, SWITZERLAND

**RECEIVED JANUARY 15, 2013; ACCEPTED JULY 14, 2014**

*The Tertiary Austurhorn intrusive complex in SE Iceland represents an exhumed magma chamber that has recorded an extensive history of magma mixing and mingling. The basal part of the intrusion consists predominantly of granophyres that have been intensively and repeatedly intruded by more mafic magma. This association of granophyres, basic and hybrid rocks at Austurhorn is referred to in the literature as a 'net-veined' complex, but field relations suggest a much more complex emplacement history. Here we present petrological and physical constraints on the various processes that resulted in magma mixing and mingling and the formation of different generations of hybrid rocks at Austurhorn. The complexity of the mixing and mingling processes increases towards the inferred centre of the intrusion, where chaotic hybrid rocks dominate the exposed lithology. Complex cross-cutting relations between different hybrid generations strongly suggest multiple magma injection and reheating events in the basal part of the shallow magma chamber. Model calculations employing distribution coefficients based on rare earth element concentrations reveal that early stage hybrid magma generations formed by pure endmember mixing between felsic and mafic magma with about 10% mafic fraction in the hybrids. With repeated injections of mafic magma into the base of the magma chamber, the intruding magma interacted to a greater extent with pre-existing hybrids. This led to the formation of hybrid magma compositions that are shifted towards the mafic endmember over time, with up to 30% of the mafic fraction in the hybrids. These mixing processes are recorded in the zonation patterns of clinopyroxene and plagioclase phenocrysts; the latter have been divided into four main groups by cross-correlation analysis. Melt viscosity calculations were performed to constrain the possible conditions of magma mixing and the results indicate that the interaction of the contrasting magmas most probably occurred at temperatures of approximately 1000°C up to 1120°C. This suggests that the initiation of effective magma mixing requires local superheating of the felsic magmas, thereby confining the process to areas of localized, substantial mafic magma injection.*

KEY WORDS: *magma mixing; hybridization; magma chamber dynamics*

## INTRODUCTION

Numerous examples of magma mixing and mingling are documented in exhumed magma reservoirs worldwide. It is evident from field observations that repeated injections may result in reheating and mobilization of partially crystallized mushes, a mechanism that is widely recognized and accepted to trigger volcanic eruptions (e.g. Sparks *et al.*, 1977; Eichelberger, 1995; Murphy *et al.*, 1998).

In the Tertiary North Atlantic Igneous Province many plutonic systems have been eroded to such an extent that the shallow magma chambers are now well exposed at the surface, allowing for detailed studies of magma chamber dynamics. A common feature in many of these exhumed magma reservoirs is the occurrence of 'net-veined'

*Corresponding author. Telephone: 0041446327819. Fax: 0041446321636. E-mail: daniel.weidendorfer@erdw.ethz.ch

complexes consisting of felsic, mafic and hybrid (intermediate) rocks (e.g. Wager & Bailey, 1953; Bailey & McCallien, 1956; Bailey, 1959; Elwell *et al.*, 1962; Wiebe, 1996; Kerr *et al.*, 1999; Preston, 2001). In Iceland several intrusive complexes occur on the eastern side of the island (i.e. in the oldest rocks that have been the most extensively eroded). The largest of these intrusions is the Austurhorn complex, located in southeastern Iceland (Fig. 1). As most active central volcanoes in Iceland typically erupt magmas of both silicic and basaltic composition (Jakobsson, 1979; Sæmundsson, 1979; Gunnarsson *et al.*, 1998; Lacasse *et al.*, 2007; Zellmer *et al.*, 2008), the Austurhorn complex has been interpreted to be analogous to the magmatic plumbing systems currently underlying the Eyjafjallajökull and Torfajökull volcanoes (Furman *et al.*, 1992b). Several recent studies of exhumed plutonic complexes have emphasized the importance of multidisciplinary approaches (such as combining detailed field studies with petrological and rheological modelling) to better understand the dynamics of incrementally formed, composite magma chambers (e.g. Turnbull *et al.*, 2010; Leuthold *et al.*, 2014). Because of the significant coastal erosion and glacial polishing of the exposed outcrops, detailed studies of the Austurhorn intrusion provide excellent three-dimensional insights into the physical and petrological processes occurring in the root zones of upper-crustal magma chambers. The relatively high cooling rates within shallow intrusions allow for reconstruction of the emplacement dynamics of single magma batches into a larger host reservoir (Sisson *et al.*, 1996; Leuthold *et al.*, 2014). Thus, the exposed root zone of the Austurhorn intrusion represents a 'snapshot' of the inner workings of a bimodal

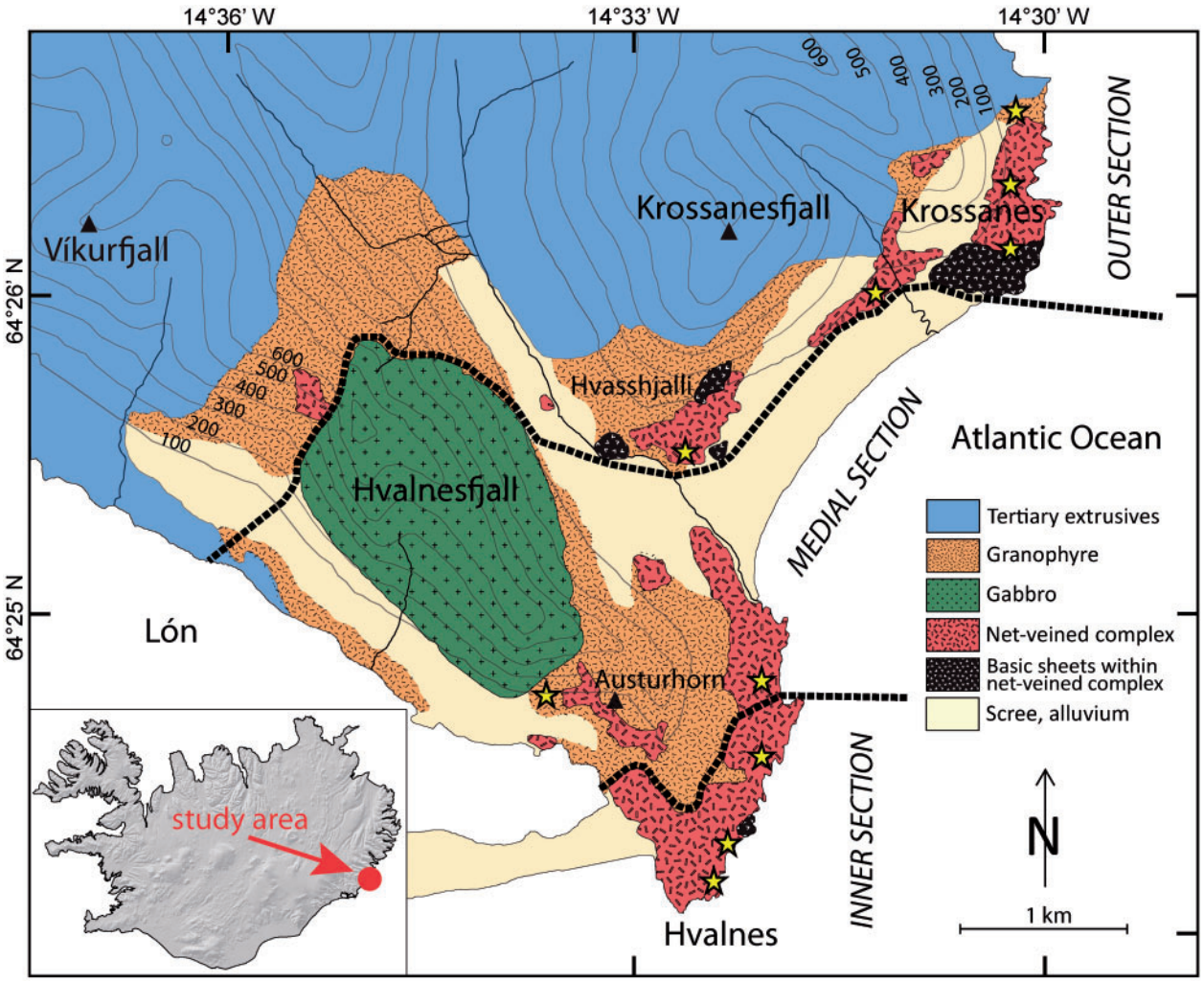


**Fig. 1.** Geological map of the Austurhorn intrusion in SE Iceland (after Blake, 1966). The Hvalnesfjall gabbro crops out in the western part of the intrusion and is entirely surrounded by granophyre. The 'net-veined' complex is exposed along the coastline, with the best exposures around Hvalnes and localities south and east of Krossanesfjall. The intrusion is emplaced into Tertiary lava flows. Sample localities are shown by stars. The bold dotted lines indicate the division of the intrusion into outer, medial and inner sections.

magmatic system that has been frozen *in situ*. In this study we focus on the hybridization dynamics and the petrological aspects of magma mixing and mingling between two or more physically and chemically contrasting magmas. We combine new field observations with geochemical data and petrological modelling to constrain these processes. Specifically, we apply distribution coefficient calculations and statistics to elucidate the petrogenetic relationship between partially crystallized felsic magmas, small-volume intrusions of basaltic composition and the hybrid magmas. We place particular emphasis on the zonation patterns in plagioclase crystals as these are well known to record complex magmatic growth dynamics within open-system magma reservoirs (Ginibre *et al.*, 2007; Streck, 2008).

Finally, based on the petrological and geochemical results, we combine MELTS calculations to constrain crystallinity–temperature relationships with viscosity calculations to delimit the rheological relationships between the magmas involved and to constrain the emplacement depth and the potential temperature window in which hybrid magmas are likely to have formed within the root zone of the Austurhorn intrusion. Although we are focusing on only the Austurhorn intrusion here, our results are likely to have much broader geological implications. We expect the physical processes and the mixing dynamics to be independent of geological setting or age, as long as two (or more) magmas with different chemical and physical properties interact inside crustal reservoirs.

## GEOLOGICAL SETTING AND PREVIOUS WORK

The coexistence of gabbros and granophyres in southeastern Iceland has been known for a long time and these occurrences have been described by several researchers (e.g. Thoroddsen, 1896; Cargill *et al.*, 1928; Anderson, 1949; Jónsson, 1954; Walker, 1964; Blake, 1966; Mattson *et al.*, 1986; Furman *et al.*, 1992a,b). The Austurhorn intrusive complex covers an area of ~11 km$^2$ along the northeastern coast of Lónsfjörður in SE Iceland (Fig. 1). It consists of layered gabbros, granophyre sheets and felsic to basaltic dikes and sills, which have been interpreted to be from a stock-like intrusion with a composite 'net-veined' complex consisting of felsic, mafic and hybrid (intermediate) rocks (Blake, 1964, 1966; Blake *et al.*, 1965; Mattson *et al.*, 1986; Furman *et al.*, 1992a,b). The country rocks surrounding the intrusion are predominantly westward dipping (6–10°; Walker, 1963) Tertiary lava flows. A contact metamorphic aureole (~1 km wide) surrounds the Austurhorn intrusion characterized by minerals such as epidote, chlorite, calcite, quartz and alkali feldspar with minor scolecite, mesolite, actinolite, garnet and prehnite (Blake, 1966). Recent U–Pb zircon age determinations (Martin *et al.*, 2011) of granophyre and gabbro at Austurhorn have yielded ages of 6·6 ± 0·4 Ma and 6·5 ± 0·2 Ma respectively. These confirm the Tertiary age of the intrusion, previously suggested on the basis of K–Ar dating of biotite (i.e. 6·6 ± 0·4 Ma; Moorbath *et al.*, 1968).

The Austurhorn intrusion hosts the largest gabbro outcrop in Iceland, the Hvalnesfjall gabbro (~1·8 km$^3$; Fig. 1), which is composed of at least eight macro-rhythmic units over more than 800 m of exposed stratigraphy (Thorarinsson & Tegner, 2009). The gabbro body defines a bowl-like structure with layering dipping ~50° to the east in the northwestern part and ~35° to the NW in the southeastern sector (Thorarinsson & Tegner, 2009). In general, the intrusion has a subhorizontal roof and steep-sided walls (Furman *et al.*, 1992b). The exposed floor and wall-rocks of the Hvalnesfjall gabbro consist of granophyre and a felsic–mafic pillow complex (Fig. 1).

Granophyre is the dominant rock type in the basal part of the intrusion, which has later been intensively intruded by mafic sheets (of tholeiitic to transitional tholeiitic composition; Furman *et al.*, 1992a,b). In the northeastern part of the intrusion the contact between the granophyre and the country-rock is exposed (Fig. 1). Along the coast from Krossanes to Hvalnes (Fig. 1) several mafic sheets intrude the granophyres and form the so-called 'net-veined' complex. This bimodal complex is more dominant in the eastern part of the intrusion (Fig. 1), whereas outcrops around the Hvalnes lighthouse in the south are characterized by intensive mixing and mingling features and the occurrence of several hybrid rock generations.

In general, the basal complex (including a variety of mingling and mixing features) forms ~30–40% of the Austurhorn intrusion (Blake, 1966). It is most commonly exposed along the margins of the intrusion but several potential contacts may also be hidden by large scree slopes that have developed below the granophyre and gabbro exposures along the Krossanesfjall and Austurhorn ridge (Fig. 1). Overall, the 'net-veined' complex at Austurhorn covers an area of more than 3 km$^2$ and consists of angular clasts, pillows and tabular masses of basaltic composition embedded within a granophyric host (Furman *et al.*, 1992b). In addition to massive sills of granophyre the 'net-veined' complex is also characterized by numerous felsic dykes that cross-cut the mafic sheets and pillows (Fig. 2a and b). Furman *et al.* (1992b) described no fewer than 16 felsic units within the coastal complex displaying brittle or ductile deformation that those researchers used as an indicator of their relative time of emplacement.

Based on the occurrence of distinct zeolite-rich horizons in the Tertiary lava pile in eastern Iceland (Walker, 1960) some indirect constraints on the emplacement depth of the Austurhorn intrusion can be provided. The top of the laumontite zone lies ~1700 m below the original top of the lava pile in this area (Walker, 1974, 1975). In olivine tholeiite

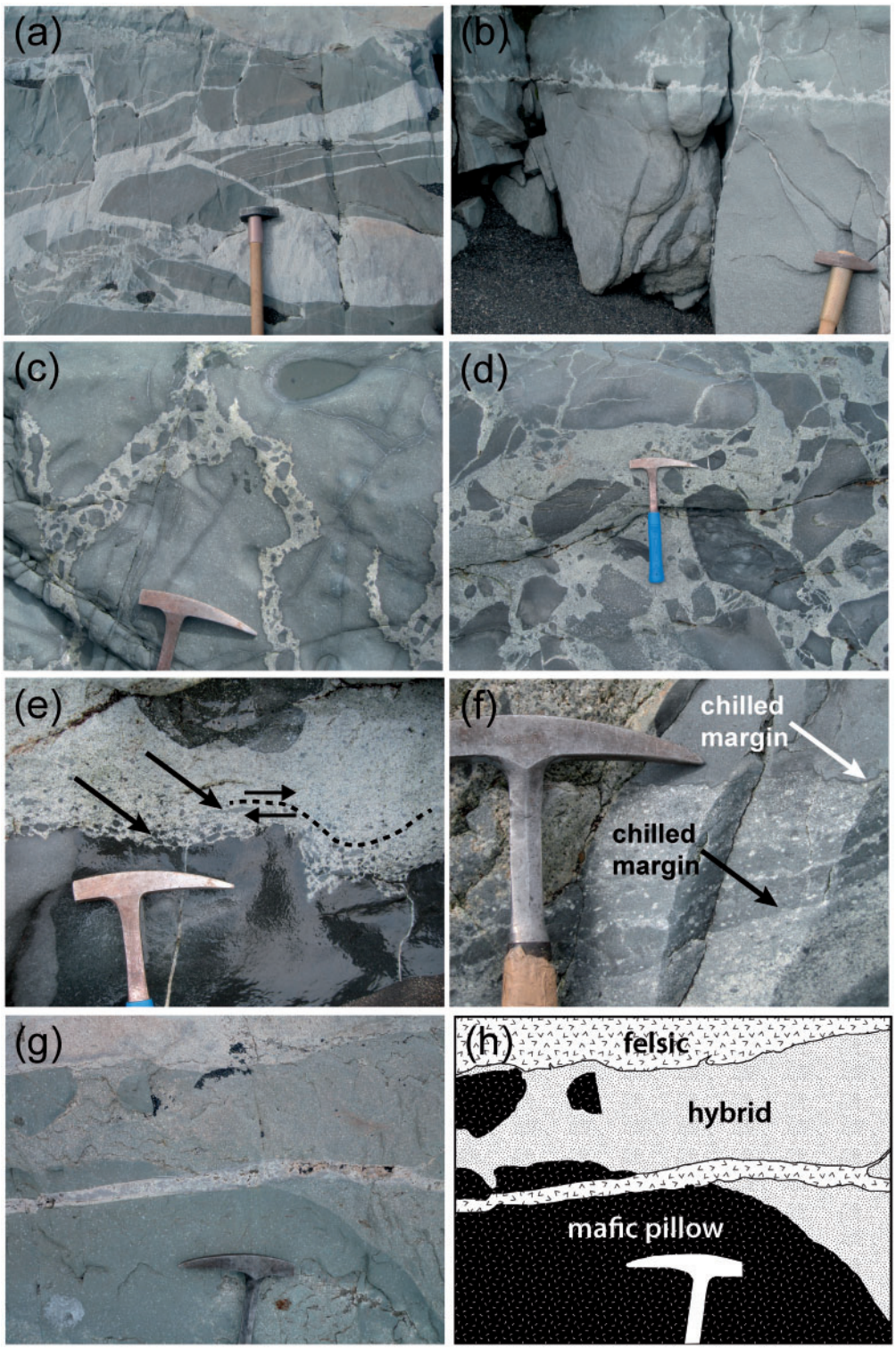


**Fig. 2.** Representative field photographs showing the variability of the outcrops within the Austurhorn intrusion. (a) Angular mafic blocks separated by felsic material south of Krossanesfjall. (b) Viscous fingering (flame structures) of felsic into mafic rocks (south of Krossanesfjall). (c) Mafic pillows separated from each other by a hybrid crystal mush containing mafic clasts. (d) Rounded to angular mafic fragments contained in a hybrid matrix. (e) Intra-magmatic shear zones generating extensive stretching of mafic enclaves. (f) Mafic layers separated from a pillow by hybrid layers. (g) Relationship between mafic pillow (bottom), hybrid (centre) and felsic rocks (top). A small felsic dike cross-cuts the hybrid and mafic rocks. (h) Sketch of (g).

lavas at Vikurfjall, located outside the thermal aureole of Austurhorn (Fig. 1), the top of the laumontite zone is located at ~750 m above sea level (a.s.l.). This height is equivalent to the highest exposure of the Austurhorn intrusion and, therefore, suggests an emplacement depth of ~1700 m for the intrusion (Walker, 1964; Blake, 1966).

## ANALYTICAL METHODS

A total of 65 whole-rock samples from different parts of the 'net-veined' complex of the Austurhorn intrusion were analysed for major elements by X-ray fluorescence spectrometry (XRF). All samples were crushed and milled to a fine powder using a hydraulic ram equipped with a stainless steel crushing cast and an agate disc mill. Dried powders were heated to 950–1050°C for 2 h and then mixed with lithium tetraborate and fused in a Claisse fluxer to glass beads. The loss of ignition (LOI) of the analysed samples ranges from −0·1 to 4·7 wt % with an average of 0·8 wt %. Glass beads were analysed using a Panalytical Axios wavelength-dispersive XRF system for 10 major and 21 trace elements. Calibration of the spectrometer is based on 32 certified standards.

Based on the compositional variability established by XRF analysis, 38 rock samples were analysed for trace elements using laser ablation inductively coupled plasma mass spectrometry (LA-ICP-MS) on broken pieces of the glass beads prepared for XRF analysis. The LA-ICP-MS system consists of a 193 nm wavelength ArF excimer prototype similar to GeoLas (Coherent) coupled to an Elan 6100 DRC (Perkin Elmer). For calibration NIST standard 610 was employed. The diameter of the laser aperture during standard and sample ablation was set to 40 μm and 90 μm respectively. Three replicate analyses were made on each sample, avoiding original surfaces of the glass bead and to minimize contamination. Acquired raw data from the LA-ICP-MS analyses were processed with SILLS (Signal Integration for Laboratory Laser Systems; Guillong *et al.*, 2008). Representative major and trace element analyses are given in Table 1 and in the Supplementary Data (supplementary data are available for downloading at http://www.petrology.oxfordjournals.org).

Approximately 240 representative crystals (comprising plagioclase, pyroxene, amphibole and Fe–Ti oxide phases) were selected for electron microprobe analysis. The analyses were performed with a JEOL JXA 8200 microprobe analyzer, with peak counting times of 20 s (except 40 s for Na) and a background time of 10 s (20 s for Na). Acceleration voltage was set to 15 kV and a beam current of 20 nA was used for all analyses. Calibration was based on the following standards: wollastonite (Si, Ca), periclase (Mg), corundum (Al), aegirine (Na), fayalite (Fe), rutile (Ti), pyrolusite (Mn), fluor-apatite (P) and alkali feldspar (K).

The characteristic morphologies of mixed and/or mingled magma interfaces were studied in the field, hand specimen, thin section and with a scanning electron microscope (JEOL JSM-6390 LA) operated at an acceleration voltage of 15 kV.

Melt viscosities for 38 rock samples were computed using the melt viscosity model of Giordano *et al.* (2008) in a temperature range from 700 to 1200°C with 50°C increments. All bulk-rock analyses from this study are within the calibrated compositional range of the viscosity model. To find the best fitting temperature window for mixing between felsic and mafic magmas as well as between the inferred endmembers and the hybrid compositions, the liquidus temperatures, liquid compositions and crystal fractions as a function of temperature were computed using MELTS (Ghiorso & Sack, 1995; Asimow & Ghiorso, 1998) and Rhyolite-MELTS (Gualda *et al.*, 2011), respectively. The changing melt composition during crystallization was then used for melt viscosity calculations using the model of Giordano *et al.* (2008). The effective viscosities of the crystal-bearing magmas were determined by applying the modified Einstein–Roscoe equation (Marsh, 1981).

To statistically identify and group various plagioclase phenocrysts from different hybrid generations we applied cross-correlation calculations using a computational raw correlation code in MATLAB 7.11. Plagioclase zonation profiles were first analysed by electron microprobe and then cross-correlated using the MATLAB algorithm. To avoid a subjective or 'pre-defined' grouping of different plagioclase phenocrysts, the cross-correlation calculations were achieved by a non-systematic correlation of all observed zonation patterns with each other. Within a group of similar crystal zonation patterns one phenocryst was randomly selected as a reference zonation pattern to subsequently discriminate between different generations of plagioclase populations.

## FIELD RELATIONSHIPS

The physical appearance of the 'net-veined' complex at Austurhorn varies substantially with location. Here we summarize the main characteristics of the outer, medial and inner sections of the intrusion (Fig. 1). In general, the complexity of the mingling and mixing features increases towards the internal parts of the intrusion (i.e. towards Hvalnes).

### Outer section

The outer part of the intrusion is predominantly characterized by brittle deformation indicated by the presence of angular mafic enclaves that are separated from each other by granophyric veins (Fig. 2a). The mafic clasts appear to have been formed by an *in situ* shattering mechanism similar to hydro-fracturing. At the contact of the intrusion

*Table 1: Representative major and trace element compositions of felsic, mafic and hybrid rocks from the 'net-veined' complex*

| Rock type: | felsic | felsic | mafic | mafic | hybrid mafic | hybrid mafic | mafic pillow | mafic pillow |
|---|---|---|---|---|---|---|---|---|
| Sample: | A5-8/a | A5-2 | A4-1 | A1-2 | A7-12/c | A5-8/b | A7-11/2 | A7-25/b |
| $SiO_2$ (wt %) | 71·49 | 73·70 | 45·88 | 46·93 | 53·64 | 52·17 | 53·35 | 47·04 |
| $TiO_2$ | 0·27 | 0·22 | 1·79 | 3·62 | 2·27 | 2·17 | 2·84 | 3·63 |
| $Al_2O_3$ | 13·44 | 13·45 | 19·51 | 12·57 | 13·57 | 15·25 | 13·50 | 12·44 |
| $Fe_2O_3$ | 2·82 | 2·24 | 9·85 | 15·95 | 11·63 | 10·99 | 12·51 | 17·17 |
| MnO | 0·06 | 0·03 | 0·15 | 0·28 | 0·18 | 0·18 | 0·24 | 0·34 |
| MgO | 0·18 | 0·12 | 6·30 | 4·78 | 4·23 | 4·80 | 3·67 | 4·74 |
| CaO | 1·53 | 0·31 | 12·12 | 8·99 | 7·71 | 8·08 | 7·32 | 8·88 |
| $Na_2O$ | 5·47 | 4·61 | 2·20 | 4·10 | 4·22 | 3·55 | 4·31 | 3·81 |
| $K_2O$ | 2·95 | 4·67 | 0·41 | 1·45 | 1·53 | 1·58 | 1·44 | 1·64 |
| $P_2O_5$ | 0·03 | 0·02 | 0·22 | 0·53 | 0·36 | 0·25 | 0·36 | 0·39 |
| LOI | 1·04 | 0·58 | 1·82 | 0·82 | 0·94 | 1·01 | 0·40 | –0·11 |
| Total | 99·27 | 99·95 | 100·27 | 100·02 | 100·29 | 100·04 | 99·95 | 100·00 |
| Mg# | 11·41 | 9·61 | 55·86 | 37·24 | 41·87 | 46·40 | 36·72 | 35·36 |
| V (ppm) | 6·2 | 5·4 | 175·6 | 336·6 | 233·8 | 221·3 | 248·7 | 394·2 |
| Cr | – | 14·9 | 82·8 | 13·2 | 55·5 | 72·9 | 21·5 | 20·8 |
| Ni | 6·4 | 9·5 | 82·7 | 36·9 | 26·7 | 43·9 | 15·5 | 29·0 |
| Sc | 2·2 | 1·4 | 19·4 | 29·2 | 23·5 | 19·7 | 19·7 | 31·4 |
| Rb | 37·2 | 58·5 | 5·0 | 44·1 | 30·9 | 39·7 | 22·8 | 62·9 |
| Sr | 81·7 | 44·6 | 442·4 | 361·3 | 297·0 | 291·3 | 258·9 | 286·7 |
| Y | 81·6 | 92·0 | 18·6 | 47·7 | 50·3 | 35·3 | 57·3 | 35·9 |
| Zr | 528·0 | 434·1 | 106·2 | 239·2 | 308·5 | 232·0 | 272·9 | 190·3 |
| Nb | 58·8 | 63·5 | 10·2 | 25·2 | 22·9 | 21·2 | 45·8 | 19·6 |
| Cs | 0·1 | 0·2 | 0·1 | 1·8 | 0·4 | 1·4 | 0·4 | 1·6 |
| Ba | 576·2 | 565·5 | 101·2 | 196·4 | 258·3 | 247·7 | 306·2 | 215·6 |
| La | 61·8 | 111·6 | 9·6 | 23·7 | 28·9 | 23·6 | 31·8 | 18·5 |
| Ce | 132·9 | 233·0 | 22·4 | 62·4 | 66·0 | 53·3 | 77·3 | 43·1 |
| Pr | 16·1 | 27·8 | 3·1 | 8·9 | 8·7 | 6·9 | 10·1 | 6·1 |
| Nd | 69·4 | 113·1 | 14·9 | 42·2 | 39·4 | 29·9 | 45·9 | 28·7 |
| Sm | 14·9 | 21·9 | 4·0 | 10·7 | 10·2 | 7·1 | 11·5 | 7·6 |
| Eu | 2·4 | 2·2 | 1·5 | 2·8 | 2·8 | 1·9 | 2·8 | 2·5 |
| Gd | 15·2 | 20·1 | 4·0 | 11·5 | 10·8 | 7·8 | 11·6 | 8·0 |
| Tb | 2·3 | 2·9 | 0·6 | 1·6 | 1·6 | 1·1 | 1·9 | 1·2 |
| Dy | 15·1 | 19·0 | 3·5 | 10·6 | 10·1 | 7·1 | 11·4 | 7·5 |
| Ho | 2·8 | 3·5 | 0·7 | 1·8 | 1·9 | 1·3 | 2·2 | 1·3 |
| Er | 9·0 | 9·3 | 2·0 | 5·0 | 5·6 | 3·6 | 6·3 | 3·7 |
| Tm | 1·2 | 1·3 | 0·2 | 0·7 | 0·7 | 0·5 | 0·8 | 0·5 |
| Yb | 8·4 | 8·0 | 1·5 | 4·0 | 4·3 | 3·1 | 5·4 | 3·0 |
| Lu | 1·1 | 1·2 | 0·2 | 0·6 | 0·6 | 0·4 | 0·7 | 0·4 |
| Hf | 13·2 | 13·5 | 2·8 | 6·4 | 8·0 | 5·7 | 7·2 | 5·2 |
| Ta | 3·8 | 3·9 | 0·7 | 1·5 | 1·6 | 1·4 | 2·7 | 1·2 |
| Th | 7·1 | 11·0 | 0·6 | 1·5 | 2·9 | 2·6 | 1·9 | 1·4 |
| U | 2·2 | 2·5 | 0·2 | 0·7 | 0·9 | 0·8 | 0·8 | 0·6 |

(continued)

*Table 1: Continued*

| Rock type: | mafic pillow | mafic pillow | mafic pillow | hybrid | hybrid | hybrid | hybrid | hybrid | hybrid |
|---|---|---|---|---|---|---|---|---|---|
| Sample: | A7-24/3 | A5-9/a | A7-7/a | A7-4 | A7-17 | A7-11/1 | A5-7/1 | A7-14/c | A5-7/2 |
| $SiO_2$ (wt %) | 48·86 | 49·96 | 47·08 | 73·11 | 69·57 | 66·65 | 61·32 | 58·03 | 57·73 |
| $TiO_2$ | 2·76 | 2·85 | 2·57 | 0·26 | 0·38 | 0·65 | 1·69 | 2·08 | 1·66 |
| $Al_2O_3$ | 14·70 | 14·38 | 14·82 | 12·41 | 13·97 | 14·35 | 14·63 | 14·57 | 11·64 |
| $Fe_2O_3$ | 13·13 | 13·00 | 12·81 | 3·98 | 4·14 | 6·00 | 8·00 | 9·73 | 9·00 |
| MnO | 0·19 | 0·19 | 0·21 | 0·06 | 0·12 | 0·13 | 0·17 | 0·18 | 0·20 |
| MgO | 5·07 | 5·20 | 6·13 | 0·04 | 0·29 | 0·66 | 1·95 | 2·50 | 5·10 |
| CaO | 10·23 | 9·70 | 9·96 | 0·79 | 1·26 | 2·09 | 4·50 | 5·55 | 8·29 |
| $Na_2O$ | 3·38 | 3·34 | 3·29 | 6·57 | 5·17 | 5·35 | 5·06 | 4·45 | 3·85 |
| $K_2O$ | 1·13 | 1·03 | 0·94 | 2·32 | 3·97 | 3·61 | 2·08 | 2·03 | 1·76 |
| $P_2O_5$ | 0·29 | 0·35 | 0·29 | 0·02 | 0·05 | 0·10 | 0·26 | 0·45 | 0·18 |
| LOI | 0·23 | 0·29 | 1·69 | 0·24 | 0·81 | 0·41 | 0·38 | 0·63 | 0·33 |
| Total | 99·99 | 100·33 | 99·82 | 99·80 | 99·74 | 100·00 | 100·06 | 100·20 | 99·79 |
| Mg# | 43·32 | 44·20 | 48·67 | 1·76 | 12·35 | 17·99 | 32·52 | 33·77 | 52·85 |
| V (ppm) | 307·8 | 281·1 | 281·4 | – | 12·4 | 29·6 | 97·6 | 127·5 | 172·4 |
| Cr | 50·1 | 79·5 | 109·9 | – | 10·8 | 8·5 | 7·8 | 6·8 | 211·6 |
| Ni | 47·1 | 42·2 | 57·5 | 10·0 | 3·9 | 5·3 | 8·3 | 8·7 | 55·3 |
| Sc | 30·0 | 28·0 | 29·1 | 2·1 | 2·6 | 5·3 | 10·4 | 13·7 | 32·0 |
| Rb | 29·8 | 22·5 | 22·7 | 27·8 | 58·1 | 53·8 | 32·3 | 30·8 | 24·9 |
| Sr | 333·7 | 325·6 | 376·0 | 75·4 | 79·4 | 105·0 | 223·0 | 307·8 | 160·2 |
| Y | 30·6 | 34·6 | 27·6 | 88·0 | 81·7 | 114·2 | 65·7 | 62·6 | 79·5 |
| Zr | 191·6 | 192·4 | 146·9 | 717·3 | 722·0 | 1182·9 | 450·5 | 390·8 | 361·4 |
| Nb | 15·5 | 18·2 | 14·1 | 57·8 | 56·5 | 55·4 | 46·6 | 39·0 | 37·6 |
| Cs | 1·0 | 1·4 | 0·7 | 0·4 | 0·2 | 0·3 | 0·3 | 0·2 | 0·2 |
| Ba | 146·6 | 184·4 | 182·9 | 462·1 | 759·0 | 713·5 | 453·3 | 436·8 | 362·0 |
| La | 16·8 | 20·2 | 15·4 | 63·4 | 52·3 | 112·9 | 41·2 | 43·0 | 36·4 |
| Ce | 36·3 | 46·9 | 35·3 | 135·1 | 121·7 | 241·9 | 95·8 | 98·2 | 89·7 |
| Pr | 5·1 | 6·1 | 4·8 | 17·4 | 15·4 | 29·9 | 12·5 | 12·6 | 12·6 |
| Nd | 24·8 | 29·7 | 22·6 | 72·8 | 69·0 | 131·9 | 54·6 | 53·4 | 56·4 |
| Sm | 6·2 | 7·5 | 5·8 | 16·3 | 15·8 | 28·9 | 13·3 | 12·5 | 14·3 |
| Eu | 2·1 | 2·4 | 2·0 | 3·0 | 3·9 | 4·1 | 3·1 | 3·4 | 2·7 |
| Gd | 6·5 | 7·8 | 5·8 | 17·7 | 15·5 | 25·8 | 12·6 | 13·6 | 14·6 |
| Tb | 1·0 | 1·2 | 0·9 | 2·7 | 2·6 | 4·0 | 2·0 | 2·1 | 2·5 |
| Dy | 6·1 | 7·2 | 5·6 | 17·4 | 16·3 | 23·8 | 12·8 | 12·6 | 15·1 |
| Ho | 1·2 | 1·4 | 1·0 | 3·5 | 3·1 | 4·4 | 2·5 | 2·3 | 3·0 |
| Er | 3·3 | 3·9 | 3·1 | 10·0 | 8·1 | 12·7 | 6·9 | 6·7 | 8·5 |
| Tm | 0·4 | 0·4 | 0·4 | 1·4 | 1·2 | 1·8 | 1·0 | 0·9 | 1·1 |
| Yb | 2·7 | 3·3 | 2·3 | 8·8 | 8·2 | 12·1 | 5·4 | 5·6 | 7·8 |
| Lu | 0·3 | 0·5 | 0·3 | 1·2 | 1·1 | 1·7 | 0·9 | 0·8 | 1·1 |
| Hf | 5·1 | 5·9 | 3·9 | 19·0 | 17·0 | 29·4 | 11·1 | 10·2 | 9·4 |
| Ta | 1·1 | 1·5 | 1·0 | 3·8 | 3·3 | 3·9 | 3·3 | 2·9 | 2·6 |
| Th | 2·3 | 2·1 | 1·0 | 7·0 | 5·7 | 9·5 | 3·9 | 3·7 | 3·4 |
| U | 0·7 | 0·6 | 0·3 | 2·0 | 2·0 | 3·1 | 1·4 | 1·1 | 1·2 |

Major elements (wt %) analysed by XRF and trace elements (ppm) analysed by LA-ICP-MS; $Mg\# = 100\,Mg/(Mg + Fe^{2+})$, $Fe^{2+} = 0{\cdot}89Fe_2O_3$.

with the Tertiary lava flows brittle deformation is recorded by the presence of ~40 cm thick granophyre dikes truncating against near-horizontal country-rocks at oblique angles. Thus, at the time when the felsic magma intruded the basal complex of the Austurhorn magma chamber, the tholeiitic lava pile was already crystallized considerably below the rheologically critical melt fraction and most probably below the melt connectivity transition (Rosenberg & Handy, 2005) where the rocks behave in a brittle manner. The separation of angular mafic blocks by thin (>15 cm) granophyre veins represents the typical appearance of what is commonly referred to as a 'net-veined' complex in the literature (Fig. 2a). These outcrops exhibit only minor variation and they are mainly exposed along the outer part of the intrusion (from Krossanes to Hvasshjalli; Fig. 1). However, in close spatial relationship with the typical brittle appearance of the 'net-veined' complex we also observe 'flame structures' (Fig. 2b), indicating significant changes in the rheological properties of the two magmas over short distances. The flame structures are always associated with, or originate from, thin granophyre veins that cross-cut the internal layering of the mafic sheets.

## Medial section

Along the coast from Krossanes to the Hvalnes lighthouse an intimate association of rounded and angular mafic blocks embedded within a hybrid matrix (Fig. 2c and d) is observed. The complexity of the textural relations is considerably greater than in the outer section, indicating that the magma chamber dynamics and physical interactions between the magmas vary to a great extent, and can change significantly on a metre scale.

The exposures in the medial section are dominated by fine-grained to gabbroic pillows within a hybrid crystal mush. Some of the gabbroic pillows (up to 45 cm in diameter) display internal layering, with an alternating sequence of coarser- and finer-grained layers, as well as chilled pillow margins. Some fine-grained mafic pillows with chilled margins are surrounded by hybrid rocks displaying intra-magmatic shear zones (Fig. 2e). Along the contact zone between the chilled pillow surface and the hybrid matrix small rounded to elongated mafic enclaves mantle the outline of the pillow (Fig. 2e). On closer inspection, most of these enclaves show well-rounded shapes that become progressively stretched and elongated with increasing distance from the pillow rim (Fig. 2e). Another mechanism leading to incorporation of mafic material into felsic or hybrid magmas can be observed along the coast between Krossanes and Hvalnes. Figure 2f shows a mafic pillow, which is surrounded by two distinct mafic layers (3–5 cm thick) that were thermo-mechanically separated from the original main pillow surface by movement of a hybrid crystal mush. The outer surface of the lowermost mafic layer as well as the inferred, previously formed, pillow margin shows quench textures indicating a significant thermal gradient between the basaltic pillows and the hybrid matrix at the time of the shear-induced physical abrasion processes. As a result of this process these mafic layers of various thicknesses were incorporated into the hybrid crystal mush and became disintegrated owing to shearing dynamics within the hybridization zones.

A key difference between the features observed in the medial section and those of the outer section is the dynamic role of the felsic and/or hybrid matrix. Compared with *in situ* shattering processes generating angular mafic blocks within felsic magma, the hybrid and/or hybridized felsic matrix in the medial section acts as a transport medium (Fig. 2c and d).

## Inner section

Along the beach close to Hvalnes lighthouse (Fig. 1) several outcrops polished by glacial erosion and subsequent wave action are exposed. In one of these outcrops a relatively voluminous mafic sheet (~15 m in width) is emplaced into a granophyric host. Figure 3 illustrates the entire outcrop exposed at Hvalnes beach where felsic and mafic endmember rocks are separated by a zone consisting of several hybrid generations. The contact between the hybridized zone and the granophyre is diffuse (Fig. 3a), whereas different hybrid generations (Fig. 3b) are identified by cross-cutting relationships. The fact that hybrids are cut by other hybrid generations indicates complex emplacement dynamics and repeated injection events within the magma chamber. At the tip of the mafic sheet, pillow-like structures (Fig. 3c) are separated from the main body. The margins of the mafic pillows near the centre of the intrusive complex are not as strongly chilled as the pillow rims within the medial section, indicating reduced temperature gradients. A distinct feature can be observed in the diffuse pillows at Hvalnes beach, where single pillows are surrounded by a yellowish halo (Fig. 3c). In close spatial relation to the pillows produced by the mafic sheet there are small areas of sharply fractured, angular mafic clasts enclosed in felsic and hybrid rocks. Between the two endmembers angular to rounded mafic and felsic enclaves (Fig. 3d and e) are embedded within a phenocryst-rich hybrid matrix. Angular to sub-rounded mafic fragments constitute ~20% of the exposed hybridization zone (Fig. 3d). Felsic enclaves predominantly occur within the hybridized zone (Fig. 3e). These are rounded to slightly elongated and considerably coarser-grained than the pure granophyre endmember. The mafic enclaves range in size from centimetre to decimetre (Fig. 3f), whereas the felsic equivalents within the hybridization zone are generally larger.

Overall, the shapes of the mafic pillow margins vary with location within the intrusion. Rather sharp, chilled pillow margins characterize the outer parts of the

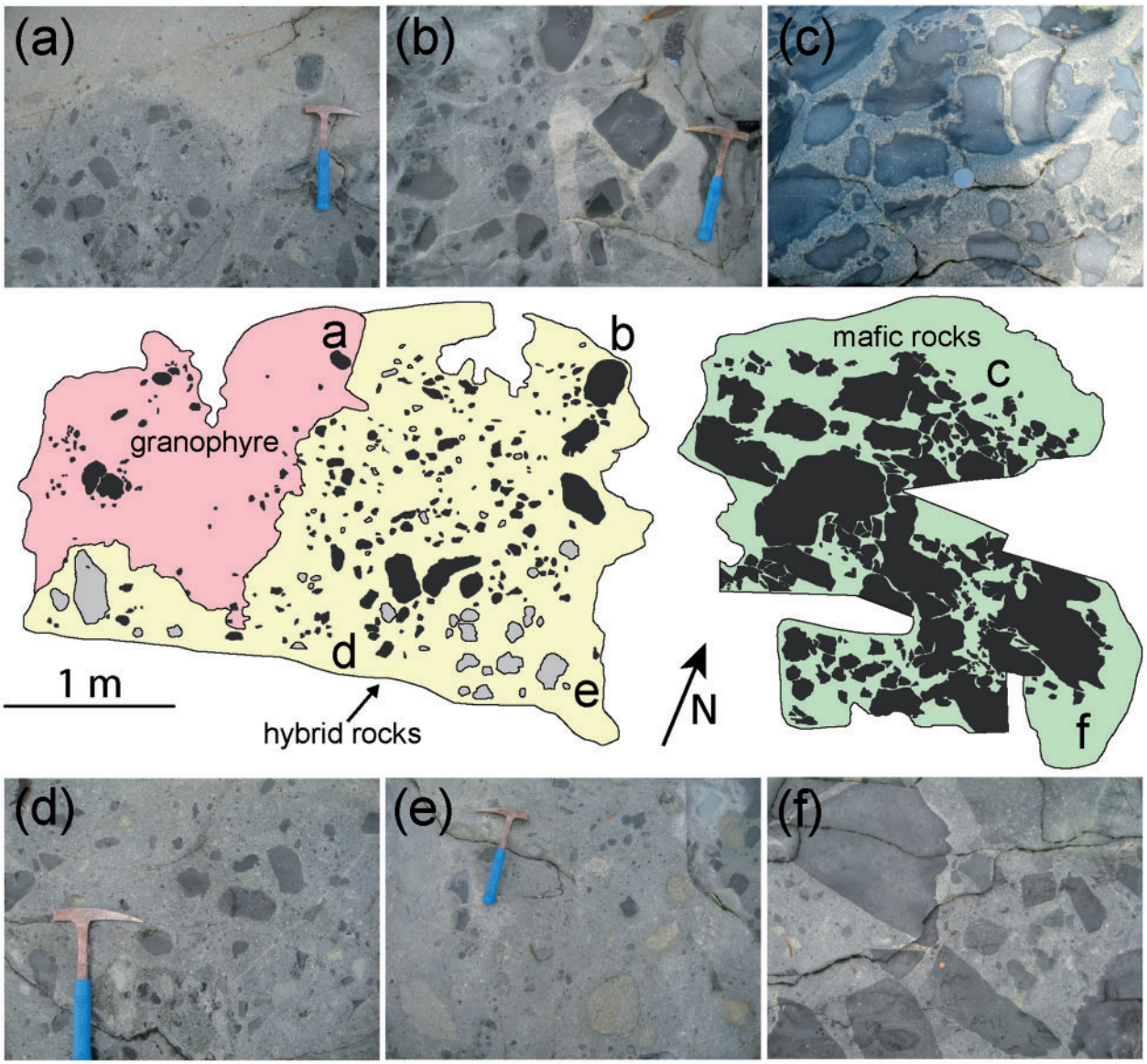


**Fig. 3.** Photographs of outcrops at Hvalnes beach. The digitized sketch illustrates the contact zone between the granophyre and the hybrid and that between the hybrid and the mafic rocks. Letters within the sketch indicate the locations of the photographs. The right-hand side of the sketch is dominated by mafic pillows and rounded to angular mafic fragments contained within a hybrid matrix. The mafic sheet from which the pillows originate is located ~3 m to the NE. Black objects represent mafic enclaves and grey objects are felsic enclaves. (a) Contact zone between the felsic endmember (granophyre) and hybrid rocks. At the position of the hammer, a sharp contact zone separates two hybrid generations. In this zone the felsic endmember appears affected by hybridization. (b) Cross-cutting relationships between hybrid generations. (c) Mafic pillows form at the tip of the mafic sheet that intrudes into the granophyre host. Pillows at Hvalnes beach are characterized by only weakly developed chilled margins and a yellowish halo. (d) Mafic enclaves close to the contact between the hybrid and granophyre rocks. (e) Felsic, coarse-grained enclaves are commonly well rounded compared with angular mafic fragments. (f) High variability of mafic enclave geometries indicates complex mixing and mingling dynamics.

intrusion, whereas pillows in the inner section are dominated by extensive fingering patterns and non-chilled rims.

## PETROGRAPHY

Each rock type within the 'net-veined' complex shows a broad variability in terms of texture and in the dominant mineral assemblage. Therefore, for the purpose of petrographic description, we divide the 'net-veined' complex into three main rock types, felsic, hybrid and mafic rocks, based on the following criteria: (1) felsic rocks consist of a phenocryst assemblage of alkali feldspar, plagioclase, quartz and minor amphibole, set in a typical micrographic intergrowth of quartz and alkali feldspar; (2) mafic rocks

exhibit an ophitic to hypidiomorphic–equigranular texture and consist of plagioclase, clinopyroxene, amphibole and Fe–Ti-oxides; (3) hybrid rocks are composed of both felsic and mafic mineral assemblages and exhibit substantial textural variability.

### Felsic rocks

The phenocryst assemblages of the felsic rocks are dominated by alkali feldspar, plagioclase, quartz, and amphibole ± biotite, with quartz and alkali feldspar typically exhibiting intergrowth textures. The groundmass consists of quartz, plagioclase and alkali feldspar ± biotite and amphibole. Zircon, apatite and Fe–Ti oxides occur as accessory phases. The graphic intergrowth texture is not characteristic of all granophyres at Austurhorn, but this texture clearly represents one of the main features of the felsic rocks (see Blake, 1966; Furman *et al.*, 1992a,b). Micrographic textures often occur at the rims of alkali feldspars, but there is also another population of large alkali feldspars, which lack quartz–feldspar intergrowths. Macroscopically, most of the granophyres have a reddish-pink colour and contain many small randomly distributed opaque phases. Many of the granophyres additionally exhibit abundant miarolitic cavities, which are occasionally filled with secondary minerals (e.g. quartz, alkali feldspar and epidote; Fig. 4a and b). Nearly all alkali feldspars are turbid and exhibit, together with plagioclase, strong alteration features along their crystal rims. Alkali feldspar in hypidiomorphic to equigranular granophyre dykes that cross-cut mafic sheets and pillows (Fig. 2g and h) are characterized by cross-hatched (tartan) twinning (typical of microcline) and the absence of quartz–alkali feldspar intergrowths. Plagioclase is commonly euhedral to subhedral in shape and is mantled with turbid and highly altered alkali feldspar (Fig. 4a and b). Plagioclase phenocrysts commonly show polysynthetic twinning as well as Carlsbad twins. In thin section, amphibole shows weak pleochroism with a colour change from green to brownish; minor biotite is predominantly associated with amphibole.

### Mafic rocks

Most mafic pillows, as well as some of the sampled mafic sheets, have ophitic to hypidiomorphic–equigranular textures and primarily consist of variable amounts of plagioclase, clinopyroxene, amphibole and Fe–Ti oxides. The matrix predominantly consists of pyroxene and plagioclase. Rare olivine crystals occur in a few of the mafic samples. Secondary alteration minerals include carbonate, pumpellyite, epidote and chlorite. Subhedral poikilitic pyroxenes frequently contain inclusions of tiny plagioclase laths that are often affected by late-stage alteration. In some cases clinopyroxene is replaced by amphibole. With the exception of a few subhedral amphiboles, the more abundant, anhedral crystals show intensive alteration with corroded crystal rims. Occasionally fibrous, short prismatic actinolite fills intergranular spaces between the different crystal assemblages (Fig. 4c–e). Plagioclase phenocrysts are euhedral to subhedral and characteristically display polysynthetic twinning and, more rarely, oscillatory zoning. Alkali feldspar is occasionally observed close to contacts with felsic dykes or along the peripheries of mafic pillows and exhibits skeletal intergrowth textures together with quartz. Mafic pillows are fine to medium grained; the grain size generally decreases from the pillow interior to the pillow margin. Close to contacts with hybrid rocks the amount of slightly elongated and radially aligned opaque phases significantly increases.

### Hybrid rocks

Hybrid rocks from the basal complex contain both felsic and mafic mineral phases, including alkali feldspar, plagioclase, clinopyroxene and amphibole in different modal proportions. Their matrix consists of equigranular quartz (up to 200 μm), alkali feldspar and plagioclase. Biotite, chlorite, epidote, zircon and pumpellyite, together with carbonate minerals, are minor phases. All investigated thin sections show evidence of intensive alteration and substantial textural variability in the different hybrid rocks. Graphic intergrowth of quartz and alkali feldspar is very common and sometimes occurs as small angular fragments within the hybrid matrix. Plagioclase phenocrysts commonly exhibit sieve textures and resorbed crystal rims, and are typically mantled by alkali feldspar (Fig. 4f–h). Alkali feldspar phenocrysts are considerably larger than plagioclase and often contain small albite inclusions that are different from perthite lamellae. Distinct mineral zonation patterns can be seen in plagioclase and clinopyroxene (Fig. 4f–h). The amount of Fe–Ti oxides in the hybrid rocks is considerably less than in the mafic rocks. Within the hybrid matrix relicts of mafic and/or felsic glomerophyric to poikilitic minerals are present. In contrast to the mafic rocks, amphiboles within the hybrid rocks are often intensely altered and frequently exhibit sieve textures.

## GEOCHEMISTRY

### Bulk-rock major elements and classification of the Austurhorn rocks

The rock classification scheme used in this study is based on geochemistry and comprises felsic endmembers, hybrid and mafic rocks; the latter two are further discriminated geochemically into subcategories. According to discrete mixing trends within the intermediate bulk-rock compositions, the hybrid rocks are separated into three groups, Intermediate (HybI), Evolved (HybE) and Primitive Hybrid (HybP) rocks. The mafic rocks are divided into five subgroups: mafic endmembers, mafic pillows, mafic enclaves, hybrid mafic pillows and hybrid mafic rocks.

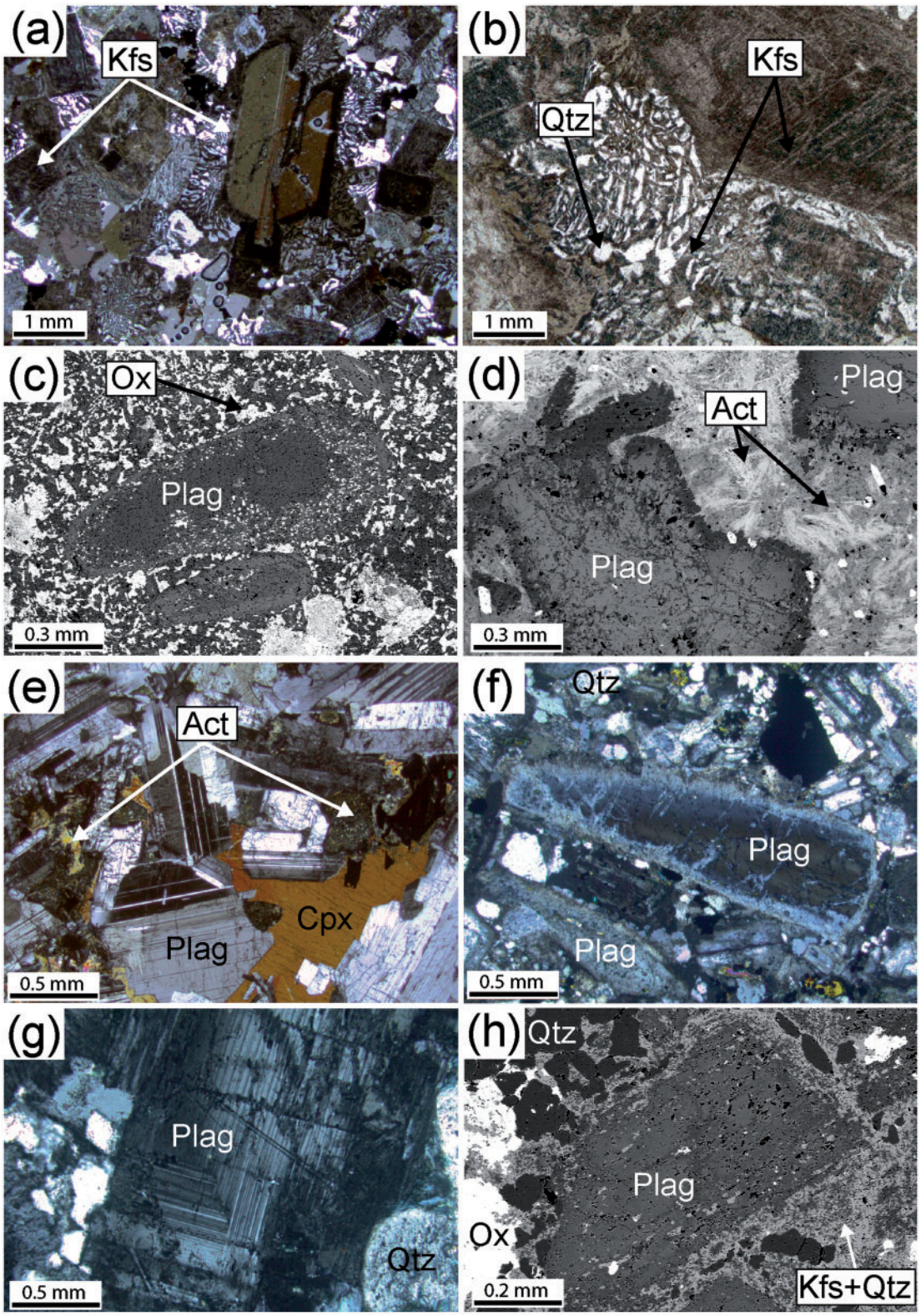


**Fig. 4.** Representative photomicrographs of textures in thin section. (a) Felsic rocks from the 'net-veined' complex at Hvalnes beach, which are identical to granophyre sills in the eastern part of the intrusion. (b) Graphic intergrowth of alkali feldspar and quartz in granophyre. (c) Back-scattered electron (BSE) image of a porphyritic mafic pillow. The matrix consists of plagioclase, clinopyroxene and Fe–Ti oxides. Plagioclase phenocrysts are euhedral to subhedral and may contain abundant small rounded magnetite grains between the crystal core and

(continued)

The compositional variability of the Austurhorn rocks is significant, with magnesium numbers (Mg#) ranging from 2 to 56, and $SiO_2$ from ~46 to 74 wt % (Table 1). In a total alkalis versus silica (TAS) diagram the suite of rocks defines a transitional alkaline–subalkaline trend (Fig. 5a) from basalt to trachydacite and rhyolite without any apparent compositional gap in the intermediate compositions. The peralkalinity index representing the molar ratio of $(K_2O + Na_2O)/Al_2O_3$ in the felsic rocks ranges from 0·9 to 0·97 (Fig. 5b). All the felsic rocks are metaluminous, with the exception of two felsic rock samples, which have an alumina index >1 and, therefore, are slightly peraluminous.

Major elements define curvilinear trends in Mg# variation diagrams (Fig. 5c–h). Especially in the mafic rocks, the oxide concentrations and the corresponding Mg# vary significantly and, thus, form the largest data spread within the entire Austurhorn rock series. The silica content increases in all rock types with decreasing Mg# (Fig. 5c). Hybrid rocks display the largest variability in $SiO_2$ content, varying from 58 to 73 wt % (Table 1). Within the felsic and hybrid rock groups, MnO and $P_2O_5$ (Fig. 5g and h) increase with increasing Mg#, whereas the mafic endmember rocks, hybrid mafic rocks and most of the mafic pillows show decreasing concentrations. Only five mafic pillow samples exhibit increasing MnO and $P_2O_5$ concentrations with increasing Mg# and, thus, follow the felsic–hybrid enrichment pattern; other mafic pillow samples exhibit trends that are nearly orthogonal to this 'hybridization' trend (Fig. 5). The same relationship with increasing Mg# as described for MnO and $P_2O_5$ is also true for $TiO_2$ and $Fe_2O_3$ (not shown). An overall increase in MgO, CaO, $Cr_2O_3$ and NiO with increasing Mg# is recorded throughout the series. Within both the felsic and mafic rock series $Al_2O_3$ increases with Mg#. Hybrid rocks exhibit slightly increasing $Al_2O_3$ contents until the Mg# exceeds 30; thereafter, hybrids show steadily decreasing $Al_2O_3$ concentrations with increasing Mg#. In all major element variation diagrams mafic endmember rock samples are aligned and form dominant curvilinear trends. The alkali contents $(Na_2O + K_2O)$ of the felsic rocks range from 8·4 to 9·3 wt %. Hybrid rocks display total alkali contents in the range of 5·6–9·5 wt % and in mafic rocks they range from 2·6 to 6·8 wt % (Fig 5a). The largest scatter in potassium concentrations is observed in felsic rocks (Fig. 5e) and low-Mg# hybrid rocks. Overall, $K_2O$ decreases with increasing Mg# throughout the entire Austurhorn rock series. $Na_2O$ concentrations (Fig. 5f) in felsic and hybrid rocks exceed 4 wt % and scatter considerably, but overall seem to level out at an Mg# less than about 35. The mafic rocks scatter much less in $Na_2O$ than $K_2O$ and show decreasing concentrations with increasing Mg# (Fig. 5f). On average, mafic endmember rocks from the basal complex have 3·1 wt % $Na_2O$ and 0·9 wt % $K_2O$ (Table 1), whereas the felsic endmember rocks contain average $Na_2O$ and $K_2O$ concentrations of 5·0 wt % and 3·9 wt %, respectively. Conspicuously, most hybrid rocks have higher $Na_2O$ concentrations than the 'pure' felsic and mafic endmember samples (Table 1).

Mafic pillows and some mafic endmember compositions exhibit increasing $P_2O_5$ concentrations with decreasing Mg#. An opposite trend of decreasing $P_2O_5$ with decreasing Mg# is recorded for nearly all hybrid rocks. One group of hybrid rocks does not follow the main trend and plots at constant, intermediate $P_2O_5$ concentrations at Mg# in the range of 30–40.

## Trace elements

Chondrite-normalized rare earth element (REE) patterns (Fig. 6) for felsic and mafic rocks exhibit decreasing concentrations from light (LREE) to heavy REE (HREE) as well as a clear separation between these endmember groups. The REE concentrations in the hybrid rocks lie between the felsic and mafic endmembers and are characterized by considerable internal variation (Fig. 6b and d). It is interesting to note that mafic pillows from the basal complex have REE concentrations that cover the range from mafic to almost felsic compositions (i.e. similar to the hybrid rocks). Chondrite-normalized $(La/Sm)_N$ in the felsic rocks ranges between 2·4 and 3·2 and is thus slightly higher than the values reported by Furman *et al.* (1992a). The hybrid rocks have $(La/Sm)_N$ values ranging from 1·6 to 2·9, whereas the mafic rocks have consistently lower values (between 1·4 and 2·1). $(Ce/Yb)_N$ for the felsic rocks ranges from 3·8 to 7·7, for hybrid samples from 3·1 to 5·6 and for mafic rocks from 3·5 to 4·7. All felsic and hybrid rocks have negative Eu anomalies (Fig. 6). These are most distinct in the felsic rocks and considerably smaller in the hybrid samples. Trace element patterns (Fig. 7) normalized to primitive mantle values reveal the strong resemblance between the felsic and hybrid rocks

**Fig. 4.** Continued
the Ca-rich crystal rim. (d) BSE image of plagioclase phenocrysts within a mafic rock matrix primarily consisting of clinopyroxene. Plagioclase has anorthite-rich cores and albitic rims (normal zoning). Actinolite forms needle-like short prismatic crystals and replaces altered clinopyroxene and hornblende. (e) Sample A4-1 from the mafic sheet at Hvalnes beach, showing late alteration products (actinolite) from the breakdown of clinopyroxene and hornblende. (f) Plagioclase within a hybrid rock showing a resorption rim that is evidence of disequilibrium. (g) Thin section photomicrograph of an oscillatory zoned plagioclase within a hybrid rock. (h) BSE image of hybrid plagioclase displaying a resorbed crystal rim and small inclusions of quartz and alkali feldspar.

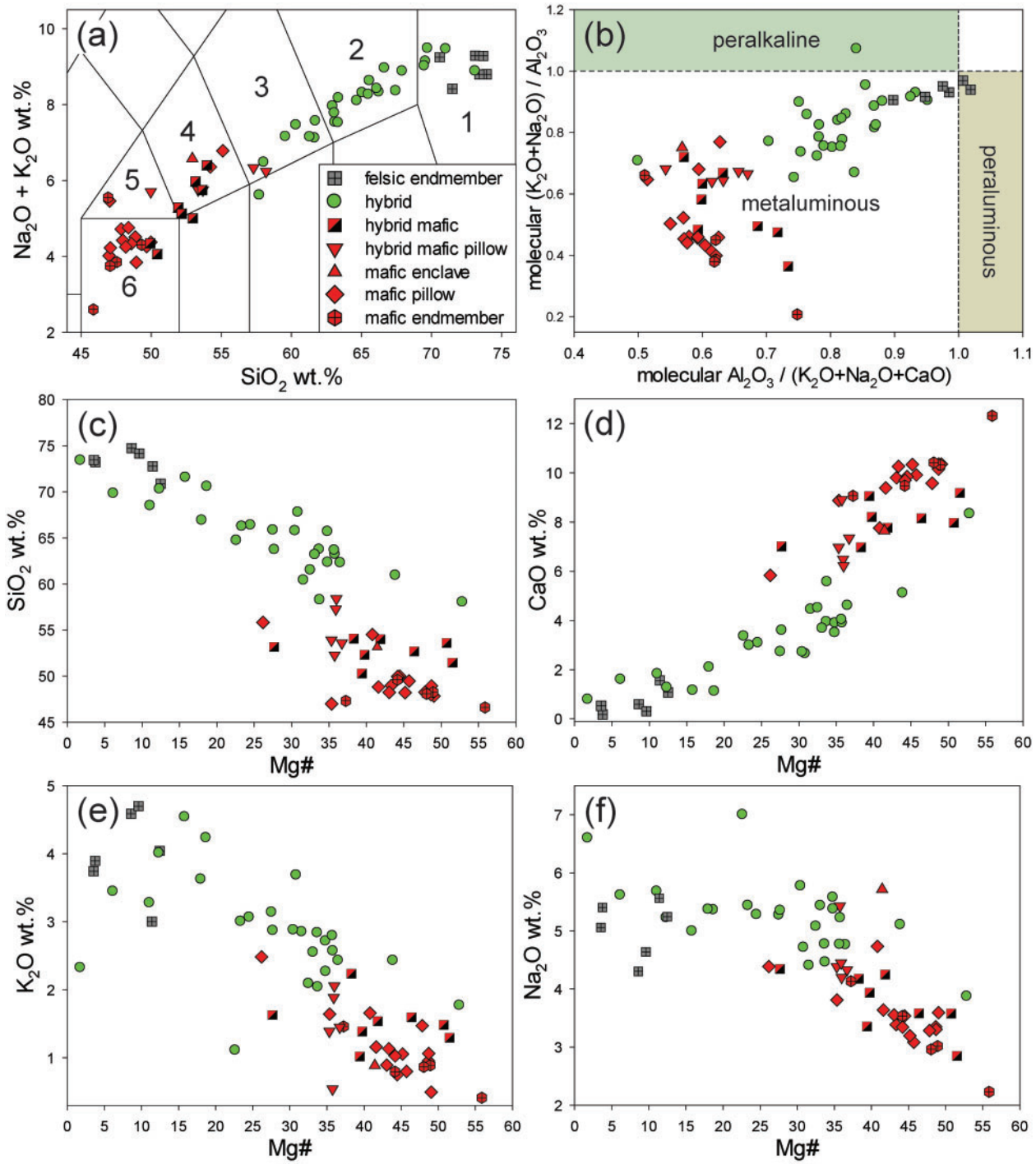


**Fig. 5.** Major element variation diagrams for the Austurhorn rocks. (a) Total alkalis–silica (TAS) diagram after Le Maitre *et al.* (1989). Felsic rocks plot in the field of rhyolites (1). Most hybrid rocks are classified as trachydacites (2) and trachyandesites (3), whereas one hybrid sample plots within the field of andesites and five hybrids have rhyolitic compositions. Mafic pillows from the 'net-veined' complex plot in the fields of trachyandesite, basaltic trachyandesite (4), trachybasalt (5) and basalt (6). Hybrid mafic rock compositions range from basaltic trachyandesitic to basaltic. One mafic enclave is classified as a basaltic trachyandesite. Mafic endmember rocks are basalts and trachybasalts. (b) Peralkalinity index PI [$(K_2O + Na_2O)/Al_2O_3$] vs alumina saturation index ASI [$Al_2O_3/(K_2O + Na_2O + CaO)$] showing that rock samples from the 'net-veined' complex are predominantly metaluminous. (c–h) Major and minor oxide compositions vs magnesium number [Mg#; molar $MgO/(MgO + FeO_{tot})$] (for discussion see text).

(continued)

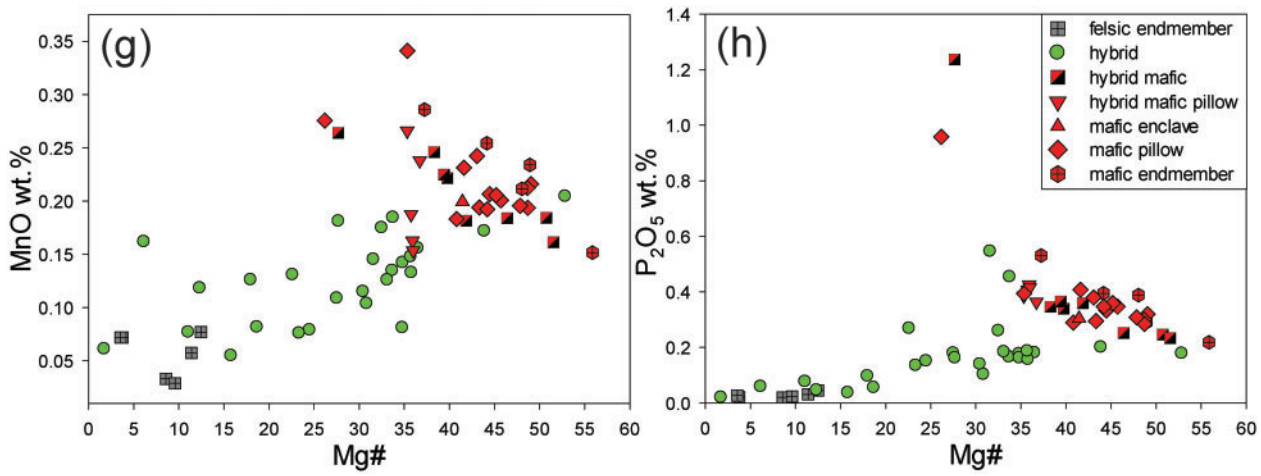


**Fig. 5.** Continued

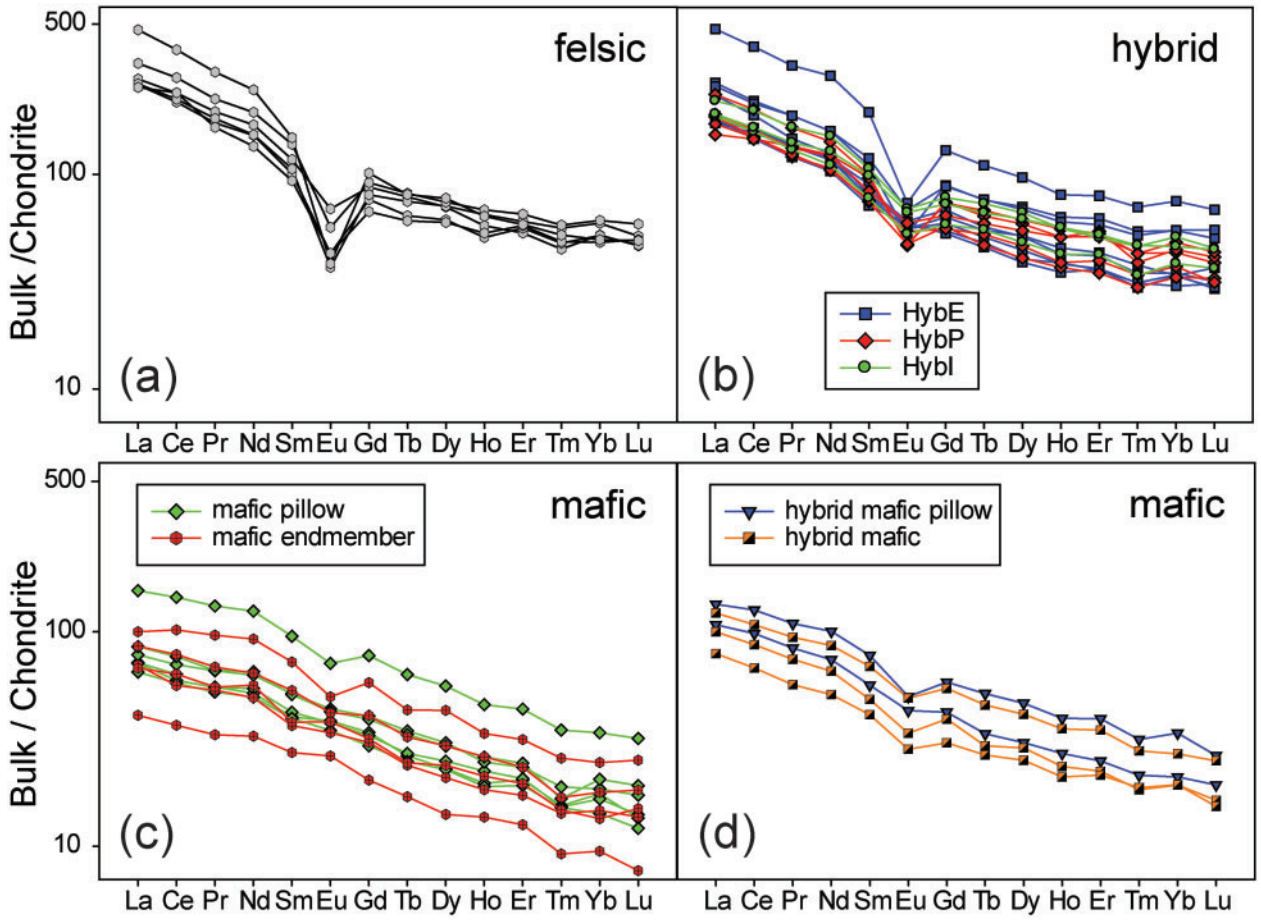


**Fig. 6.** Rare earth element (REE) patterns for Austurhorn rocks normalized to Cl chondrite (after Sun & McDonough, 1989). (a) Felsic rocks; (b) hybrid rocks; (c) mafic pillows and mafic endmember rocks; (d) hybrid mafic pillows and hybrid mafic rocks.

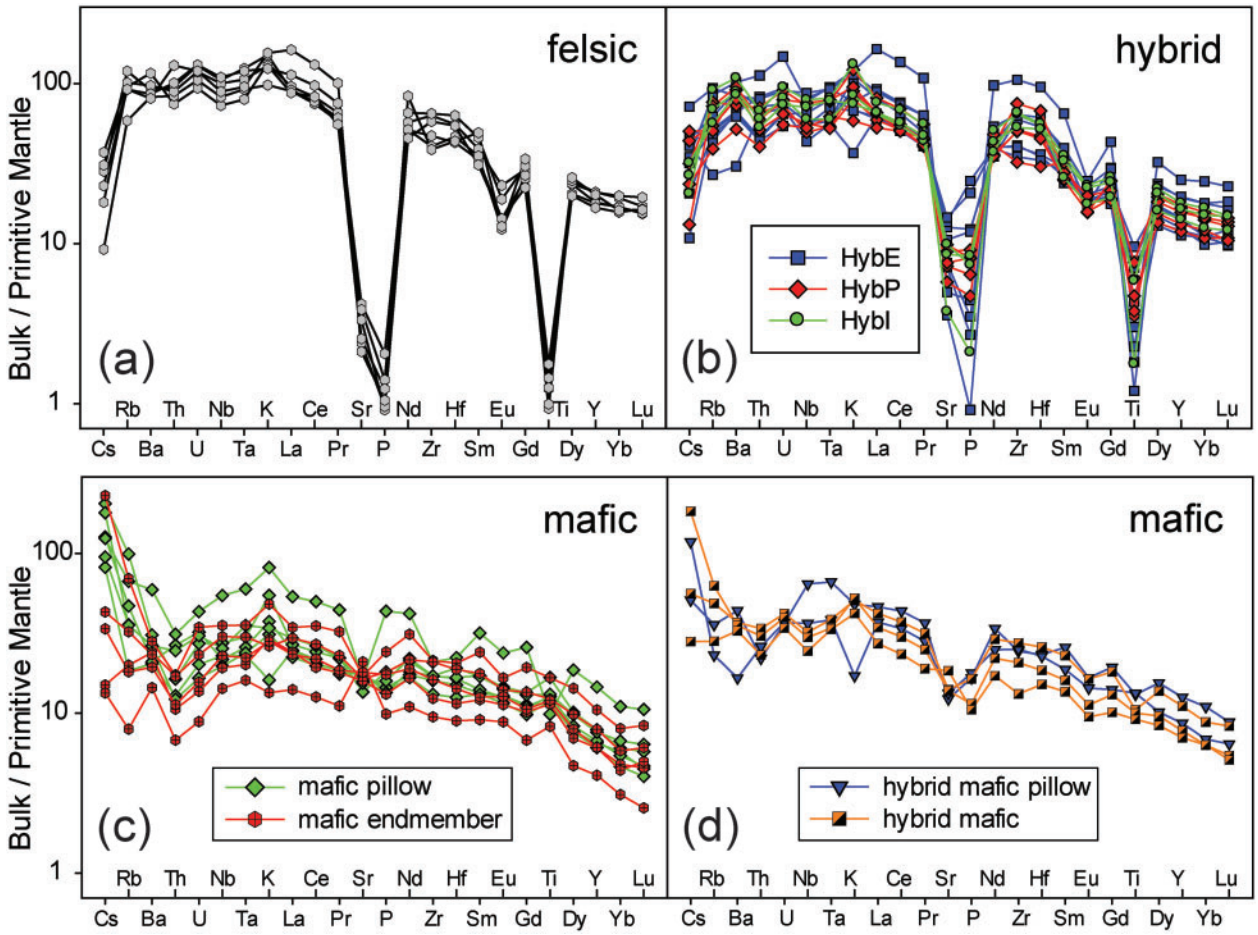


**Fig. 7.** Multi-element variation diagrams for felsic (a), hybrid (b), mafic pillow and mafic rocks (c, d) from the Austurhorn intrusion. Trace element concentrations are normalized to primitive mantle values after Sun & McDonough (1989). Felsic and hybrid rocks display marked negative anomalies in Sr, P and Ti.

in the Austurhorn rock series. Within these two rock groups, higher concentrations in Rb, Ba, Th, U, Nb and REE are observed in the felsic rocks than in the mafic rocks. Felsic and hybrid rocks display strong relative depletions in Sr, P and Ti (Fig. 7a and b) that are not present, or are much less pronounced, in the mafic rocks. Mafic pillows and mafic endmember rocks are, in contrast, characterized by slight, negative, relative anomalies in Th (Fig. 7c), very limited variability of Sr, but considerable variations (negative and positive relative to neighboring REE) in P and Ti. Hybrid mafic rocks and hybrid mafic pillows (Fig. 7d) show the characteristic relative depletions in Sr and P observed for the felsic and hybrid rock samples. One sample within the hybrid mafic pillow group records a negative K anomaly (Fig. 7d). Overall the normalized trace element patterns for the mafic rocks underline their transitional tholeiitic characteristics.

Ba, Sr, Zr, Sc and REE concentrations plotted against Th and La, utilized as a first-order differentiation index (Fig. 8a–h), characteristically show linear trends. The LREE such as La correlate positively with Th. The felsic endmembers display the highest concentrations, followed by the hybrid rocks. The mafic rocks show decreasing LREE contents with decreasing Th (<4 ppm Th), and the hybrid rocks plot on linear trends between felsic and mafic endmember rocks (Fig. 8b). All other REE (Sm, Gd, Tb, Dy, Tm, Ho, Er, Yb and Lu) display increasing concentrations with increasing Th content. In general, the quality of the linear relation between two REE diminishes from the LREE towards the HREE, most probably the result of zircon saturation and fractionation in the most evolved felsic liquids, effectively depleting Zr and HREE relative to Th. Some granophyres and hybrids do not follow the positive linear relationship defined by the majority of the felsic, hybrid and mafic rocks but rather plot on a separate linear trend showing a positive correlation between two REE (Fig. 8c). The plot of Eu/Eu* vs La displays considerable scatter, with some hybrids following the linear trend of the mafic rocks whereas others exhibit

a large variation in Eu/Eu* within the felsic endmembers (Fig. 8g).

Ba concentrations in felsic and hybrid samples scatter significantly from values ranging from 200 to 800 ppm, whereas the mafic endmember rocks cluster at lower Ba concentrations (Fig. 8a). Y concentrations are highest in the felsic and hybrid samples but show more intense scattering than the positive linear trend defined by the mafic rocks (Fig. 8h). At least four hybrid rock samples display comparable concentrations of Y to the average of the felsic endmembers. In general, large ion lithophile elements (LILE, such as Rb and Cs), as well as high field strength elements (HFSE, such as Th, Zr, Nb, Y and HREE), increase linearly with increasing $SiO_2$ (Table 1).

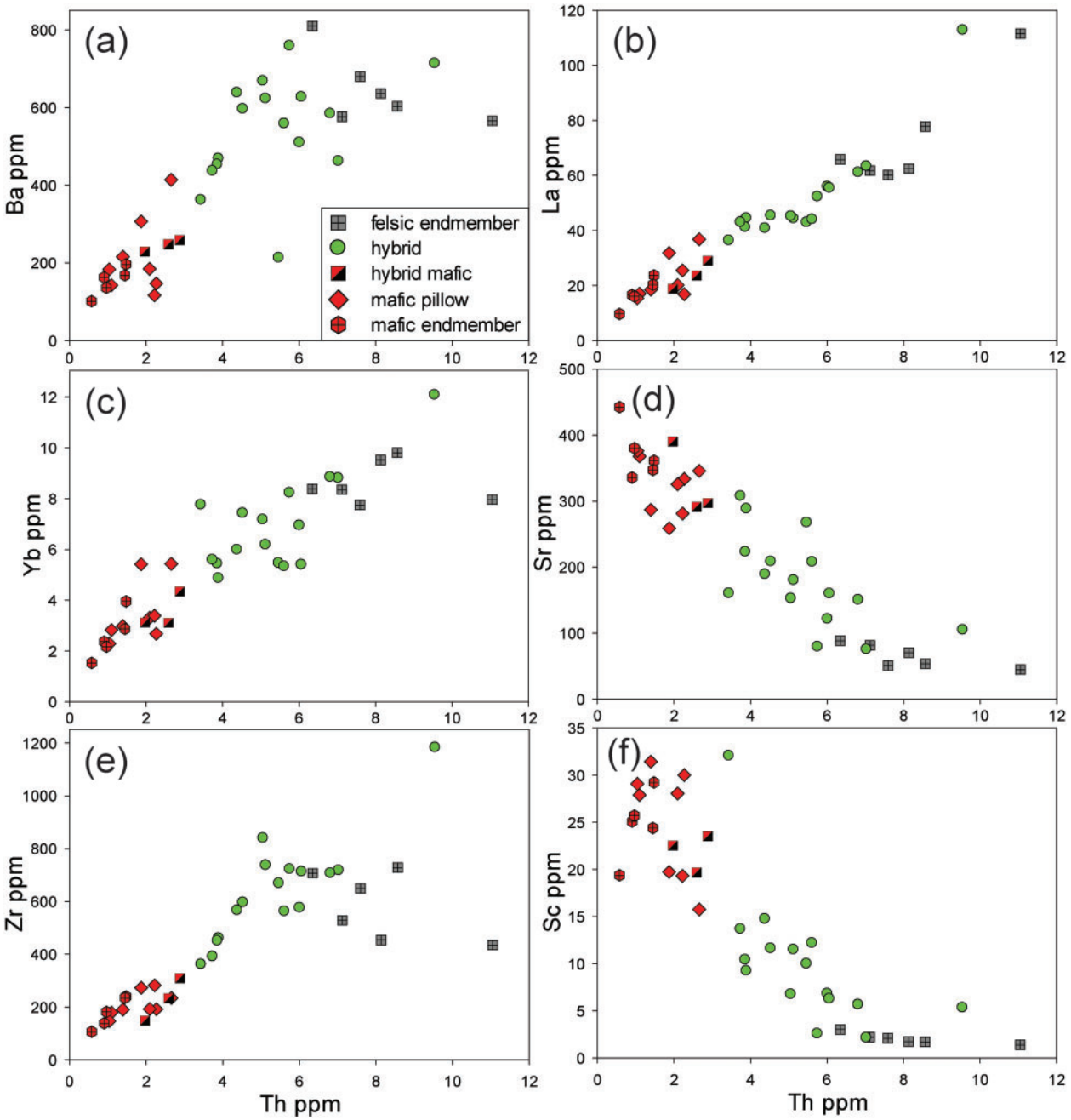


**Fig. 8.** Trace element variation diagrams for the Austurhorn rocks. (a–f) Selected trace elements (ppm) vs Th (ppm); (g, h) Eu/Eu* and Y (ppm) vs La (ppm).

(continued)

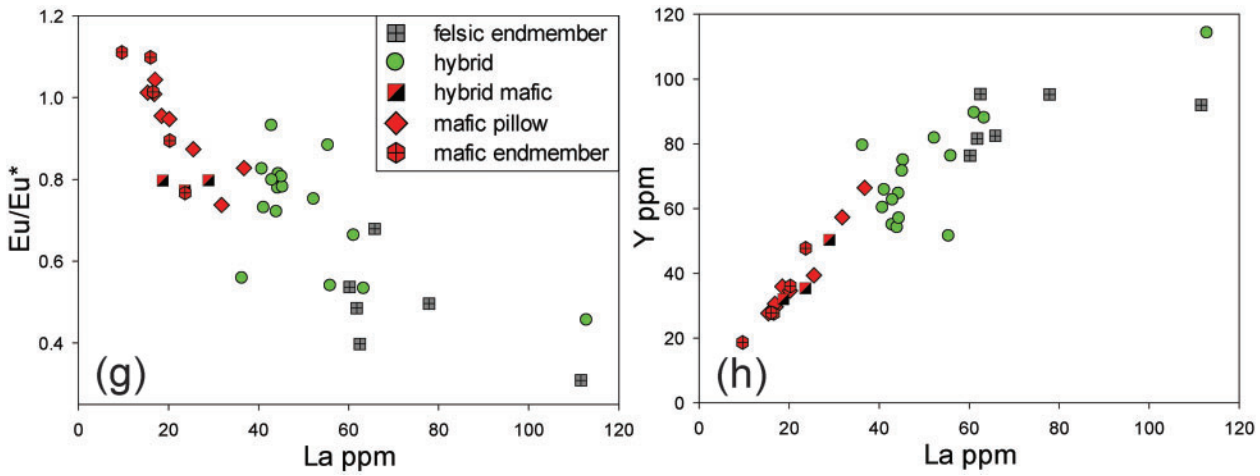


**Fig. 8.** Continued

In all rock types, Sr shows decreasing concentrations with increasing Th (Fig. 8d).

## MINERAL CHEMISTRY

This section focuses on the mineral chemistry of clinopyroxenes and feldspars present in the Austurhorn rock series. These minerals are abundant in most rock types and often display distinct zonation patterns. They may, thus, provide pertinent information regarding conditions during mingling or mixing of different magmas at different stages.

### Clinopyroxene

The compositional range of clinopyroxene within the mafic and hybrid rocks is $Wo_{34}$ $En_{22}$ $Fs_{44}$ to $Wo_{48}$ $En_{11}$ $Fs_{41}$. Clinopyroxene crystals within the hybrid rocks show a larger range in Ca than the pyroxenes in the mafic rocks. The Mg# ranges in all analysed rock samples from 58 to 79, whereas clinopyroxene in the hybrid rocks has a lower Mg#. In both rock types, $TiO_2$ ranges significantly from 0·1 to 3·3 wt % with an average of 0·9 wt %. Clinopyroxene in the hybrid rocks commonly shows stepwise normal zoning patterns (Fig. 9a). Most clinopyroxene crystals in the hybrid rocks generally have a high-Mg# core (>70; Table 2), which decreases stepwise towards the rim (Mg# ~60; Table 2). In addition to stepwise and normally zoned crystals, the hybrid rocks occasionally contain clinopyroxene displaying oscillatory zoning patterns (Fig. 9a). Clinopyroxene is often mantled by amphibole and exhibits intense resorption at the rim.

### Amphibole

Representative analyses of amphiboles from hybrid and mafic rocks are listed in Table 3 and plotted in Fig. 10a. Amphiboles are calcic including (ferro-)edenite, actinolitic hornblende and (magnesio-)hornblende. Si in edenite ranges from 6·86 to 7·37 p.f.u. and in hornblende from 6·40 to 7·50 p.f.u.. Sodium content in edenite ranges from 0·54 to 0·78 (p.f.u.) whereas a larger variation in Na is observed in hornblende (0·21–0·78 p.f.u.).

### Feldspar

Plagioclase phenocrysts (up to 10 mm in size) range in anorthite content from $An_9$ to $An_{81}$ in the mafic rocks and from $An_9$ to $An_{83}$ in the hybrid rocks (Table 4). In general, plagioclase crystals from the hybrid and mafic rocks become more enriched in the orthoclase component when approaching albitic compositions (Fig. 10b). In addition to plagioclase the mafic rocks also contain rare K-feldspar, clustering at high orthoclase contents (Fig. 10b). In these mafic rocks only two feldspar analyses indicate compositions of intermediate alkali feldspar solid solution, whereas feldspars from the hybrid rocks continuously cover the Or–Ab compositional range (Fig. 10b). It should be noted that the hybrid rocks contain a large fraction of highly altered alkali feldspar within the groundmass. A few feldspars from mafic and hybrid rock samples have almost pure potassium- or sodium-feldspar compositions.

The hybrid rocks contain both inversely and normally zoned plagioclase, with the former being dominant. Based on mineral chemistry and zonation patterns, four plagioclase groups can be distinguished within the hybrid rocks.

(1) The first group has An contents of around 80 in the core with stepwise decreasing An contents towards the crystal rim (Fig. 9b). These plagioclases have similar An contents to the plagioclases within the mafic rocks.
(2) The second group of phenocrysts exhibits intermediate anorthite contents in the core ($An_{50–60}$) that

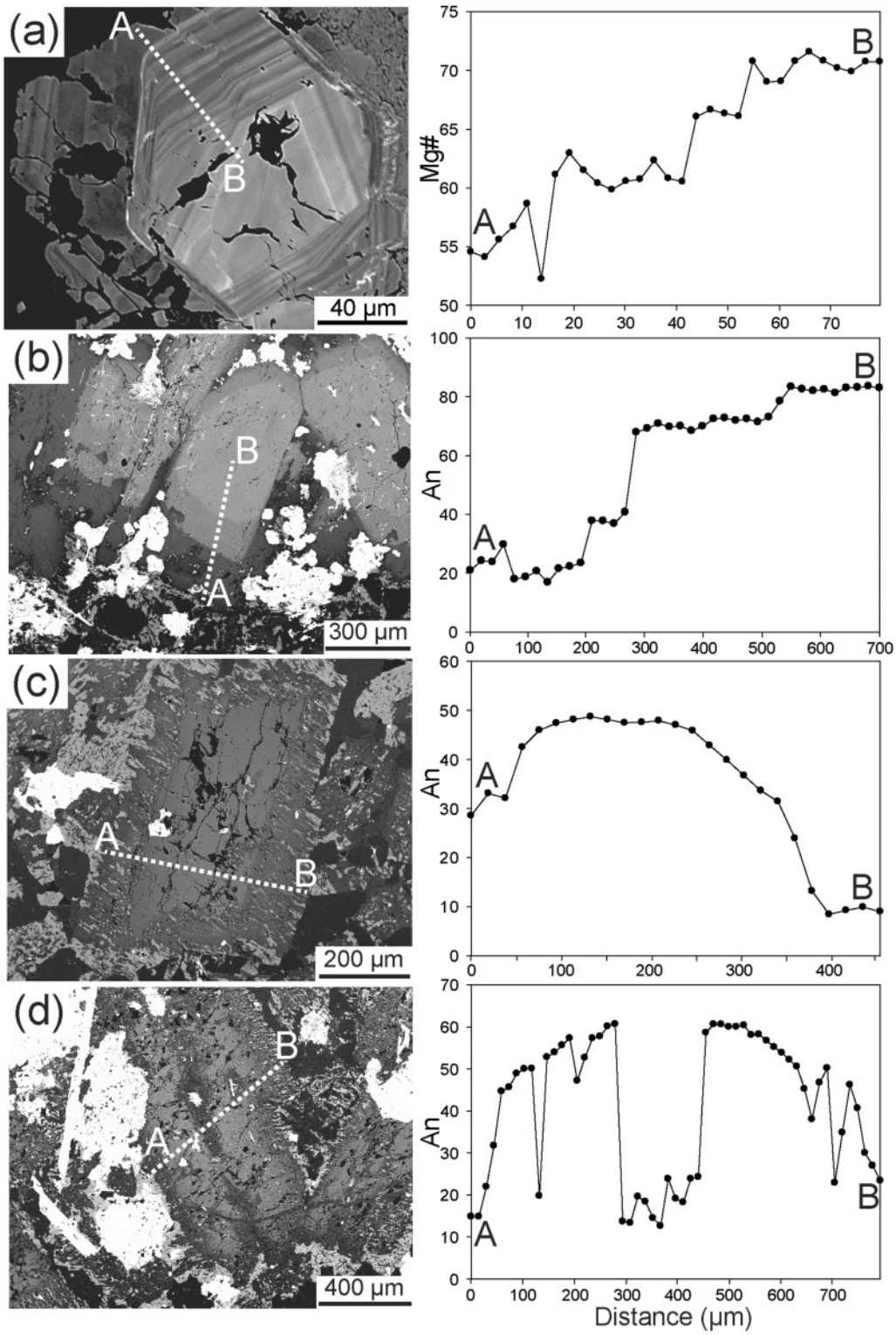


**Fig. 9.** Crystal zonation within pyroxene and plagioclase from the hybrid and mafic rocks of the Austurhorn intrusion. (a) Back-scattered electron image of zoned clinopyroxene in hybrid sample A5-9/l, which displays normal, step-zonation; diagram on the right shows Mg# variations along profile (A–B) through the pyroxene. (b–d) Different plagioclase zonation patterns within hybrid rocks from the 'net-veined' complex indicating complex mixing and mingling dynamics in the root zone of the Austurhorn magma chamber. Diagrams on the right display An variations (mol %) along the indicated profiles.

*Table 2: Representative clinopyroxene analyses in hybrid and mafic rocks from the Austurhorn intrusion*

| Rock type: | hybrid | hybrid | | | hybrid | | hybrid | | hybrid | |
|---|---|---|---|---|---|---|---|---|---|---|
| Sample: | A5-5 | A5-7-2 | | | A5-7-3 | | A5-9-1 | | A5-9-2 | |
| | core | rim | middle | core | rim | core | rim | core | rim | core |
| $SiO_2$ | 52·31 | 52·48 | 50·51 | 47·04 | 51·92 | 53·12 | 51·48 | 51·19 | 52·16 | 50·91 |
| $TiO_2$ | 0·09 | 0·32 | 1·14 | 2·50 | 0·11 | 0·17 | 0·63 | 1·11 | 0·13 | 0·90 |
| $Al_2O_3$ | 0·32 | 1·13 | 2·20 | 5·99 | 0·33 | 0·51 | 1·57 | 2·56 | 0·42 | 2·09 |
| FeO | 13·36 | 8·54 | 9·38 | 10·10 | 14·53 | 7·24 | 11·33 | 8·34 | 13·44 | 11·19 |
| MnO | 0·49 | 0·39 | 0·32 | 0·19 | 0·55 | 0·22 | 0·51 | 0·17 | 0·73 | 0·48 |
| MgO | 11·57 | 12·91 | 14·59 | 13·66 | 11·55 | 14·92 | 13·29 | 15·86 | 12·16 | 14·15 |
| CaO | 21·40 | 23·91 | 20·90 | 20·06 | 20·67 | 23·66 | 20·60 | 20·36 | 20·62 | 20·00 |
| $Na_2O$ | 0·49 | 0·38 | 0·38 | 0·34 | 0·32 | 0·14 | 0·39 | 0·28 | 0·35 | 0·38 |
| $K_2O$ | 0·02 | 0·00 | 0·00 | 0·00 | 0·01 | 0·01 | 0·01 | 0·01 | 0·00 | 0·00 |
| $P_2O_5$ | 0·01 | 0·00 | 0·00 | 0·03 | 0·03 | 0·03 | 0·04 | 0·02 | 0·00 | 0·00 |
| Total | 100·06 | 100·06 | 99·42 | 99·91 | 100·01 | 100·01 | 99·85 | 99·90 | 100·02 | 100·10 |
| *Cations based on 4 cations and 12 charges* | | | | | | | | | | |
| Si | 1·98 | 1·96 | 1·89 | 1·76 | 1·98 | 1·97 | 1·94 | 1·89 | 1·98 | 1·90 |
| Ti | 0·00 | 0·01 | 0·03 | 0·07 | 0·00 | 0·00 | 0·02 | 0·03 | 0·00 | 0·03 |
| Al | 0·01 | 0·05 | 0·10 | 0·26 | 0·01 | 0·02 | 0·07 | 0·11 | 0·02 | 0·09 |
| $Fe^{3+}$ | 0·05 | 0·04 | 0·09 | 0·11 | 0·05 | 0·04 | 0·05 | 0·06 | 0·04 | 0·08 |
| $Fe^{2+}$ | 0·37 | 0·23 | 0·21 | 0·21 | 0·42 | 0·18 | 0·31 | 0·20 | 0·38 | 0·27 |
| Mn | 0·02 | 0·01 | 0·01 | 0·01 | 0·02 | 0·01 | 0·02 | 0·01 | 0·02 | 0·02 |
| Mg | 0·65 | 0·72 | 0·81 | 0·76 | 0·66 | 0·82 | 0·74 | 0·87 | 0·69 | 0·79 |
| Ca | 0·87 | 0·96 | 0·84 | 0·80 | 0·84 | 0·94 | 0·83 | 0·81 | 0·84 | 0·80 |
| Na | 0·04 | 0·03 | 0·03 | 0·02 | 0·02 | 0·01 | 0·03 | 0·02 | 0·03 | 0·03 |
| Total | 4·00 | 4·00 | 4·00 | 4·00 | 4·00 | 4·00 | 4·00 | 4·00 | 4·00 | 4·00 |
| $Fe_{tot}$ | 0·42 | 0·26 | 0·28 | 0·30 | 0·46 | 0·22 | 0·35 | 0·25 | 0·42 | 0·34 |
| Mg# | 60·97 | 73·24 | 74·08 | 71·39 | 58·87 | 78·92 | 67·96 | 77·64 | 61·97 | 69·76 |
| Wo | 34·7 | 38·4 | 45·0 | 47·6 | 34·4 | 42·7 | 40·6 | 48·5 | 36·3 | 44·0 |
| En | 19·8 | 12·1 | 11·7 | 13·0 | 21·9 | 9·5 | 16·6 | 10·9 | 20·2 | 15·0 |
| Fs | 45·5 | 49·5 | 43·3 | 39·4 | 43·7 | 47·8 | 42·7 | 40·5 | 43·5 | 41·0 |

| Rock type: | hybrid | | | hybrid | | mafic | | mafic | |
|---|---|---|---|---|---|---|---|---|---|
| Sample: | A5-9-4 | | | A5-9-10 | | A4-1 | | A5-5-pillow | |
| | rim | middle | core | rim | core | rim | core | rim | core |
| $SiO_2$ | 51·90 | 52·06 | 52·37 | 52·44 | 52·23 | 48·99 | 50·81 | 52·74 | 51·36 |
| $TiO_2$ | 0·25 | 0·19 | 0·25 | 0·14 | 0·15 | 1·57 | 1·07 | 0·13 | 1·10 |
| $Al_2O_3$ | 0·52 | 0·48 | 0·80 | 0·40 | 0·43 | 4·46 | 2·94 | 0·36 | 2·89 |
| FeO | 14·78 | 14·23 | 11·65 | 13·21 | 13·20 | 7·81 | 7·49 | 13·48 | 7·78 |
| MnO | 0·78 | 0·73 | 0·54 | 0·45 | 0·61 | 0·17 | 0·17 | 0·37 | 0·20 |
| MgO | 11·95 | 11·98 | 13·22 | 12·15 | 12·18 | 14·63 | 15·74 | 12·25 | 15·59 |
| CaO | 19·39 | 19·78 | 20·92 | 20·83 | 20·81 | 21·32 | 21·31 | 21·95 | 21·73 |
| $Na_2O$ | 0·33 | 0·35 | 0·32 | 0·35 | 0·36 | 0·33 | 0·29 | 0·38 | 0·30 |
| $K_2O$ | 0·01 | 0·00 | 0·01 | 0·05 | 0·02 | 0·00 | 0·00 | 0·00 | 0·00 |
| $P_2O_5$ | 0·04 | 0·00 | 0·02 | 0·00 | 0·00 | 0·00 | 0·00 | 0·00 | 0·00 |
| Total | 99·95 | 99·80 | 100·09 | 100·02 | 99·99 | 99·28 | 99·82 | 101·66 | 100·96 |

(continued)

*Table 2: Continued*

| Rock type: | hybrid | | | hybrid | | mafic | | mafic | |
|---|---|---|---|---|---|---|---|---|---|
| Sample: | A5-9-4 | | | A5-9-10 | | A4-1 | | A5-5-pillow | |
| | rim | middle | core | rim | core | rim | core | rim | core |
| *Cations based on 4 cations and 12 charges* | | | | | | | | | |
| Si | 1·98 | 1·98 | 1·97 | 1·99 | 1·98 | 1·82 | 1·88 | 1·97 | 1·88 |
| Ti | 0·01 | 0·01 | 0·01 | 0·00 | 0·00 | 0·04 | 0·03 | 0·00 | 0·03 |
| Al | 0·02 | 0·02 | 0·04 | 0·02 | 0·02 | 0·20 | 0·13 | 0·02 | 0·12 |
| $Fe^{3+}$ | 0·03 | 0·03 | 0·04 | 0·03 | 0·04 | 0·09 | 0·08 | 0·07 | 0·08 |
| $Fe^{2+}$ | 0·44 | 0·43 | 0·33 | 0·39 | 0·38 | 0·15 | 0·15 | 0·35 | 0·16 |
| Mn | 0·03 | 0·02 | 0·02 | 0·01 | 0·02 | 0·01 | 0·01 | 0·01 | 0·01 |
| Mg | 0·68 | 0·68 | 0·74 | 0·69 | 0·69 | 0·81 | 0·87 | 0·68 | 0·85 |
| Ca | 0·79 | 0·81 | 0·84 | 0·85 | 0·84 | 0·85 | 0·84 | 0·88 | 0·85 |
| Na | 0·02 | 0·03 | 0·02 | 0·03 | 0·03 | 0·02 | 0·02 | 0·03 | 0·02 |
| Total | 4·00 | 4·00 | 4·00 | 4·00 | 4·00 | 4·00 | 4·00 | 4·00 | 4·00 |
| $Fe_{tot}$ | 0·47 | 0·45 | 0·36 | 0·42 | 0·41 | 0·23 | 0·22 | 0·41 | 0·23 |
| Mg# | 59·20 | 60·15 | 67·15 | 62·28 | 62·42 | 77·62 | 79·52 | 62·25 | 78·71 |
| Wo | 35·8 | 35·8 | 39·3 | 35·9 | 36·3 | 36·0 | 37·4 | 43·2 | 38·0 |
| En | 23·2 | 22·4 | 17·4 | 20·3 | 19·9 | 40·6 | 43·3 | 34·0 | 42·5 |
| Fs | 41·0 | 41·8 | 43·3 | 43·7 | 43·8 | 7·6 | 7·5 | 17·3 | 7·9 |

$Mg\# = 100\,Mg/(Mg + Fe_{tot})$.

become progressively more albite-rich towards the rim (Fig. 9c).

(3) The third group that occurs within the hybrid rocks consists of reversely zoned crystals that have clearly been exposed to a changing melt composition during their growth. The chemical variation within single crystals is characterized by An contents of 10–20 in the core and 5–15 at the rim. From core to rim the An content increases abruptly from $\sim An_{20}$ to values of $\sim An_{60}$ (Fig. 9d) and decreases thereafter to about $An_{45}$, followed by a rapid, but continuous decrease to the rim values. The zoning patterns of plagioclase crystals occurring near the contact between hybrid rocks and mafic pillows are noteworthy (A5-7-7; Table 4). The An content increases from the core ($\sim An_{14}$) towards the margins ($\sim An_{60}$), followed by an overgrowth with normal zoning, which results in crystal rims with An contents <15. The crystal side facing the mafic pillow is characterized by saw-toothed zonation.

(4) The fourth group of plagioclase crystals within the hybrid rocks typically has An contents ranging from 15 to 25 and exhibits reaction textures (e.g. sieve textures). These sieve textures result in a step-like pattern in which the anorthite content rapidly shifts from values of around 25 down to 15. Within this group predominantly stepwise normal zoning is preserved, showing albitic rims with An content ranging from 5 to 10. Some plagioclase crystals are affected by more intense reaction and characteristically show An compositions ranging from 10 to 45 (electronic appendix), often with lower An contents in the core. However, the dissolution–melting reaction that led to the formation of the sieve-textured zones is composed not only of plagioclase, but represents a fine-grained mixture of dissolved plagioclase, crystallized melt and even later alteration products; thus a clean zonation pattern is difficult to obtain from such plagioclase crystals.

## DISCUSSION

### Mingling and mixing processes inferred from field relations

The complexity of magma mixing and mingling clearly increases from NE to SW within the intrusion (Fig. 1). Intruding mafic magma has a significantly higher temperature and lower viscosity than the partially crystallized granophyre. The relative intrusion sequence is clearly evidenced by field and petrographic relationships. Mafic magmas locally form sills with textures ranging from very

*Table 3: Representative amphibole analyses in hybrid and mafic rocks from the Austurhorn intrusion*

| Rock type: | hybrid | | | hybrid | | hybrid | | hybrid | | hybrid | | hybrid |
|---|---|---|---|---|---|---|---|---|---|---|---|---|
| Sample: | A5-5-4-1 | | | A5-5-3 | | A5-5-4 | | A5-5-5 | | A5-5-6 | | A5-7-3 |
| | #1 | #2 | #3 | #1 | #2 | #1 | #2 | #1 | #2 | #1 | #2 | #1 |
| $SiO_2$ (wt %) | 46·30 | 44·37 | 44·70 | 49·05 | 44·45 | 46·98 | 46·34 | 45·40 | 49·24 | 45·51 | 46·57 | 49·09 |
| $TiO_2$ | 1·68 | 2·52 | 1·94 | 0·55 | 0·93 | 0·77 | 0·79 | 1·10 | 0·60 | 1·32 | 1·39 | 0·93 |
| $Al_2O_3$ | 5·85 | 7·65 | 8·07 | 3·31 | 5·51 | 4·27 | 4·82 | 5·20 | 2·89 | 6·08 | 5·59 | 3·85 |
| FeO | 18·07 | 18·17 | 15·68 | 20·56 | 25·00 | 21·95 | 24·15 | 24·80 | 20·38 | 20·55 | 19·85 | 19·33 |
| MnO | 0·37 | 0·32 | 0·32 | 1·22 | 1·31 | 1·16 | 1·33 | 1·30 | 1·01 | 0·98 | 1·00 | 0·47 |
| MgO | 11·69 | 11·19 | 12·77 | 9·98 | 7·08 | 9·24 | 7·64 | 6·75 | 10·69 | 9·57 | 10·40 | 12·03 |
| CaO | 11·64 | 11·93 | 12·67 | 12·03 | 10·58 | 11·13 | 10·89 | 10·80 | 11·41 | 11·22 | 11·33 | 10·87 |
| $Na_2O$ | 2·22 | 2·60 | 2·61 | 1·85 | 2·17 | 1·99 | 2·20 | 2·12 | 1·62 | 2·23 | 2·26 | 1·59 |
| $K_2O$ | 0·71 | 0·75 | 0·46 | 0·52 | 0·92 | 0·87 | 0·79 | 0·93 | 0·63 | 0·86 | 0·66 | 0·53 |
| Total | 98·53 | 99·51 | 99·22 | 99·07 | 97·94 | 98·36 | 98·95 | 98·41 | 98·48 | 98·32 | 99·05 | 98·70 |
| *Cations based on 13 cations + Na + K and 46 charges* | | | | | | | | | | | | |
| Si | 6·89 | 6·60 | 6·60 | 7·37 | 6·86 | 7·13 | 7·06 | 7·00 | 7·36 | 6·88 | 6·95 | 7·18 |
| Ti | 0·19 | 0·28 | 0·22 | 0·06 | 0·11 | 0·09 | 0·09 | 0·13 | 0·07 | 0·15 | 0·16 | 0·10 |
| Al | 1·03 | 1·34 | 1·40 | 0·59 | 1·00 | 0·76 | 0·87 | 0·95 | 0·51 | 1·08 | 0·98 | 0·66 |
| $Fe^{3+}$ | 0·32 | 0·21 | 0·13 | 0·03 | 0·73 | 0·44 | 0·47 | 0·40 | 0·38 | 0·39 | 0·41 | 0·80 |
| $Fe^{2+}$ | 1·93 | 2·05 | 1·80 | 2·56 | 2·50 | 2·35 | 2·60 | 2·80 | 2·17 | 2·21 | 2·06 | 1·56 |
| Mn | 0·05 | 0·04 | 0·04 | 0·16 | 0·17 | 0·15 | 0·17 | 0·17 | 0·13 | 0·13 | 0·13 | 0·06 |
| Mg | 2·59 | 2·48 | 2·81 | 2·24 | 1·63 | 2·09 | 1·73 | 1·55 | 2·38 | 2·16 | 2·31 | 2·62 |
| Ca | 1·86 | 1·90 | 2·00 | 1·94 | 1·75 | 1·81 | 1·78 | 1·79 | 1·83 | 1·82 | 1·81 | 1·70 |
| Na | 0·64 | 0·75 | 0·75 | 0·54 | 0·65 | 0·59 | 0·65 | 0·63 | 0·47 | 0·65 | 0·65 | 0·45 |
| K | 0·14 | 0·14 | 0·09 | 0·10 | 0·18 | 0·17 | 0·15 | 0·18 | 0·12 | 0·17 | 0·13 | 0·10 |
| Total | 15·63 | 15·79 | 15·84 | 15·58 | 15·58 | 15·56 | 15·58 | 15·60 | 15·42 | 15·64 | 15·59 | 15·26 |
| $FeO_{tot}$ | 2·22 | 2·24 | 1·92 | 2·58 | 3·15 | 2·74 | 3·03 | 3·16 | 2·51 | 2·56 | 2·43 | 2·29 |
| Mg# | 53·91 | 52·56 | 59·38 | 46·41 | 34·06 | 43·26 | 36·42 | 32·94 | 48·70 | 45·73 | 48·71 | 53·45 |

| Rock type: | hybrid | hybrid | | | | hybrid | | mafic | | | |
|---|---|---|---|---|---|---|---|---|---|---|---|
| Sample: | A5-7-4 | A7-10 | | | | A7-22 | | A7-22-b | | | |
| | #1 | #1 | #2 | #3 | #4 | #1 | #2 | #1 | #2 | #3 | #4 |
| $SiO_2$ (wt %) | 48·87 | 48·16 | 45·94 | 43·61 | 43·39 | 45·58 | 45·97 | 45·66 | 44·76 | 44·52 | 45·25 |
| $TiO_2$ | 1·42 | 1·50 | 1·46 | 3·63 | 3·56 | 1·29 | 0·82 | 1·24 | 2·17 | 1·65 | 2·10 |
| $Al_2O_3$ | 4·78 | 4·83 | 5·72 | 9·15 | 9·24 | 5·67 | 4·99 | 9·23 | 8·29 | 8·95 | 8·18 |
| FeO | 15·94 | 17·38 | 19·07 | 14·79 | 14·84 | 23·79 | 23·56 | 16·71 | 16·57 | 16·76 | 16·47 |
| MnO | 0·41 | 0·38 | 0·38 | 0·28 | 0·28 | 0·64 | 0·73 | 0·20 | 0·18 | 0·21 | 0·21 |
| MgO | 13·83 | 13·44 | 11·05 | 12·31 | 12·47 | 8·31 | 9·64 | 11·81 | 12·14 | 11·71 | 12·18 |
| CaO | 11·07 | 10·17 | 10·59 | 11·56 | 11·58 | 10·75 | 10·13 | 10·81 | 11·49 | 11·54 | 11·59 |
| $Na_2O$ | 2·16 | 2·40 | 2·69 | 2·71 | 2·73 | 1·91 | 2·03 | 2·25 | 2·27 | 2·36 | 2·30 |
| $K_2O$ | 0·57 | 0·50 | 0·64 | 0·57 | 0·58 | 0·78 | 0·57 | 1·33 | 0·78 | 0·79 | 0·77 |
| Total | 99·04 | 98·77 | 97·54 | 98·61 | 98·67 | 98·72 | 98·43 | 99·24 | 98·65 | 98·50 | 99·05 |

(continued)

*Table 3: Continued*

| Rock type: | hybrid | hybrid | | | | hybrid | | mafic | | | |
|---|---|---|---|---|---|---|---|---|---|---|---|
| Sample: | A5-7-4 | A7-10 | | | | A7-22 | | A7-22-b | | | |
| | #1 | #1 | #2 | #3 | #4 | #1 | #2 | #1 | #2 | #3 | #4 |
| *Cations based on 13 cations + Na + K and 46 charges* | | | | | | | | | | | |
| Si | 7·07 | 6·97 | 6·90 | 6·44 | 6·40 | 6·89 | 6·86 | 6·65 | 6·59 | 6·58 | 6·64 |
| Ti | 0·15 | 0·16 | 0·16 | 0·40 | 0·39 | 0·15 | 0·09 | 0·14 | 0·24 | 0·18 | 0·23 |
| Al | 0·82 | 0·82 | 1·01 | 1·59 | 1·61 | 1·01 | 0·88 | 1·59 | 1·44 | 1·56 | 1·42 |
| $Fe^{3+}$ | 0·59 | 1·00 | 0·53 | 0·19 | 0·27 | 0·74 | 1·29 | 0·58 | 0·48 | 0·43 | 0·40 |
| $Fe^{2+}$ | 1·33 | 1·10 | 1·86 | 1·63 | 1·56 | 2·27 | 1·65 | 1·46 | 1·56 | 1·64 | 1·63 |
| Mn | 0·05 | 0·05 | 0·05 | 0·04 | 0·03 | 0·08 | 0·09 | 0·02 | 0·02 | 0·03 | 0·03 |
| Mg | 2·98 | 2·90 | 2·47 | 2·71 | 2·74 | 1·87 | 2·14 | 2·56 | 2·66 | 2·58 | 2·66 |
| Ca | 1·72 | 1·58 | 1·70 | 1·83 | 1·83 | 1·74 | 1·62 | 1·69 | 1·81 | 1·83 | 1·82 |
| Na | 0·61 | 0·67 | 0·78 | 0·78 | 0·78 | 0·56 | 0·59 | 0·64 | 0·65 | 0·68 | 0·65 |
| K | 0·10 | 0·09 | 0·12 | 0·11 | 0·11 | 0·15 | 0·11 | 0·25 | 0·15 | 0·15 | 0·14 |
| Total | 15·43 | 15·34 | 15·61 | 15·71 | 15·72 | 15·45 | 15·31 | 15·57 | 15·61 | 15·65 | 15·62 |
| $FeO_{tot}$ | 1·87 | 2·00 | 2·34 | 1·81 | 1·80 | 2·93 | 2·81 | 1·98 | 1·99 | 2·03 | 1·98 |
| Mg# | 61·48 | 59·14 | 51·37 | 59·99 | 60·32 | 38·96 | 43·28 | 56·46 | 57·21 | 55·99 | 57·35 |

$Mg\# = 100\,Mg/(Mg + Fe_{tot})$.

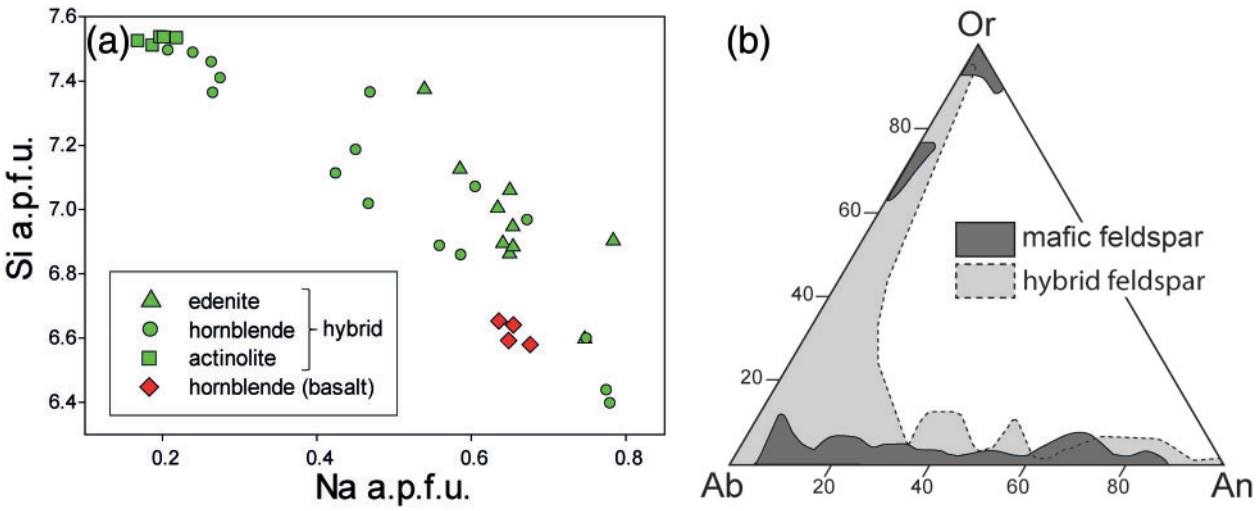


**Fig. 10.** Mineral chemistry of hybrid and mafic rocks from the Austurhorn intrusion. (a) Na vs Si (a.p.f.u.) in amphibole from hybrid and mafic rocks. (b) Feldspar compositions (1914 analyses) from mafic and hybrid rocks from the 'net-veined' complex plotted in the ternary Or–Ab–An diagram.

fine-grained, phenocryst-poor, to more ophitic textures a few tens of centimetres away from the contact with the felsic or hybrid magma. Towards the centre of the intrusions the mafic texture is equigranular and relatively coarse-grained. The textural development is symmetrical towards the two sides of the intrusion. Mafic pillowing is frequent at the tips of the intrusions or in smaller intrusions, again often with clear textural variations from very fine-grained at the chilled margin to coarser-grained in the central parts of the pillows. Fingering textures of mafic into more silicic magma most probably develop owing to the different rheological properties of the contrasting magmas during their interaction. South of Krossanesfjall, felsic 'flame structures' within a mafic sheet could indicate rheological inversion between felsic and mafic magmas at the time of interaction (Fig. 2b).

*Table 4: Representative plagioclase analyses in hybrid and mafic rocks from the Austurhorn intrusion*

| Rock type: | hybrid | | | hybrid | | | hybrid | | | hybrid | hybrid |
|---|---|---|---|---|---|---|---|---|---|---|---|
| Sample: | A5-7-7 | | | A5-7-6 | | | A7-3-1 | | | A7-3-2 | A7-29-b |
| | rim | middle | core | rim | middle | core | rim | middle | core | core | rim |
| $SiO_2$ (wt %) | 67·01 | 57·34 | 67·08 | 66·93 | 57·94 | 67·97 | 66·02 | 61·20 | 64·74 | 64·84 | 67·10 |
| $TiO_2$ | 0·01 | 0·08 | 0·03 | 0·00 | 0·09 | 0·00 | 0·01 | 0·04 | 0·04 | 0·02 | 0·00 |
| $Al_2O_3$ | 20·57 | 25·86 | 20·67 | 20·51 | 25·49 | 20·62 | 20·92 | 23·69 | 21·20 | 21·94 | 21·01 |
| FeO | 0·27 | 0·66 | 0·22 | 0·14 | 0·34 | 0·06 | 0·09 | 0·27 | 0·32 | 0·06 | 0·03 |
| MnO | 0·01 | 0·01 | 0·01 | 0·00 | 0·00 | 0·01 | 0·00 | 0·00 | 0·03 | 0·00 | 0·00 |
| MgO | 0·01 | 0·02 | 0·00 | 0·00 | 0·02 | 0·00 | 0·00 | 0·00 | 0·00 | 0·00 | 0·00 |
| CaO | 1·69 | 9·56 | 1·63 | 1·73 | 8·94 | 1·21 | 2·49 | 6·52 | 3·40 | 3·29 | 2·34 |
| $Na_2O$ | 9·34 | 5·93 | 9·85 | 9·84 | 6·41 | 9·98 | 9·82 | 7·99 | 9·14 | 9·43 | 10·99 |
| $K_2O$ | 0·35 | 0·27 | 0·43 | 0·58 | 0·24 | 0·20 | 0·50 | 0·43 | 0·83 | 0·16 | 0·27 |
| Total | 99·27 | 99·73 | 99·91 | 99·16 | 99·23 | 99·85 | 99·86 | 100·14 | 99·70 | 99·74 | 101·75 |
| *Cations based on 5 cations and 16 charges* | | | | | | | | | | | |
| Si | 2·99 | 2·59 | 2·97 | 2·96 | 2·62 | 3·00 | 2·92 | 2·72 | 2·88 | 2·87 | 2·89 |
| Ti | 0·00 | 0·00 | 0·00 | 0·00 | 0·00 | 0·00 | 0·00 | 0·00 | 0·00 | 0·00 | 0·00 |
| Al | 1·08 | 1·38 | 1·08 | 1·07 | 1·36 | 1·07 | 1·09 | 1·24 | 1·11 | 1·15 | 1·07 |
| $Fe^{3+}$ | 0·00 | 0·00 | 0·00 | 0·00 | 0·00 | 0·00 | 0·00 | 0·01 | 0·00 | 0·00 | 0·00 |
| $Fe^{2+}$ | 0·01 | 0·03 | 0·01 | 0·01 | 0·01 | 0·00 | 0·00 | 0·00 | 0·01 | 0·00 | 0·00 |
| Mn | 0·00 | 0·00 | 0·00 | 0·00 | 0·00 | 0·00 | 0·00 | 0·00 | 0·00 | 0·00 | 0·00 |
| Mg | 0·00 | 0·00 | 0·00 | 0·00 | 0·00 | 0·00 | 0·00 | 0·00 | 0·00 | 0·00 | 0·00 |
| Ca | 0·08 | 0·46 | 0·08 | 0·08 | 0·43 | 0·06 | 0·12 | 0·31 | 0·16 | 0·16 | 0·11 |
| Na | 0·81 | 0·52 | 0·84 | 0·84 | 0·56 | 0·85 | 0·84 | 0·69 | 0·79 | 0·81 | 0·92 |
| K | 0·02 | 0·02 | 0·02 | 0·03 | 0·01 | 0·01 | 0·03 | 0·02 | 0·05 | 0·01 | 0·01 |
| Total | 5·00 | 5·00 | 5·00 | 5·00 | 5·00 | 5·00 | 5·00 | 5·00 | 5·00 | 5·00 | 5·00 |
| An | 14·85 | 60·67 | 13·69 | 14·23 | 57·35 | 10·63 | 19·43 | 43·65 | 25·44 | 25·55 | 17·21 |
| Ab | 82·06 | 37·64 | 82·73 | 80·96 | 41·12 | 87·62 | 76·64 | 53·49 | 68·38 | 73·23 | 80·81 |
| Or | 3·09 | 1·69 | 3·58 | 4·81 | 1·53 | 1·75 | 3·93 | 2·86 | 6·18 | 1·22 | 1·99 |

| Rock type: | hybrid mafic pillow | | | hybrid mafic pillow | | hybrid mafic | | mafic pillow | | mafic pillow | |
|---|---|---|---|---|---|---|---|---|---|---|---|
| Sample | A7-10-2 | | | A7-10-2 | | A5-5-3 | | A5-9-1 | | A5-9-1 | |
| | rim | middle | core | rim | core | rim | core | rim | core | rim | core |
| $SiO_2$ (wt %) | 68·11 | 60·63 | 67·24 | 67·70 | 60·73 | 68·12 | 58·92 | 63·92 | 47·45 | 60·81 | 50·78 |
| $TiO_2$ | 0·01 | 0·09 | 0·03 | 0·00 | 0·02 | 0·01 | 0·06 | 0·03 | 0·05 | 0·12 | 0·09 |
| $Al_2O_3$ | 20·33 | 25·11 | 21·72 | 19·99 | 23·79 | 20·13 | 25·08 | 22·03 | 32·41 | 23·66 | 30·00 |
| FeO | 0·20 | 0·47 | 0·20 | 0·08 | 0·33 | 0·08 | 0·40 | 0·26 | 0·59 | 0·92 | 0·29 |
| MnO | 0·01 | 0·03 | 0·00 | 0·00 | 0·00 | 0·00 | 0·03 | 0·00 | 0·02 | 0·01 | 0·01 |
| MgO | 0·00 | 0·06 | 0·01 | 0·00 | 0·02 | 0·00 | 0·02 | 0·00 | 0·01 | 0·02 | 0·00 |
| CaO | 1·46 | 7·49 | 2·80 | 1·06 | 6·61 | 0·77 | 8·19 | 4·14 | 17·52 | 6·32 | 14·38 |
| $Na_2O$ | 8·99 | 5·81 | 7·49 | 9·65 | 7·25 | 7·87 | 6·57 | 8·16 | 1·91 | 7·40 | 3·44 |
| $K_2O$ | 0·47 | 0·43 | 1·14 | 0·83 | 0·52 | 2·30 | 0·43 | 0·94 | 0·04 | 0·52 | 0·13 |
| Total | 99·58 | 100·11 | 100·64 | 99·32 | 99·28 | 99·28 | 99·70 | 99·48 | 99·99 | 99·78 | 99·12 |

(continued)

*Table 4: Continued*

| Rock type: | hybrid mafic pillow | | | hybrid mafic pillow | | hybrid mafic | | mafic pillow | | mafic pillow | |
|---|---|---|---|---|---|---|---|---|---|---|---|
| Sample | A7-10-2 | | | A7-10-2 | | A5-5-3 | | A5-9-1 | | A5-9-1 | |
| | rim | middle | core | rim | core | rim | core | rim | core | rim | core |
| *Cations based on 5 cations and 16 charges* | | | | | | | | | | | |
| Si | 3·04 | 2·74 | 3·00 | 3·02 | 2·74 | 3·07 | 2·65 | 2·86 | 2·18 | 2·73 | 2·34 |
| Ti | 0·00 | 0·00 | 0·00 | 0·00 | 0·00 | 0·00 | 0·00 | 0·00 | 0·00 | 0·00 | 0·00 |
| Al | 1·07 | 1·34 | 1·14 | 1·05 | 1·26 | 1·07 | 1·33 | 1·16 | 1·76 | 1·25 | 1·63 |
| $Fe^{3+}$ | 0·00 | 0·00 | 0·00 | 0·00 | 0·00 | 0·00 | 0·00 | 0·00 | 0·02 | 0·00 | 0·01 |
| $Fe^{2+}$ | 0·01 | 0·02 | 0·01 | 0·00 | 0·01 | 0·00 | 0·01 | 0·01 | 0·00 | 0·03 | 0·00 |
| Mn | 0·00 | 0·00 | 0·00 | 0·00 | 0·00 | 0·00 | 0·00 | 0·00 | 0·00 | 0·00 | 0·00 |
| Mg | 0·00 | 0·00 | 0·00 | 0·00 | 0·00 | 0·00 | 0·00 | 0·00 | 0·00 | 0·00 | 0·00 |
| Ca | 0·07 | 0·36 | 0·13 | 0·05 | 0·32 | 0·04 | 0·40 | 0·20 | 0·86 | 0·30 | 0·71 |
| Na | 0·78 | 0·51 | 0·65 | 0·83 | 0·63 | 0·69 | 0·57 | 0·71 | 0·17 | 0·64 | 0·31 |
| K | 0·03 | 0·02 | 0·07 | 0·05 | 0·03 | 0·13 | 0·02 | 0·05 | 0·00 | 0·03 | 0·01 |
| Total | 5·00 | 5·00 | 5·00 | 5·00 | 5·00 | 5·00 | 5·00 | 5·00 | 5·00 | 5·00 | 5·00 |
| An | 13·37 | 54·56 | 24·49 | 9·22 | 45·96 | 7·02 | 53·92 | 20·68 | 83·35 | 44·38 | 80·13 |
| Ab | 82·34 | 42·32 | 65·51 | 83·56 | 50·41 | 71·95 | 43·26 | 73·75 | 16·44 | 51·96 | 19·17 |
| Or | 4·28 | 3·11 | 10·01 | 7·23 | 3·64 | 21·03 | 2·82 | 5·57 | 0·20 | 3·66 | 0·70 |

| Rock type: | mafic pillow | | mafic pillow | |
|---|---|---|---|---|
| Sample: | A5-5-4-6 | | A5-5-4-1 | |
| | rim | core | rim | core |
| $SiO_2$ (wt %) | 61·08 | 48·55 | 65·99 | 57·58 |
| $TiO_2$ | 0·02 | 0·08 | 0·02 | 0·03 |
| $Al_2O_3$ | 23·78 | 31·42 | 20·33 | 25·99 |
| FeO | 0·32 | 0·65 | 0·21 | 0·21 |
| MnO | 0·00 | 0·02 | 0·00 | 0·00 |
| MgO | 0·01 | 0·02 | 0·01 | 0·00 |
| CaO | 6·75 | 17·77 | 2·21 | 9·56 |
| $Na_2O$ | 7·63 | 2·53 | 9·32 | 6·35 |
| $K_2O$ | 0·59 | 0·05 | 1·06 | 0·37 |
| Total | 100·18 | 101·09 | 99·15 | 100·09 |
| *Cations based on 5 cations and 16 charges* | | | | |
| Si | 2·72 | 2·20 | 2·95 | 2·58 |
| Ti | 0·00 | 0·00 | 0·00 | 0·00 |
| Al | 1·25 | 1·68 | 1·07 | 1·37 |
| $Fe^{3+}$ | 0·00 | 0·02 | 0·00 | 0·01 |
| $Fe^{2+}$ | 0·01 | 0·00 | 0·01 | 0·00 |
| Mn | 0·00 | 0·00 | 0·00 | 0·00 |
| Mg | 0·00 | 0·00 | 0·00 | 0·00 |
| Ca | 0·32 | 0·86 | 0·11 | 0·46 |
| Na | 0·66 | 0·22 | 0·81 | 0·55 |
| K | 0·03 | 0·00 | 0·06 | 0·02 |
| Total | 5·00 | 5·00 | 5·00 | 5·00 |
| An | 31·75 | 79·29 | 17·55 | 58·74 |
| Ab | 64·94 | 20·43 | 74·02 | 39·02 |
| Or | 3·32 | 0·28 | 8·43 | 2·24 |

Rheological inversion occurs locally where granophyric magma is superheated by multiple replenishment events of mafic magma. Close to such rheologically inverse zones, mafic pillows emplaced into granophyre are only slightly chilled at their margins and, therefore, rheological inversion is thought to represent only a small-scale geometrical phenomenon. The intermediate and inner sections of the basal complex comprise zones of intense hybridization that display substantial textural variability on a metre scale. In the outer section, angular mafic clasts are predominantly separated from each other by small felsic veins with little movement of the mafic clasts (Fig. 2a). This is in sharp contrast to the mafic enclaves within the intermediate section, which are dislocated and have been transported by a hybrid crystal mush, suggesting different emplacement mechanisms. Zones of intense hybridization are interpreted to represent small feeder channels (~5–15 m in diameter) in which magma mingling and *in situ* mixing takes place. Variations in strain rate within these feeder channels may control the extent of hybridization. In areas with high strain rates small mafic enclaves are significantly stretched and incorporated along shear zones into the hybridized crystal mush (Fig. 2e). Increasing the surface area of the enclaves (as a result of stretching within magmatic shear zones) promotes diffusion of elements depending on the chemical gradients between the two melt compositions (De Campos *et al.*, 2011).

Mingling of felsic and mafic magmas represents the most common process at Austurhorn, whereas the transition between mingling and mixing can rapidly change on a small scale. In general, hybridization zones are extremely affected by magma mingling and subsequent mixing processes. Many researchers strictly refer to magma mixing when chemical exchange between two magmas occurs, whereas mingling reflects physical interaction and deformation processes (Flinders & Clemens, 1996). However, we suggest that chemical exchange is not restricted to mixing but can also occur in highly sheared hybridization zones owing to infinite stretching of enclaves in combination with enhanced diffusion. Outcrops consisting of several hybrid generations do not exhibit mingling textures, but rather indicate efficient mixing processes. This is also substantiated at a microscopic scale as the textures of hybrid rocks do not show mingling surfaces between the two magmas but are characterized by a chaotic distribution of minerals originating from both endmember rocks.

## Geochemical evolution of the Austurhorn rock series

*Compositional variations of the mafic and felsic endmembers*

In general, mafic rocks from the basal complex of the Austurhorn intrusion exhibit a rather broad range of geochemical variation ($Mg\# = 26–56$, $SiO_2 = 46–55$ wt %; Table 1). As *in situ* differentiation during emplacement of small-volume mafic sheets is not expected to represent an effective mechanism, the geochemical variation strongly points to injection of basaltic magmas that have already undergone fractional crystallization at deeper levels as previously suggested by Furman *et al.* (1992a,b). Except for one pillow sample, all rocks identified as mafic endmembers and mafic pillows follow a tholeiitic differentiation trend, most clearly illustrated in $TiO_2$, $Fe_2O_3$ and $Al_2O_3$ vs Mg# diagrams (Fig. 11a–c). Increasing $Fe_2O_3$, $TiO_2$ and $P_2O_5$ (Fig. 5h) with decreasing Mg# at fairly constant $SiO_2$ (Fig. 5c) and decreasing CaO and $Al_2O_3$ with decreasing Mg# are the typical features of a tholeiitic differentiation trend controlled by early olivine, plagioclase and clinopyroxene fractionation and delayed Fe–Ti-oxide saturation, most probably related to rather low $fO_2$ conditions (e.g. Tormey *et al.*, 1987; Villiger *et al.*, 2007). The presence of late amphibole and the relatively early clinopyroxene crystallization suggest that some $H_2O$ was present in the parental magmas (e.g. Feig *et al.*, 2006). Most of the mafic pillows are characterized, both macro- and microscopically, by chilled margins. The presence of chilled margins further indicates that the partially crystallized mafic magmas did not significantly interact (mechanically and/or chemically) with the magmas into which they intruded. Some mafic pillows are characterized by diffuse margins and trace element concentrations that are close to the evolved felsic endmember composition. The chemical similarity to felsic endmember concentrations may result from the incorporation of felsic magma-derived feldspar phenocrysts, where physical exchange was enhanced by the lack of a chilled outer surface between the mafic magma and the surrounding medium.

Chemical variations within felsic endmember rocks are exemplified by Ba, Sr and $K_2O$ concentrations when plotted against Th. The overall positive correlation between Ba and Th (Fig. 8a) clearly shows that the felsic rocks are characterized by a large spread, whereas the mafic rock samples are rather tightly clustered. Hybrid rocks plot on fans spreading out towards the felsic endmember Ba concentrations (Fig. 8a). The compositional variation in both the mafic and felsic endmembers is demonstrated when Ni is plotted against La (Fig. 12). Hybrid rocks plot on mixing lines (Fig. 12) between mafic magmas falling along a fractional crystallization trend and discrete differentiated felsic endmember compositions. The chemical variability within the felsic endmembers is also manifested in other elements, most prominently Zr, Sr and $K_2O$. The rather large range observed within the felsic rocks for Th, La and Zr (Table 1) suggests that significant internal differentiation by solid–liquid separation processes occurred within the felsic magmas. This might even have led to the formation of a magma reservoir that is composed of a (lower) layer enriched in crystals (crystal mush) and an (upper) layer enriched in liquids extracted

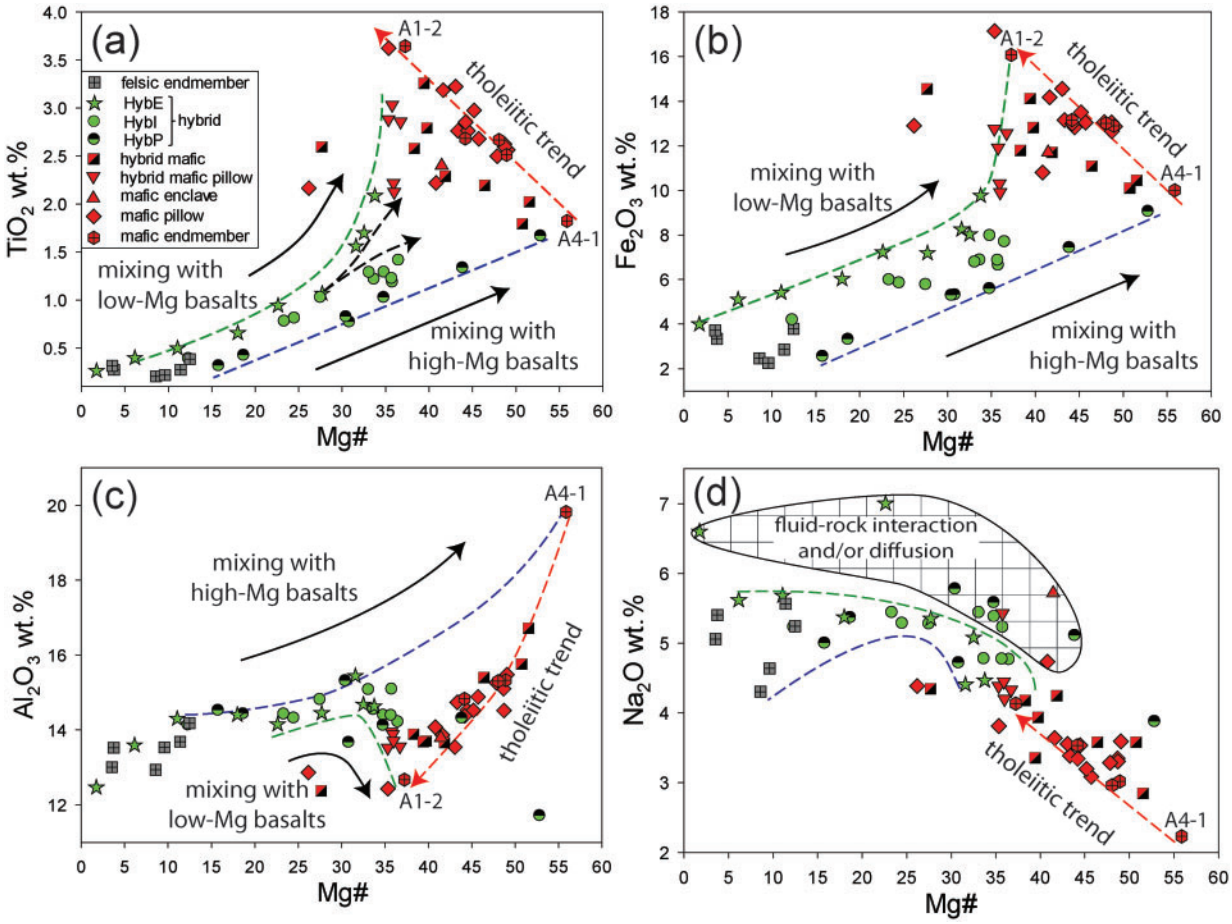


**Fig. 11.** Major element variation diagrams for the Austurhorn rocks. (a) $TiO_2$ vs Mg# including all rock types from the 'net-veined' complex. Mafic rocks display a tholeiitic trend characterized by increasing $Fe_2O_3$ and $TiO_2$ content with increasing differentiation. Magma mixing takes place between felsic endmember compositions and variably differentiated basalts resulting in two main trends of hybrid magmas. One mixing trend of hybrid rocks is characterized by increasing $TiO_2$ with increasing Mg# and suggests mixing between felsic magmas and Mg-rich basalts. In contrast, the second main mixing trend contains hybrids showing a hyperbolic increase in $TiO_2$ with increasing Mg#. The hybrid mixing trends clearly diverge towards the most primitive and most evolved mafic endmembers. It should be noted that hybrid rock samples have $TiO_2$ contents identical to those of felsic endmembers at low Mg#. (b) $Fe_2O_3$ vs Mg#. Hybrid rocks following the primitive mixing trend towards the high-Mg basalt endmember of the tholeiitic series show a positive linear correlation between $Fe_2O_3$ and Mg#. The low-Mg mixing trend in the hybrid rocks shows elevated $Fe_2O_3$ concentrations compared with the felsic rocks. Therefore, mixing of felsic and/or already existing hybrid magmas with Fe-rich more evolved members of the tholeiitic series is inferred. Hybrids plotting at $Fe_2O_3$ contents in the range between the two main distinguishable trends most probably result from mixing of hybrid magmas from each trend or mixing hybrids with intermediate composition differentiated basalts. (c) $Al_2O_3$ vs Mg#. Most hybrid rocks have higher $Al_2O_3$ contents than the felsic endmembers and mafic pillows, with the clear exception of mafic sample A4-l, which has a high $Al_2O_3$ content. Hybrid rocks plotting along the proposed high-Mg mixing trend exhibit increasing $Al_2O_3$ with increasing Mg#. Hybrid rocks following the more differentiated mixing trend first increase in $Al_2O_3$ at lower Mg# (<33) but then decrease significantly with increasing Mg#. The same relationship is observed for hybridized mafic pillows, which are inferred to act as the mafic mixing endmember for hybrids belonging to the low-Mg trend. Hybrid rocks plotting between the two main trends show $Al_2O_3$ contents that suggest mixing with more differentiated intermediate magmas or hybridized mafic basalts. (d) $Na_2O$ vs Mg# for felsic, hybrid and mafic rocks. Sodium contents exceeding those of both felsic and mafic endmember rocks cannot result from magma mixing and mingling alone, but require additional processes.

from the crystal mush and various mixtures of them entrained during extraction from the reservoir. Zr concentrations within the hybrid rocks do not clearly follow a mixing line between felsic and mafic compositions but rather point towards a possible missing felsic endmember as evident from Fig. 8e. The missing felsic endmember (at high Zr and Ba concentrations when extrapolating the mafic–hybrid mixing line; Fig. 8a, e) is most probably the crystal-rich part of the felsic intrusion containing zircon and Ba-rich feldspar that has been trapped by some hybrids mixing at lower levels of the magmatic system. The felsic endmembers that are exposed at the level of outcrop are therefore interpreted to represent extracted rhyolites from lower levels of the system.

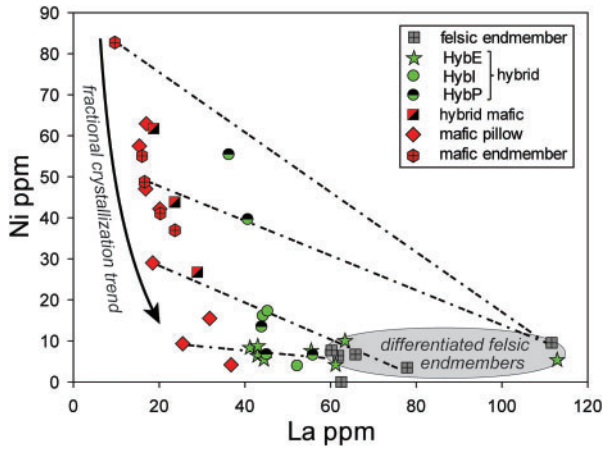


**Fig. 12.** Ni vs La (ppm) indicating the large chemical variability within the mafic and felsic endmember compositions. Hybrid rocks plot along mixing lines between mafic rocks defining a fractional crystallization trend and variably differentiated felsic endmembers.

### *Petrology of the different hybrid generations and their relative timing*

REE and major element concentrations, except most probably alkalis, are dominantly controlled by differentiation processes prior to mixing as well as by the mixing process itself. As shown previously, the REE are sensitive to differentiation, displaying rather different relative enrichments and patterns for the mafic and felsic rocks and exhibiting a continuum for the hybrid rocks that covers the compositional gap between the crystallization-derived endmember compositions.

For further evaluation of the mixing processes we separated the hybrid rocks into two distinct groups, one forming hybrid mafic pillows and a second group that is composed of more massive hybridization zones. Overall, the hybrid mafic pillows (Fig. 11a) within the inner section are characterized by Mg# ~36, higher $SiO_2$ contents and lower contents of MgO and CaO than the 'purely' basaltic pillows. The lower MgO and CaO contents of these hybridized mafic pillows indicate more extensive and prolonged interaction with felsic magmas. This interpretation is supported by the lack of chilled outer margins in these pillows, a feature that reflects lower thermal gradients and, thus, a potentially longer diffusion time. The physico-chemical interaction with felsic magma is also manifested in the REE patterns of the hybrid rocks, which exhibit a felsic signature compared with their mafic endmember. The felsic rocks have the largest negative Eu anomalies within the Austurhorn rock series, suggesting extensive plagioclase fractionation during their genesis (Fig. 6a). The negative Eu anomaly in the hybrid rocks is considerably smaller and the difference from the felsic rocks indicates the influence of mafic magma at the time of hybridization. Many incompatible elements such as Ba (Fig. 7a and b) substantiate the strong compositional similarities between the hybrids and the felsic rocks.

The hybrid mafic rocks characteristically display similarities to the endmember basalts; most of their major and trace elements are clearly controlled by variable degrees of fractionation of the basaltic magmas involved in the mixing process. Three hybrid mafic rock samples have low $TiO_2$, MnO and $Fe_2O_3$, but high MgO. The low concentrations of $TiO_2$, MnO and $Fe_2O_3$ suggest interaction with more primitive basaltic magmas that have experienced less clinopyroxene and plagioclase fractionation (Table 1). Other hybrid mafic rocks are characterized by higher $TiO_2$, $Fe_2O_3$ and MnO concentration, but lower contents of MgO and $Al_2O_3$ and are interpreted to result from interaction of more evolved tholeiitic basalts with felsic magmas. The chemical offset of the hybridized mafic rocks from the inferred tholeiitic liquid line of descent represents variable amounts of felsic liquids contained in the mixed products. During the interaction of the contrasting magmas both chemical mixing and diffusion processes along the interfaces are thought to take place rather than pure mechanical mingling. Diffusion and/or the presence of late-stage alkaline fluids are most probably responsible for $Na_2O$ concentrations in some mafic and hybrid rocks that even exceed the concentrations in the felsic magmas and clearly plot far outside any inferred mixing line between felsic and mafic endmembers (Fig. 11d). The scatter in $Na_2O$ within these hybrid rocks might be indicative of uphill diffusion, but we cannot *a priori* exclude a limited amount of late-stage fluid alteration that would, however, have affected only some hybrid rocks, but not the mafic rocks. Only the most fluid-mobile elements Na, Cs and Ba have potentially been affected by this process. Near-perfect linear correlations of LREE and Sr with Th, which is supposed to be fluid-immobile under most circumstances, testify to the robustness of the trace element dataset for most elements considered for evaluation of the mixing–mingling processes.

Hybrid rocks from the more massive hybridization zones (Fig. 3) have been separated into three groups based on the two major trends that are observed in Mg# variation diagrams (Fig. 11). The first trend (primitive hybrid rocks, HybP) is characterized by intermediate rocks showing higher Mg# and lower concentrations in $TiO_2$ for a given Mg# (Fig. 11a). These hybrid rocks are interpreted as the most 'primitive' hybrids. From 26 investigated hybrid rocks, seven samples are classified as 'primitive' hybrid rocks even though their $SiO_2$ contents can exceed 70 wt % at low Mg#. Hybrid rocks plotting along this linear or curvilinear HybP trend were most probably derived from mingling and subsequent mixing of granophyric magma with the least differentiated Mg-rich basalts. The second dominant geochemical trend (evolved

hybrid rocks, HybE) includes nine of the 26 analysed intermediate rock samples. This trend is dominated by more evolved hybrids that show a clear offset from the 'primitive' hybrid trend. The HybE hybrids are interpreted to result from mixing between felsic magmas and more differentiated basalts or with previously hybridized mafic pillows. Both hybrid trends start out as endmember mixing, but evolve with time into hybrid–hybrid interaction. Most hybrids that have lower concentrations of HREE plot along the 'evolved hybrid rock mixing trend in Mg# variation diagrams (Fig. 11). The petrogenesis of different hybrid generations evidently follows certain evolutionary patterns even if the REE show large internal variations suggesting complex mixing and mingling processes.

Ten hybrid rock samples do not follow either of the two discrete trends and do not result in linear relationships within variation diagrams. However, these hybrid rocks always display major element compositions within the bounds defined by the HybP and HybE trends. Therefore, these hybrid rocks are termed 'intermediate hybrid rocks' (HybI) and are interpreted to result from hybrid–hybrid mixing or originate from mixing hybrids with granophyric magmas. The remarkable range in $SiO_2$ within the hybrid rocks (58–73·4 wt %) indicates the complex petrogenetic processes and large chemical variability of the mingled and mixed rocks.

As discussed above, whole-rock and trace element chemistry allow the separation of the hybrid rocks into three types (HybP, HybE and HybI). The temporal and spatial relationships between these hybrid rock groups are crucial to delimit the intrusion and hybridization dynamics within the basal part of the Austurhorn intrusion. The distinct, variably differentiated mafic endmember rocks record systematic changes in the interaction with felsic magmas through time. This increasing interaction complexity over time is clearly recorded in the field relations. Only a minor degree of interaction between felsic and mafic magmas is recorded during the early stage, in which most mafic magmas display chilled rims at their contact with cooler felsic magmas. However, towards the centre of the intrusion, where numerous small mafic injections have occurred over a longer time span, the interaction dynamics between the mafic and felsic magmas are much more complex (probably as a direct result of a local temperature increase in the felsic magma owing to repeated mafic injections). The chemical signature of each of the three hybrid rock groups (HybP, HybE and HybI) not only displays their chemical affinity with their respective mafic endmembers but also yields further insights into the relative timing of hybridization events. The HybP rock samples (most primitive basaltic component) are interpreted to represent the early stage hybridization events where the least differentiated mafic magma interacted with a presumably larger volume of felsic, partially crystallized magma (Fig. 11). Hybrid rocks plotting along trends indicating mixing of felsic and low- to intermediate-Mg# basalts form the HybI and HybE groups (Fig. 11). With time, the mafic endmembers became more evolved, which is consistent with intermediate to more evolved hybrid rock compositions (HybI and HybE) relative to the mafic endmember (e.g. increased $TiO_2$ contents for a given Mg#).

### *A multiple endmember mixing scenario*

Exposed outcrops to the SE of Hvalnes lighthouse (Fig. 1) permit access to an entire cross-section of different hybrid generations enclosed by their felsic and mafic endmembers (Fig. 3). Some of these hybrid rocks do not display macroscopically identifiable contacts with their adjoining intermediate rocks, which either indicates a minimal thermal gradient between the two contrasting magmas at the time of intrusion or results from a short-term intrusion interval and subsequent mixing processes. The latter hypothesis implies mingling and mixing of hot mafic magma with a pre-existing hybrid, which was intruded and mixed shortly before that event (i.e. still in a partially molten state). In previous studies (Blake, 1966; Mattson *et al.*, 1986; Furman *et al.*, 1992b), hybrid rocks within the 'net-veined' complex were interpreted as being the products of 'pure' endmember magma mixing (i.e. granophyre mixed with basalt). However, the textures of contact zones, cross-cutting relationships between single hybrid generations in the field and their complex bulk and mineral geochemistry rather suggest multiple mingling and mixing of intruding mafic material with pre-existing, already hybrid magmas. Trace element variation diagrams (e.g. Th vs Ce; Fig. 13a) reveal a remarkably consistent clustering of hybrid samples at lower REE concentrations. The highest and lowest LREE concentrations of felsic and mafic endmember rocks are 11·1 and 0·6 ppm for Th and 233 and 22·4 ppm for Ce respectively. Intermediate rocks characteristically display concentrations ranging from 3·4 to 9·5 ppm for Th and from 89·7 to 135·1 ppm for Ce.

Below, we use simplified distribution coefficients $D_{\mathrm{bulk}(i)}$ to estimate the magma endmember mass fractions forming a particular hybrid magma generation:

$$D_{\mathrm{bulk}(i)} = \frac{1}{n}\sum_{i=1}^{n}\frac{C_{i\mathrm{m}}}{C_{i\mathrm{f}}} \tag{1}$$

where $C_{i\mathrm{m}}$ and $C_{i\mathrm{f}}$ represent the concentrations of an element $i$ in the mafic and felsic endmember, respectively.

Once distribution coefficients for the hybrid rocks are known, mixing ratios can be derived by the following steps:

$$C_{\mathrm{mh}}[\mathrm{ppm}_{(i)}] = C_{\mathrm{h}} \times D_{\mathrm{bulk}(i)} \tag{2}$$

and

$$C_{\mathrm{fh}} = C_{\mathrm{h}} - C_{\mathrm{mh}} \tag{3}$$

where $C_{\mathrm{fh}}$ is the felsic-derived concentration of element $i$ within the hybrid, $C_{\mathrm{mh}}$ is the mafic-derived concentration of

element $i$ within the hybrid and $C_h$ is the concentration of element $i$ in a particular hybrid rock sample.

The mixing ratio [equation (4)] of hybrid magmas is, therefore, simply the ratio of the proportions of mafic ($C_{mh}$) and felsic ($C_{fh}$) derived concentrations [equation (3)]:

$$\text{mixing ratio} = \frac{C_{mh}}{C_{fh}}. \quad (4)$$

All 16 hybrid rock samples used in this model were collected from the zone between the granophyres and the massive (~15 m width) mafic sheet at Hvalnes beach (Fig. 3). It is, thus, important to note that the mixing ratios based on the distribution coefficient calculations apply to only this location. This outcrop is interpreted as a feeding system near the centre of the intrusion and is, therefore, selected for investigating partitioning of trace elements during the mixing process.

The multi-endmember mixing model presented here is based on mixing of two endmember magmas, which are characterized by the most extreme concentrations in Th and Ce from all collected rock samples. The REE are chosen for applying this mixing model because these elements are much less susceptible to diffusion compared with the rather fast diffusion rates of, for example, the alkalis. Within the Austurhorn hybrid rock series chemical exchange processes (e.g. diffusion) affect only a few hybrid samples, pointing to uphill diffusion (Fig. 11d). Sample A4-1 is chosen as the mafic endmember and is set constant during all mixing calculations within this model. The magmatic evolution of the hybrid magmas initiates with the interaction of a pure felsic host and a freshly intruding mafic magma batch. After the formation of the first hybrid generation following mafic, small-volume intrusions, the hybrids became progressively more mafic in composition with time (Fig. 13a). To obtain correct mixing ratios for each hybrid generation, distribution coefficients for all REE have to be corrected for the felsic and, subsequently, for the hybrid magma compositions, which then act as possible mixing endmembers. Such corrections are achieved by considering the previously formed hybrid trace element concentration as $C_{if}$ in equation (1).

The mixing process starts with mixing basalt and a 'pure' granophyre (sample A5-5-2; Fig. 13a). The granophyre is later replaced by the different hybrids formed. Therefore, only the most REE-enriched hybrid sample (sample A7-11/1; Table 1) was used for pure endmember mixing between basaltic and granophyric magma. Distribution coefficients (Fig. 13b) and, thus, mixing ratios for all other hybrid rocks exhibiting progressively decreasing concentrations of REE (e.g. Ce) were determined by considering the next higher REE concentration hybrid sample as the new 'felsic' endmember.

The suggested mixing model for hybrid rock generations yields mixing ratios (mafic/felsic) ranging from 0·09 to 0·6 with respect to REE concentrations (Table 5). Distribution coefficient calculations suggest that 9–25% of the LREE incorporated in the hybrid magmas originated from the mafic magma during multiple endmember mixing. Similarly, the HREE contents also confirm the percentage of mafic magma derived concentrations with values ranging from 15 to 37%. Intermediate rocks collected from the 'net-veined' complex indicate a mean mafic magma proportion of ~25%. Thus, it is suggested that the hybrids of the Austurhorn intrusion formed by multiple small-volume intrusions of basaltic magma into an originally granophyric host reservoir that continuously

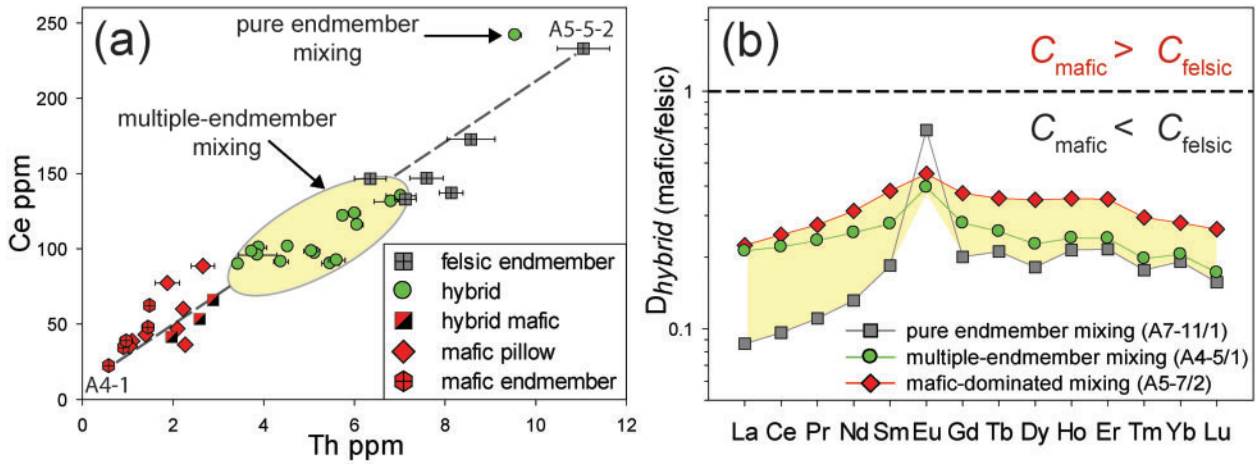


**Fig. 13.** (a) Ce vs Th (ppm) showing the variation in hybrid rock samples from the 'net-veined' complex. All hybrid rocks plot along an inferred mixing line between the felsic and the mafic endmembers. Only the most enriched hybrid rock sample (A7-11/1) is considered as a pure endmember mixing product. Data points within the shaded ellipse represent samples from multiple magma mixing events. (b) REE bulk partition coefficients between mafic and felsic magma for three hybrid rock samples, which are considered in the mixing model as products of pure-endmember mixing, multi-endmember mixing and late-stage mafic magma dominated magma mixing.

*Table 5: Mixing ratios and mass percentage of mafic magma derived from REE concentrations in hybrid rocks*

| REE | Pure endmember mixing | | Intermediate mixing stage | | Late-stage mixing | |
|---|---|---|---|---|---|---|
| | Mixing ratio | Mafic fraction (%) | Mixing ratio | Mafic fraction (%) | Mixing ratio | Mafic fraction (%) |
| La | 0·09 | 8·6 | 0·21 | 17·2 | 0·29 | 22·5 |
| Ce | 0·11 | 9·6 | 0·22 | 18·2 | 0·33 | 24·9 |
| Nd | 0·15 | 13·2 | 0·30 | 22·9 | 0·46 | 31·4 |
| Dy | 0·22 | 18·2 | 0·31 | 23·9 | 0·54 | 35·0 |
| Yb | 0·24 | 19·2 | 0·28 | 22·0 | 0·39 | 28·0 |

changed its composition by the mixing process, resulting in a system in which fresh basaltic magma mixed with pre-existing hybrids of a more and more 'basaltic' character over time.

## Constraints from mineral chemistry

The intrusion of basaltic magma into a granophyre reservoir results in disequilibrium features and mineral dissolution, reaction and overgrowth rims on pre-existing phenocryst and primocrysts (Streck, 2008). Detailed studies of mineral textures and their zoning patterns can, therefore, be employed to constrain the processes operating in open-system magma chambers (Eichelberger, 1975; Sato, 1975; Anderson, 1976; Humphreys *et al.*, 2006; Streck, 2008; Costa *et al.*, 2010). Here, we first discuss the observed mineral chemistry and zonation patterns that are subsequently utilized to identify discrete phenocryst populations that were subjected to similar thermal–geochemical histories.

### *Equilibrium and disequilibrium features in the phenocryst phases*

Normally, step-zoned clinopyroxene crystals within hybrid rocks may indicate open-system dynamics (e.g. Tomiya & Takahashi, 2005). Hybrid clinopyroxene often displays intense reaction and resorption at the crystal rim. These reaction textures are interpreted as disequilibrium features owing to chemical interaction between distinct magma compositions.

Most amphibole crystals display normal zoning; only in a few crystals is inverse zoning recorded. The wide range in Si (Fig. 10a) and Na content most probably reflects decreasing temperature with the higher Si amphiboles basically aligning along the edenite exchange vector at higher silica contents. Amphibole compositions plotting significantly below this trend towards lower Si contents for a given Na content are most probably additionally controlled by decreasing silica activity resulting in additional Tschermak's component in the amphibole consistent with their derivation from more mafic ($SiO_2$-poorer) basaltic and hybrid magmas.

Based on mineral chemistry, plagioclase zoning suggests the presence of at least three different mixing processes within the Austurhorn magma chamber, as follows.

Mixing of mafic and felsic magmas (Fig. 9b and c) is recorded in the plagioclase of groups 1 and 2. The stepwise, normally zoned phenocrysts of group 1 may record a progressively evolving melt composition with time, following a liquid line of descent in a (nearly) closed system. However, these zonation patterns could also reflect open-system mixing of a mafic magma with a more evolved melt at the late stage of crystallization. Based on field relations, we suggest that open-system mixing processes were responsible for at least some of the normally zoned plagioclase crystals within the hybrid rocks. Zonation patterns in group 2 are inferred to originate from mixing between hybrid and felsic magmas. The difference from group 1 is manifested by the composition of the crystal core ($An_{50–60}$), which has a lower An content than group 1 plagioclase, pointing towards previous interaction between mafic and more evolved melt compositions. Phenocrysts of group 2 often exhibit more than one mixing event in their zonation pattern.

Multiple mixing events between felsic, mafic and hybrid magmas (Fig. 9d) are manifested in group 3 plagioclases. The albitic cores suggest an origin from felsic magmas, which were mixed with mafic magmas (abrupt increase in An) before mixing with hybrid melts occurred. Reverse zoned plagioclase phenocrysts and resorption textures are evidence for reheating events in subvolcanic systems and have been reported from many mixed magmas (e.g. Eichelberger, 1978).

Many hybrid rocks contain strongly corroded plagioclase phenocrysts displaying disequilibrium textures and significant compositional scatter within a single profile. The An content of cores and crystal rims is not comparable with those of mafic and felsic plagioclase crystals (Table 4) and, therefore, mixing between different hybrid magmas (electronic appendix) is suggested to yield these intermediate compositions. Such chaotic zonation patterns, as well as the large variability of zonation patterns, strongly point towards complex mixing dynamics in the basal part of the Austurhorn magma chamber.

The endmember compositions of potassium feldspar and sodium feldspar within some mafic and hybrid rocks, respectively, necessitate additional explanation, other than simple minimum melt crystallization. Those feldspars recording extreme Ab or Or contents (Fig. 10b) may imply

additional subsolidus re-equilibration reaction between feldspar and high-temperature fluids (Słaby *et al.*, 2012).

### *Identification of different crystal populations using cross-correlation calculations*

In addition to kinetically controlled mineral zoning, changes in both chemistry and temperature, owing to recharge processes involving chemically distinct magmas, can lead to a superimposition of the original mineral zoning pattern (Ginibre *et al.*, 2002; Streck, 2008). Mingling of two chemically distinct magmas promotes chemical diffusion and homogenization of disequilibrium chemical gradients over time (Lesher, 2010; Zhang, 2010). The petrographic textures reveal that the phenocryst assemblages in the hybrid rocks are not in equilibrium with the resulting bulk-rock chemistry but rather suggest crystal growth (and partly dissolution) under significantly different chemical conditions. Here, plagioclase phenocrysts from hybrid rock samples are used for cross-correlation calculations with the aim of grouping plagioclases according to their zonation patterns. Diffusion processes may strongly influence the mineral zonation patterns and, therefore, the interpretation of single mineral phase populations can be challenging. The observed zonation patterns in thin sections strongly depend on the orientation of the two-dimensional cut and may lead to a misinterpretation of the growth history. Cross-correlation provides a helpful tool to avoid the impact of cutting effects on crystals by simple comparison of the integrated area of the overlapping zonation pattern accordance. The basic idea of identifying crystal populations using this method has already been introduced by Wallace & Bergantz (2005). However, our correlation method slightly differs from the cross-correlation approach used by Wallace & Bergantz (2005), which compensates for geometric distortions in zonation profiles and a maximization of the shared characteristic intervals between two cross-correlated crystals. Our method does not apply artificial stretching and reorientation of zonation profiles and is, therefore, thought to be better to constrain the original magmatic signatures. Both cross-correlation methods are based on the calculation of the correlation coefficients $R$ [equation (5)] by a moving window along the entire crystal length of plagioclase crystal A compared with a fixed reference crystal B. The chemical compositions of plagioclase phenocrysts analysed by electron microprobe were used and cross-correlated using equation (5), which allows the identification of mineral groups that have experienced similar crystallization histories:

$$R_{yx}(\tau) = \lim_{T\to\infty} \frac{1}{T} \int_{-T}^{T} y(t)x(t+\tau)\mathrm{d}t. \qquad (5)$$

The cross-correlation function measures the dependence of the values from one signal $x(t)$ on another signal $y(t)$; in the present case signals represent quantitative analysis of plagioclase profiles. $T$ is the record length (number of analysis points along the profile).

Based on cross-correlation calculations four main groups of plagioclase phenocrysts can be distinguished within the hybrid rocks at Austurhorn. Within each group (Fig. 14) crystals have experienced similar chemical evolution. The plotted curves in Fig. 14 represent best-fit reference cross-correlation profiles, which were used for grouping plagioclase phenocryst assemblages according to their zonation history. The majority (58%) of plagioclases in the hybrid rocks (Group A in Fig. 14) are interpreted to result from felsic and hybrid magma interaction, or by mixing hybrid magmas with a pre-existing hybrid generation. The second largest plagioclase group (19%; Group B) is characterized by high-An core compositions and more evolved melt compositions generating the crystal rims. This group is closely followed by phenocrysts (14%; Group C) recording mixing of mafic magma (An-rich cores) and hybridized melt compositions. Only 9% of all cross-correlation functions suggest mixing of hybrid or felsic magma-derived plagioclases with 'pure' mafic melts (Group D). These crystal zonation patterns record a late-stage event in which the inversely zoned crystals interact with a more felsic magma composition.

## Rheological constraints on the mingling and mixing processes

### *Rheology and the temperature window of magma mixing*

Hybridization owing to mingling and mixing processes in subvolcanic settings requires specific rheological conditions to allow the magmas to mix physically, which in turn allows for chemical interaction. The efficiency of magma mixing (or mingling) is dependent on several factors (e.g. Sparks & Marshall, 1986; Poli *et al.*, 1996; Jellinek *et al.*, 1999; Petrelli *et al.*, 2006), including the chemical composition of the two magmas, the temperature gradients between the interacting liquids, and the crystal fraction, which controls magma movement and its internal deformation and resistance to flow (viscosity). To allow mixing of two magmas their bulk or effective viscosities, considering melt plus crystals, need to be closely similar. Here, we present viscosity calculations based on bulk-rock compositions (Table 6) and the viscosity model of Giordano *et al.* (2008) computed at 1 kbar pressure. Melt compositions and crystal fractions as a function of temperature were computed with MELTS (basaltic endmember A7-24) and Rhyolite-MELTS (felsic endmember A5-8 and hybrid rocks A7-11/1 and A5-5/2) at a pressure of 1 kbar; initial $H_2O$ contents of the bulk magma varied from 1 to 3·5 wt %, equilibrium crystallization conditions were modelled and an $fO_2$ buffered at the fayalite–magnetite–quartz (FMQ) equilibrium was selected. Effective melt viscosities at a given temperature were calculated using the respective melt

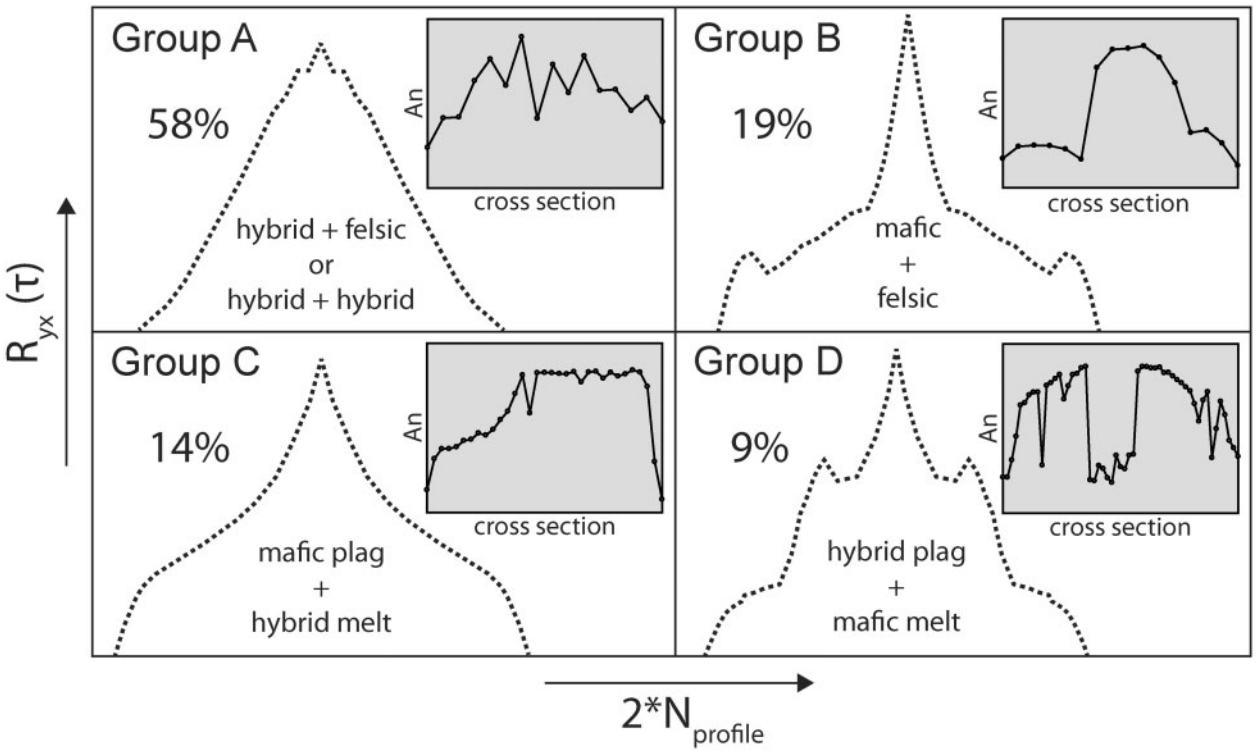


**Fig. 14.** Cross-correlation functions for plagioclase phenocrysts within hybrid rocks from the 'net-veined' complex. Cross-correlation calculations were conducted in MATLAB using electron microprobe data. The obtained functions show four major groups (Groups A–D), each consisting of several plagioclase phenocrysts. Each group is assigned to a certain type of mixing dynamics that is consistent with the observed mineral zonation patterns. Number of chemical analyses ($N$) on $x$-axis; cross-correlation factor on $y$-axis.

compositions obtained by the MELTS simulation, the calculated crystal fractions and the empirical, modified Einstein–Roscoe equation of Marsh (1981).

Anhydrous felsic endmember melt viscosities (0 wt % $H_2O$) range from $\sim 10^5$ to $10^{12}$ Pa s for a temperature range of 700–1200°C. On addition of 2–3 wt % $H_2O$ to dry rhyolite the melt viscosity decreases by 2·5–5·5 orders of magnitude (log $\eta$). For hybrid rock samples similar melt viscosities to felsic magmas are obtained with respect to changing $H_2O$ content and temperature. Anhydrous basaltic melt viscosities vary from $10^{11}$ to $3{\cdot}2 \times 10^2$ Pa s over the given temperature range. Introducing 2 wt % $H_2O$ to dry mafic endmember compositions yields melt viscosities in the range $10^6$ to 32 Pa s.

In the basal complex at Austurhorn, the hybrid rocks may have been generated by *in situ* mixing of felsic magma and a basaltic melt that was presumably hotter than the felsic host reservoir at the time of intrusion. Jellinek *et al.* (1999) proposed the mixing efficiency for such extreme viscosity contrasts between felsic and mafic melts to be almost zero. Large contrasts in temperature and viscosity between crystal-rich felsic magma and hotter, crystal-poor mafic magma would cause mingling rather than magma mixing (Murphy *et al.*, 2000). To find an appropriate temperature window (Fig. 15a and b) that allows mixing of basaltic and felsic magma in the basal complex of the Austurhorn intrusion, different volatile contents for each endmember were applied in both the melt viscosity and effective viscosity calculations, the latter taking into account the effect of changing melt composition and the crystal content on the viscosity of the bulk magma upon crystallization and cooling. The results of the pure melt viscosity modelling reveal that rhyolites containing 3–3·5 wt % $H_2O$ reach similar melt viscosities to their mafic counterparts (2–3 wt % $H_2O$) at temperatures around 900°C (Fig. 15a). This, however, would allow mixing of only the interstitial liquid (less than 20%) within the mafic magma with the nearly completely liquid felsic magma; this does not correspond to the mechanism we infer from the field evidence, where contrasting bulk magmas have mixed completely, not just their interstitial liquids. In contrast, the effective viscosities of both endmember magmas taking into account that the mafic magma will be highly crystallized close to the liquidus temperature of the felsic magma provides only a rather narrow temperature window (~1000°C) in which felsic and mafic magmas reach similar viscosities at lower volatile contents (Fig. 15b). The apparent gap at higher volatile concentrations results from the fact that we did not consider substantial superheating above the felsic magma

*Table 6: Melt viscosity and effective viscosity calculations for felsic, mafic and hybrid rocks as a function of temperature and $H_2O$ content at 1 kbar*

| Felsic (A5-8) | | | | Mafic (A7-24) | | | |
|---|---|---|---|---|---|---|---|
| *T* (°C) | φ | $\eta_{melt}$ (Pa s) | $\eta_{eff}$ (Pa s) | *T* (°C) | φ | $\eta_{melt}$ (Pa s) | $\eta_{eff}$ (Pa s) |
| *1 wt % $H_2O$* | | | | | | | |
| 1019 | 0·00 | $8·93 \times 10^4$ | $8·93 \times 10^4$ | 1134 | 0·00 | $4·99 \times 10^1$ | $5·00 \times 10^1$ |
| 1000 | 0·06 | $1·44 \times 10^5$ | $1·88 \times 10^5$ | 1100 | 0·17 | $1·31 \times 10^2$ | $3·07 \times 10^2$ |
| 950 | 0·19 | $5·55 \times 10^5$ | $1·43 \times 10^6$ | 1050 | 0·48 | $1·44 \times 10^3$ | $8·45 \times 10^4$ |
| 900 | 0·33 | $2·83 \times 10^6$ | $2·09 \times 10^7$ | 1000 | 0·62 | $8·83 \times 10^3$ | – |
| 850 | 0·53 | $1·19 \times 10^7$ | $2·61 \times 10^9$ | 984 | 0·65 | $1·51 \times 10^4$ | – |
| 800 | 0·66 | $4·76 \times 10^7$ | – | | | | |
| *1·5 wt % $H_2O$* | | | | | | | |
| 988 | 0·00 | $6·40 \times 10^4$ | $6·42 \times 10^4$ | 1102 | 0·09 | $6·42 \times 10^1$ | $9·50 \times 10^1$ |
| 950 | 0·09 | $1·57 \times 10^5$ | $2·56 \times 105$ | 1050 | 0·35 | $5·11 \times 10^2$ | $6·07 \times 10^3$ |
| 900 | 0·21 | $6·58 \times 10^5$ | $2·09 \times 10^6$ | 1000 | 0·52 | $3·06 \times 10^3$ | $7·18 \times 10^5$ |
| 850 | 0·35 | $3·62 \times 10^6$ | $4·03 \times 10^7$ | 952 | 0·62 | $1·40 \times 10^4$ | – |
| 800 | 0·52 | $1·40 \times 10^7$ | $1·98 \times 10^9$ | | | | |
| 763 | 0·78 | $2·04 \times 10^7$ | – | | | | |
| *2 wt % $H_2O$* | | | | | | | |
| 960 | 0·00 | $4·84 \times 10^4$ | $4·85 \times 10^4$ | 1099 | 0·05 | $4·37 \times 10^1$ | $5·48 \times 10^1$ |
| 950 | 0·03 | $6·10 \times 10^4$ | $6·83 \times 10^4$ | 1050 | 0·28 | $2·55 \times 10^2$ | $1·27 \times 10^3$ |
| 900 | 0·14 | $2·13 \times 10^5$ | $4·22 \times 10^5$ | 1000 | 0·45 | $1·42 \times 10^3$ | $4·40 \times 10^4$ |
| 850 | 0·26 | $1·16 \times 10^6$ | $4·73 \times 10^6$ | 950 | 0·62 | $7·09 \times 10^3$ | – |
| 800 | 0·41 | $5·00 \times 10^6$ | $8·87 \times 10^7$ | 904 | 0·81 | $4·65 \times 10^4$ | – |
| 750 | 0·90 | $5·17 \times 10^6$ | – | | | | |
| *2·5 wt % $H_2O$* | | | | | | | |
| 934 | 0·00 | $3·94 \times 10^4$ | $3·95 \times 10^4$ | 1090 | 0·00 | $3·74 \times 10^1$ | $3·74 \times 10^1$ |
| 900 | 0·08 | $8·77 \times 10^4$ | $1·27 \times 10^5$ | 1050 | 0·25 | $1·46 \times 10^2$ | $5·64 \times 10^2$ |
| 850 | 0·20 | $3·97 \times 10^5$ | $1·10 \times 10^6$ | 1000 | 0·39 | $7·18 \times 10^2$ | $9·65 \times 10^3$ |
| 800 | 0·31 | $2·09 \times 10^6$ | $1·26 \times 10^7$ | 950 | 0·62 | $3·84 \times 10^3$ | – |
| 754 | 0·87 | $1·80 \times 10^6$ | – | 900 | 0·82 | $2·77 \times 10^4$ | – |
| *3 wt % $H_2O$* | | | | | | | |
| 911 | 0·00 | $3·23 \times 10^4$ | $3·24 \times 10^4$ | 1094 | 0·00 | $2·85 \times 10^1$ | $2·85 \times 10^1$ |
| 900 | 0·02 | $4·12 \times 10^4$ | $4·56 \times 10^4$ | 1050 | 0·24 | $8·27 \times 10^1$ | $3·06 \times 10^2$ |
| 850 | 0·14 | $1·58 \times 10^5$ | $3·12 \times 10^5$ | 1000 | 0·40 | $4·82 \times 10^2$ | $7·39 \times 10^3$ |
| 800 | 0·27 | $8·65 \times 10^5$ | $3·89 \times 10^6$ | 950 | 0·63 | $2·33 \times 10^3$ | – |
| 750 | 0·89 | $1·07 \times 10^6$ | – | 904 | 0·81 | $1·28 \times 10^4$ | – |
| *3·5 wt % $H_2O$* | | | | | | | |
| 888 | 0·00 | $2·78 \times 10^4$ | $2·79 \times 10^4$ | | | | |
| 850 | 0·10 | $7·38 \times 10^4$ | $1·15 \times 10^5$ | | | | |
| 800 | 0·29 | $4·65 \times 10^5$ | $2·39 \times 10^6$ | | | | |
| 750 | 0·89 | $5·70 \times 10^5$ | – | | | | |

(continued)

*Table 6: Continued*

| Hybrid (A7-11/1) | | | | Hybrid (A5-5/2) | | | |
|---|---|---|---|---|---|---|---|
| $T$ (°C) | φ | $\eta_{melt}$ (Pa s) | $\eta_{eff}$ (Pa s) | $T$ (°C) | φ | $\eta_{melt}$ (Pa s) | $\eta_{eff}$ (Pa s) |
| *1 wt % $H_2O$* | | | | | | | |
| 1020 | 0·00 | $2{\cdot}31 \times 10^4$ | $2{\cdot}37 \times 10^4$ | 1104 | 0·00 | $1{\cdot}1 \times 10^3$ | $1{\cdot}1 \times 10^3$ |
| 1000 | 0·09 | $4{\cdot}06 \times 10^4$ | $5{\cdot}99 \times 10^4$ | 1050 | 0·13 | $4{\cdot}23 \times 10^3$ | $7{\cdot}7 \times 10^3$ |
| 950 | 0·28 | $2{\cdot}55 \times 10^5$ | $1{\cdot}24 \times 10^6$ | 1000 | 0·35 | $2{\cdot}66 \times 10^4$ | $2{\cdot}28 \times 10^5$ |
| 900 | 0·41 | $1{\cdot}67 \times 10^6$ | $2{\cdot}98 \times 10^7$ | 950 | 0·48 | $1{\cdot}31 \times 10^5$ | $7{\cdot}95 \times 10^6$ |
| 850 | 0·50 | $1{\cdot}15 \times 10^7$ | $1{\cdot}01 \times 10^9$ | 900 | 0·58 | $6{\cdot}52 \times 10^5$ | $4{\cdot}74 \times 10^9$ |
| 800 | 0·64 | $4{\cdot}80 \times 10^7$ | – | 850 | 0·66 | $3{\cdot}57 \times 10^6$ | – |
| 755 | 0·90 | $7{\cdot}22 \times 10^7$ | – | 800 | 0·72 | $2{\cdot}22 \times 10^7$ | – |
| | | | | 764 | 0·82 | $1{\cdot}36 \times 10^8$ | – |
| *1·5 wt % $H_2O$* | | | | | | | |
| 1000 | 0·00 | $1{\cdot}47 \times 10^4$ | $1{\cdot}48 \times 10^4$ | 1091 | 0·00 | $7{\cdot}21 \times 10^2$ | $7{\cdot}26 \times 10^2$ |
| 950 | 0·17 | $6{\cdot}91 \times 10^4$ | $1{\cdot}61 \times 10^5$ | 1050 | 0·04 | $1{\cdot}82 \times 10^3$ | $2{\cdot}12 \times 10^3$ |
| 900 | 0·32 | $3{\cdot}76 \times 10^5$ | $2{\cdot}51 \times 10^6$ | 1000 | 0·23 | $8{\cdot}74 \times 10^3$ | $2{\cdot}88 \times 10^4$ |
| 850 | 0·42 | $2{\cdot}15 \times 10^6$ | $4{\cdot}56 \times 10^7$ | 950 | 0·38 | $3{\cdot}88 \times 10^4$ | $5{\cdot}04 \times 10^5$ |
| 800 | 0·50 | $1{\cdot}36 \times 10^7$ | $1{\cdot}38 \times 10^9$ | 900 | 0·50 | $1{\cdot}65 \times 10^5$ | $1{\cdot}32 \times 10^7$ |
| 754 | 0·91 | $1{\cdot}76 \times 10^7$ | – | 850 | 0·58 | $7{\cdot}47 \times 10^5$ | $4{\cdot}34 \times 10^9$ |
| | | | | 800 | 0·71 | $5{\cdot}39 \times 10^6$ | – |
| | | | | 761 | 0·89 | $2{\cdot}95 \times 10^7$ | – |
| *2 wt % $H_2O$* | | | | | | | |
| 994 | 0·00 | $8{\cdot}07 \times 10^3$ | $8{\cdot}16 \times 10^3$ | 1080 | 0·00 | $5{\cdot}18 \times 10^2$ | $5{\cdot}22 \times 10^2$ |
| 950 | 0·08 | $2{\cdot}56 \times 10^4$ | $3{\cdot}62 \times 10^4$ | 1050 | 0·02 | $9{\cdot}71 \times 10^2$ | $1{\cdot}08 \times 10^3$ |
| 900 | 0·24 | $1{\cdot}21 \times 10^5$ | $4{\cdot}25 \times 10^5$ | 1000 | 0·14 | $3{\cdot}87 \times 10^3$ | $7{\cdot}34 \times 10^3$ |
| 850 | 0·35 | $6{\cdot}01 \times 10^5$ | $5{\cdot}55 \times 10^6$ | 950 | 0·30 | $1{\cdot}58 \times 10^4$ | $9{\cdot}34 \times 10^4$ |
| 800 | 0·44 | $3{\cdot}25 \times 10^6$ | $9{\cdot}09 \times 10^7$ | 900 | 0·43 | $6{\cdot}01 \times 10^4$ | $1{\cdot}34 \times 10^6$ |
| 754 | 0·91 | $6{\cdot}04 \times 10^6$ | – | 850 | 0·55 | $2{\cdot}67 \times 10^5$ | $1{\cdot}47 \times 10^8$ |
| | | | | 800 | 0·72 | $1{\cdot}99 \times 10^6$ | – |
| | | | | 765 | 0·81 | $1{\cdot}04 \times 10^7$ | – |
| *2·5 wt % $H_2O$* | | | | | | | |
| 995 | 0·00 | $4{\cdot}31 \times 10^3$ | $4{\cdot}32 \times 10^3$ | 1070 | 0·00 | $3{\cdot}91 \times 10^2$ | $3{\cdot}94 \times 10^2$ |
| 950 | 0·02 | $1{\cdot}20 \times 10^4$ | $1{\cdot}29 \times 10^4$ | 1050 | 0·02 | $5{\cdot}76 \times 10^2$ | $6{\cdot}17 \times 10^2$ |
| 900 | 0·16 | $4{\cdot}87 \times 10^4$ | $1{\cdot}08 \times 10^5$ | 1000 | 0·09 | $1{\cdot}99 \times 10^3$ | $2{\cdot}98 \times 10^3$ |
| 850 | 0·29 | $2{\cdot}15 \times 10^5$ | $1{\cdot}12 \times 10^6$ | 950 | 0·23 | $7{\cdot}46 \times 10^3$ | $2{\cdot}51 \times 10^4$ |
| 800 | 0·43 | $1{\cdot}26 \times 10^6$ | $3{\cdot}04 \times 10^7$ | 900 | 0·36 | $2{\cdot}64 \times 10^4$ | $2{\cdot}67 \times 10^5$ |
| 755 | 0·90 | $2{\cdot}41 \times 10^6$ | – | 850 | 0·55 | $1{\cdot}24 \times 10^5$ | $7{\cdot}1 \times 10^7$ |
| | | | | 800 | 0·72 | $8{\cdot}41 \times 10^5$ | – |
| | | | | 765 | 0·81 | $3{\cdot}99 \times 10^6$ | – |
| *3 wt % $H_2O$* | | | | | | | |
| 991 | 0·00 | $2{\cdot}75 \times 10^3$ | $2{\cdot}76 \times 10^3$ | 1064 | 0·00 | $2{\cdot}92 \times 10^2$ | $2{\cdot}94 \times 10^2$ |
| 950 | 0·02 | $6{\cdot}62 \times 10^3$ | $7{\cdot}07 \times 10^3$ | 1050 | 0·01 | $3{\cdot}86 \times 10^2$ | $4{\cdot}01 \times 10^2$ |
| 900 | 0·10 | $2{\cdot}26 \times 10^4$ | $3{\cdot}51 \times 10^4$ | 1000 | 0·08 | $1{\cdot}17 \times 10^3$ | $1{\cdot}65 \times 10^3$ |
| 850 | 0·23 | $9{\cdot}11 \times 10^4$ | $3{\cdot}06 \times 10^5$ | 950 | 0·17 | $3{\cdot}99 \times 10^3$ | $9{\cdot}03 \times 10^3$ |
| 800 | 0·43 | $5{\cdot}84 \times 10^5$ | $1{\cdot}40 \times 10^7$ | 900 | 0·35 | $1{\cdot}44 \times 10^4$ | $1{\cdot}36 \times 10^5$ |
| 750 | 0·96 | $1{\cdot}02 \times 10^6$ | – | 850 | 0·56 | $6{\cdot}51 \times 10^4$ | $5{\cdot}44 \times 10^7$ |
| | | | | 800 | 0·72 | $4{\cdot}11 \times 10^5$ | – |
| | | | | 764 | 0·83 | $1{\cdot}82 \times 10^6$ | – |

(continued)

*Table 6: Continued*

| Hybrid (A7-11/1) | | | | Hybrid (A5-5/2) | | | |
|---|---|---|---|---|---|---|---|
| $T$ (°C) | φ | $\eta_{melt}$ (Pa s) | $\eta_{eff}$ (Pa s) | $T$ (°C) | φ | $\eta_{melt}$ (Pa s) | $\eta_{eff}$ (Pa s) |
| *3·5 wt % $H_2O$* | | | | | | | |
| 987 | 0·00 | $1·83 \times 10^3$ | $1·84 \times 10^3$ | 1059 | 0·00 | $2·23 \times 10^2$ | $2·24 \times 10^2$ |
| 950 | 0·01 | $3·89 \times 10^3$ | $4·12 \times 10^3$ | 1050 | 0·01 | $2·63 \times 10^2$ | $2·7 \times 10^2$ |
| 900 | 0·04 | $1·16 \times 10^4$ | $1·37 \times 10^4$ | 1000 | 0·06 | $7·23 \times 10^2$ | $9·6 \times 10^2$ |
| 850 | 0·23 | $4·91 \times 10^4$ | $1·63 \times 10^5$ | 950 | 0·13 | $2·31 \times 10^3$ | $4·36 \times 10^3$ |
| 800 | 0·43 | $2·94 \times 10^5$ | $7·00 \times 10^6$ | 900 | 0·36 | $8·52 \times 10^3$ | $8·49 \times 10^4$ |
| 750 | 0·95 | $5·53 \times 10^5$ | – | 850 | 0·56 | $3·65 \times 10^4$ | $3·9 \times 10^7$ |
| | | | | 800 | 0·72 | $2·16 \times 10^5$ | – |
| | | | | 763 | 0·85 | $8·86 \times 10^5$ | – |

Liquidus temperature and solid fractions were derived from MELTS or Rhyolite-MELTS; melt viscosities were calculated with the model of Giordano *et al.* (2008); effective viscosities were calculated with the Einstein–Roscoe equation considering $R = 1·67$ (Marsh, 1981); φ, solid fraction; $\eta_{melt}$, melt viscosity in Pa s; $\eta_{eff}$, effective viscosity in Pa s.

liquidus, which is displaced to lower temperature with increasing $H_2O$ concentration. According to these results pure endmember mixing would be confined to mixing of crystal-poor felsic magma with mafic magma close to the rheologically critical melt fraction (for the modified Roscoe–Einstein equation this occurs at a crystal fraction of 60%). For higher $H_2O$ contents (>2·0 wt %) mixing would be possible between the pure endmembers only when the felsic magma is considerably superheated above its liquidus.

Higher volatile contents, in particular in the basaltic magma, would be possible only if the inferred emplacement depth of 1700 m (Walker, 1964, 1975; Blake, 1966) corresponding to a lithostatic pressure of ~0·5 kbar was increased to 1 kbar, because the maximum $H_2O$ contents for both the felsic and the mafic magmas are limited to about 2·0 wt % at 0·5 kbar (VolatileCalc, 100 ppm $CO_2$; Newman & Lowenstern, 2002). The suggested emplacement depth of 1700 m of the Austurhorn intrusion does not necessarily represent the formation depth of all the exposed hybrid rocks. If either the emplacement depth of the intrusion or the mixing horizon is set to ~3·5 km depth (1 kbar), then rheological inversion between mafic and felsic melts occurs, with overlapping of the solidus and liquidus of mafic and felsic magmas, respectively, because volatile contents of up to 3·5 wt % $H_2O$ (saturation at 1 kbar) in the melt phase decrease the mafic magma solidus to considerably lower temperatures (Fig. 15a).

The liquidus of $H_2O$-saturated (3·5 wt % $H_2O$) felsic melt at 1 kbar is ~890°C and the solidus of mafic magma at 1 kbar is around the same temperature (Fig. 15). However, multiple replenishment events of mafic magma batches into a partially crystallized felsic host reservoir cause reheating of the more viscous felsic magma (Murphy *et al.*, 2000). According to the effective viscosities of felsic and mafic melt compositions (Fig. 15b), the felsic magma must be locally superheated to temperatures up to ~1020°C, most probably owing to multiple replenishment events by hot mafic magma in the basal part of the Austurhorn magma chamber (as indicated by the observed field relations). Conduction is thought to be an efficient and relatively fast process transferring heat from mafic to felsic magma. Thermo-mechanical abrasion processes within the interacting magmas are thought to enhance heat exchange. Superheating of a hydrous felsic magma to such high temperatures decreases its effective viscosity and brings it up into the temperature range in which the crystallinity of the mafic magma is not yet too high to impede physical interaction. This facilitates magma mixing with basaltic liquids under the crystallinity conditions inferred from field relations (chilled margins of mafic intrusions). In summary, the rarely observed mixing of pure felsic and mafic endmembers that must constitute the initiation of more extensive mixing will occur only in specific areas within a magmatic system. This is likely to occur at the injection point on top of a feeding system where considerable volumes of mafic magma are injected into the host felsic reservoir over a short period of time, resulting in local superheating of the felsic magma. In terms of geographical location within the Austurhorn magmatic system we propose that the injection point of the feeder system is close to the Hvalnes outcrop (Figs 1 and 3).

According to the proposed multi-endmember mixing model, intruding mafic magmas preferentially interact with previously formed hybrids and thus approach with

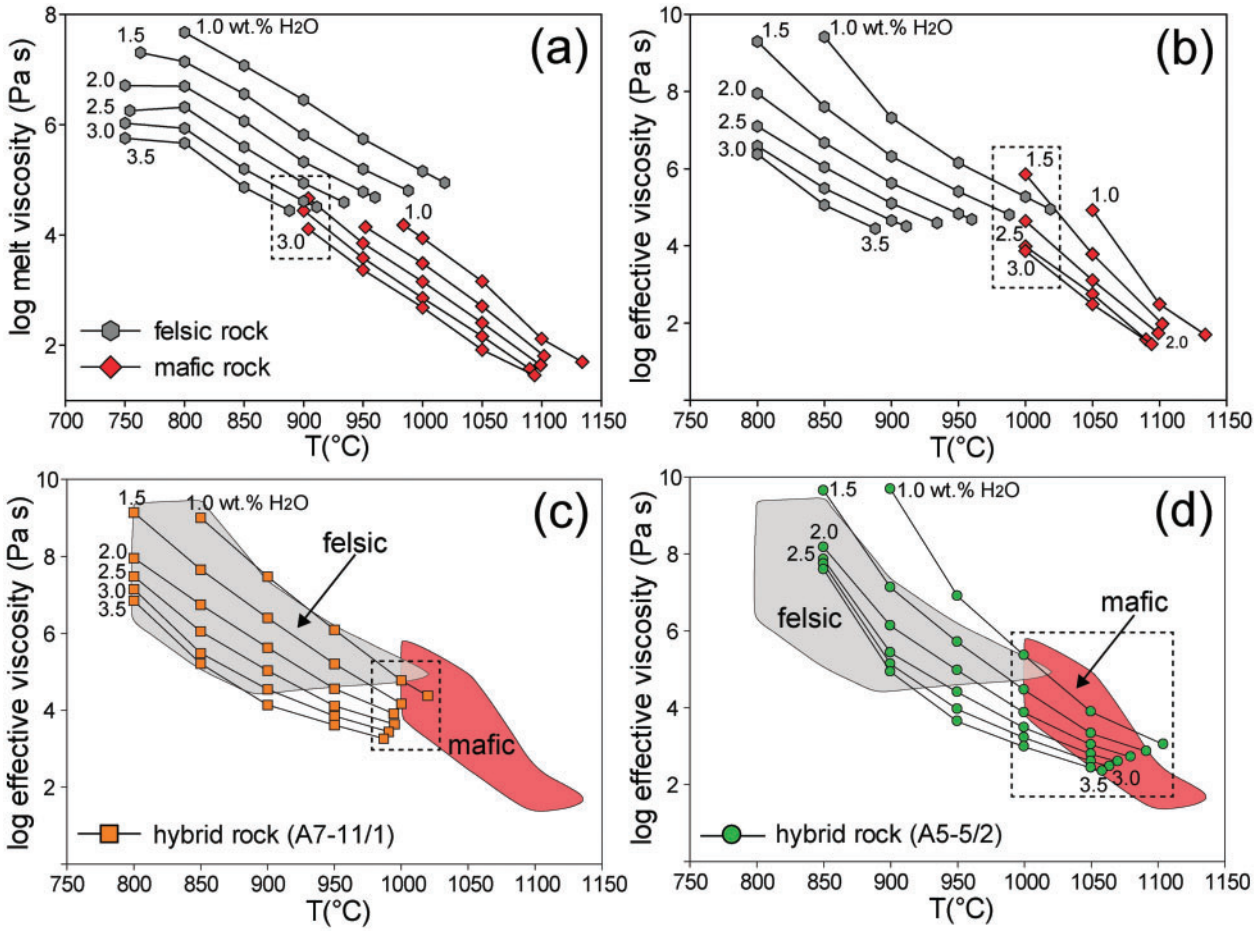


**Fig. 15.** Calculated melt and effective viscosity for felsic, mafic and hybrid rocks from the Austurhorn intrusion. (a) Melt viscosities calculated using the algorithm of Giordano *et al.* (2008) for one felsic (A5-8) and one mafic (A7-24) endmember with different $H_2O$ contents (1–3·5%), at a pressure of 1 kbar, as a function of temperature. Melt compositions and crystal fractions as a function of temperature were obtained using MELTS (mafic endmember) and Rhyolite-MELTS (felsic endmember) equilibrium crystallization calculations respectively. (b) Effective viscosity of both endmember systems calculated at 1 kbar and with variable $H_2O$ contents ranging from 1 to 3·5 wt % as a function of temperature. The effective viscosity was computed using the modified Einstein–Roscoe equation of Marsh (1981). (c) Effective viscosity of hybrid rock A7-11/1 for various $H_2O$ contents compared with the results for the mafic and felsic endmembers respectively. (d) Effective viscosity of hybrid rock A5-5/2 for various $H_2O$ contents compared with the results for the mafic and felsic endmembers respectively. Dashed rectangle represents the temperature- and viscosity-dependent mixing window.

time the mafic endmember composition. The effective viscosities computed for the hybrid rocks display rheological similarity to the felsic endmember, in agreement with the REE mixing model, which demonstrates that the hybrids have formed most probably by mixing small-volume mafic magma batches with a much larger volume of felsic magma (Fig. 15c). In contrast, late-stage hybridization within the Austurhorn magma chamber is characterized by hybrid effective viscosities that bridge felsic and mafic endmember viscosities at varying volatile contents (Fig. 15d). Owing to the larger overlap in the effective viscosities of the mafic and hybridized magmas, which are closer to the mafic endmember composition, the mixing efficiency increases significantly. Hybrids with more mafic compositions are furthermore characterized by lower viscosities than the pure mafic endmembers and, therefore, rheological inversion may occur. The formation of angular mafic blocks that lack chilled outer margins towards their surrounding hybridized matrix (Fig. 2d) are most probably the result of the increased mobility (lower viscosity than the pure mafic magma) of the hybridized magmas.

Our modelling results indicate that the hybrid magmas either formed at ~1 kbar pressure or at the pressure conditions suggested in the literature (0·5 kbar; Blake, 1966). In the latter case the felsic magmas must have been superheated to reach the inferred mixing window shown in Fig. 15a. Based on the observation that some hybrid rock generations contain both fine-grained mafic enclaves together with coarser-grained mafic and felsic enclaves (Fig. 3d and e), we suggest that these originate from

deeper mixing horizons than the hybrid rocks generated *in situ* within the basal part of the magma chamber. However, *in situ* mixing between felsic and mafic magma batches most probably occurs in small-volume feeder channels recording high strain rates, shear zones and elevated temperatures. The proposed multi-endmember mixing model is substantiated by the viscosity model. Within the basal complex of the Austurhorn intrusion the mixing efficiency increases with time when already hybridized magmas overlap the viscosity range of intruding mafic magmas.

## CONCLUSIONS

The basal part of the Austurhorn intrusion is characterized by a 'net-veined' complex consisting of felsic, mafic and hybrid rocks displaying evidence of complex physical emplacement dynamics. Based on field observations, the basal part of this exhumed intrusion is divided into three main sections: outer, intermediate and inner. Brittle deformation and 'net-veining' of mafic angular blocks by thin granophyre veins are observed in the outer section. The complexity of mingling and mixing dynamics increases considerably from the outer to the inner section of the intrusion where different cross-cutting hybrid generations are exposed between their felsic and mafic endmembers. Along the coast between the outer and inner section the large variability of mingling and mixing features is interpreted to represent small-volume feeding systems, which result in efficient *in situ* hybridization owing to high strain rates and deformation of the intruding mafic magma within the felsic host reservoir, combined with increased heat transfer from the mafic to the more felsic magma.

Mafic rocks display an increase in differentiation from voluminous mafic sheets to late-stage basaltic dykes that cross-cut the entire 'net-veined' complex. This broad geochemical variation results from fractional crystallization at deeper levels in the Austurhorn magmatic system followed by repeated injection of distinct, variably differentiated, small-volume mafic magma batches into the root zone of the magma chamber. Hybrid rocks cover the compositional gap between the felsic and mafic endmembers and are divided into three groups according to their whole-rock chemistry. These are denoted primitive (HybP), evolved (HybE) and intermediate (HybI) hybrid rocks. HybP rocks derived from mixing of the least differentiated mafic magma with felsic magma. The HybE group resulted from mixing of hybridized mafic magmas with felsic endmembers, and HybI compositions indicate physico-chemical interactions between different hybrid magma generations.

Distribution coefficient calculations are consistent with early stage hybrid magma generations formed by pure endmember mixing between felsic and mafic magma. The injection rate and, thus, the relative volume of mafic magma within the basal part of the magma chamber increased with time and mafic magmas interacted to a larger extent with pre-existing hybrids. Thus, the hybrid magma compositions are progressively shifted towards the mafic endmember composition with time and consist of a mean mafic magma proportion of ~25%.

These mixing processes are also recorded in the zonation patterns of plagioclase phenocrysts. According to cross-correlation calculations four main mixing processes can be distinguished. Cross-correlating the zonation patterns reveals that the majority (58%) of plagioclases within the hybrid rocks resulted from felsic–hybrid magma interaction, followed by a second group (19%) indicating mixing between mafic and felsic magma. The third group (14%) records magma mixing between mafic magmas containing plagioclase with hybridized melts. Only 9% of all cross-correlated plagioclase crystals suggest mixing of hybrids with pure mafic magmas.

Magma viscosity calculations indicate that magma mixing at Austurhorn most probably occurred at temperatures between 1000 and 1120°C and pressures equivalent to ~3·5 km depth. The initiation of the process (pure mafic–felsic endmember mixing) was possible only when the felsic magma was locally heated above its liquidus temperature in the early stage of hybridization. With time the hybrid magmas become more dominated by the mafic endmember composition with intermediate effective viscosities, which allowed magma mixing within a temperature window between 1000 and 1120°C. This implies that the continuous injection of mafic magma shifted the temperature of the felsic magma to higher values consistent with the generation of abundant, more mafic hybrid magmas over time.

## ACKNOWLEDGEMENTS

We gratefully acknowledge thoughtful and constructive reviews by Martial Caroff and Ewa Słaby, as well as additional comments from an anonymous reviewer and from the editor Gerhard Wörner.

## FUNDING

This study was carried out in preparation of a thesis for an MSc degree and was funded internally by the Institute of Geochemistry and Petrology, ETH Zurich.

## SUPPLEMENTARY DATA

Supplementary data for this paper are available at *Journal of Petrology* online.

## REFERENCES


Anderson, A. T. (1976). Magma mixing: petrological process and volcanological tool. *Journal of Volcanology and Geothermal Research* **1**, 3–33.

Anderson, F. J. (1949). Geological observations in south-eastern and central Iceland. *Transactions of the Royal Society of Edinburgh* **61**, 779–792.

Asimow, P. D. & Ghiorso, M. S. (1998). Algorithmic modifications extending MELTS to calculate subsolidus phase relations. *American Mineralogist* **83**, 1127–1131.

Bailey, E. B. (1959). Mobilization of granophyre in Eire and sinking of olivine in Greenland. *Liverpool and Manchester Geological Journal* **1**, 466–501.

Bailey, E. B. & McCallien, W. J. (1956). Composite minor intrusions, and the Slieve Gullion complex, Ireland. *Liverpool and Manchester Geological Journal* **2**, 143–154.

Blake, D. H. (1964). The volcanic geology of the Austurhorn area, southeastern Iceland. PhD thesis, Imperial College, London University, 191 p.

Blake, D. H. (1966). The net-veined complex of the Austurhorn intrusion, southeastern Iceland. *Journal of Geology* **74**, 891–907.

Blake, D. H., Elwell, R. W. D., Gibson, I. L., Skelhorn, R. R. & Walker, G. P. L. (1965). Some relationships resulting from the intimate association of acid and basic magmas. *Quarterly Journal of the Geological Society of London* **121**, 31–49.

De Campos, C. P., Perugini, D., Ertel-Ingrisch, W., Dingwell, D. B. & Poli, G. (2011). Enhancement of magma mixing efficiency by chaotic dynamics: an experimental study. *Contributions to Mineralogy and Petrology* **161**, 863–881.

Cargill, H. K., Hawkes, L. & Ledeboer, J. A. (1928). The major intrusions of south-eastern Iceland. *Quarterly Journal of the Geological Society of London* **84**, 505–539.

Costa, F., Coogan, L. A. & Chakraborty, S. (2010). The time scales of magma mixing and mingling involving primitive melts and melt–mush interaction at mid-ocean ridges. *Contributions to Mineralogy and Petrology* **159**, 371–387.

Eichelberger, J. C. (1975). Origin of andesite and dacite: Evidence of mixing at Glass Mountain in California and at other circum-Pacific volcanoes. *Geological Society of America Bulletin* **86**, 1381–1391.

Eichelberger, J. C. (1978). Andesitic volcanism and crustal evolution. *Nature* **275**, 21–27.

Eichelberger, J. C. (1995). Silicic volcanism: ascent of viscous magmas from crustal reservoirs. *Annual Review of Earth and Planetary Science* **23**, 41–63.

Elwell, E. W. D., Skelhorn, R. R. & Drysdall, A. R. (1962). Net-veining in the diorite of north-east Guernsey, Channel Islands. *Journal of Geology* **70**, 215–226.

Feig, S. T., Koepke, J. & Snow, J. E. (2006). Effect of water on tholeiitic phase equilibria: an experimental study under oxidizing conditions. *Contributions to Mineralogy and Petrology* **152**, 611–638.

Flinders, J. & Clemens, J. D. (1996). Nonlinear dynamics, chaos, complexity and enclaves in granitoid magmas. *Transactions of the Royal Society of Edinburgh: Earth Sciences* **87**, 217–223.

Furman, T., Frey, F. & Meyer, P. S. (1992*a*). Petrogenesis of evolved basalts and rhyolites at Austurhorn, southeastern Iceland: the role of fractional crystallization. *Journal of Petrology* **33**, 1405–1445.

Furman, T., Meyer, P. S. & Frey, F. (1992*b*). Evolution of Icelandic central volcanoes: evidence from the Austurhorn intrusion, southeastern Iceland. *Bulletin of Volcanology* **55**, 45–62.

Ghiorso, M. S. & Sack, R. O. (1995). Chemical mass transfer in magmatic processes. IV. A revised and internally consistent thermodynamic model for the interpolation and extrapolation of liquid–solid equilibria in magmatic systems at elevated temperatures and pressures. *Contributions to Mineralogy and Petrology* **119**, 197–212.

Ginibre, C., Kronz, A. & Woerner, G. (2002). High-resolution quantitative imaging of plagioclase composition using accumulated backscattered electron images; new constraints on oscillatory zoning. *Contributions to Mineralogy and Petrology* **142**, 436–444.

Ginibre, C., Wörner, G. & Kronz, A. (2007). Crystal zoning as an archive for magma evolution. *Elements* **3**, 261–266.

Giordano, D., Russel, J. K. & Dingwell, D. B. (2008). Viscosity of magmatic liquids: A model. *Earth and Planetary Science Letters* **271**, 123–134.

Gualda, G. A. R., Ghiorso, M. S., Lemons, R. V. & Carley, T. L. (2011). Rhyolite-MELTS: a modified calibration of MELTS optimized for silica-rich, fluid-bearing magmatic systems. *Journal of Petrology* **53**, 875–890.

Guillong, M., Meier, D. L., Allan, M. M., Heinrich, C. A. & Yardley, B. W. D. (2008). A MATLAB-based program for the reduction of laser ablation ICP-MS data of homogeneous materials and inclusions. In: Sylvester, P. (ed.) *Laser Ablation ICP-MS in the Earth Sciences: Current Practices and Outstanding Issues. Mineralogical Association of Canada, Short Course Series* **40**, 328–333.

Gunnarsson, B., Marsh, B. D. & Taylor, H. P., Jr (1998). Generation of Icelandic rhyolites: silicic lavas from the Torfajökull central volcano. *Journal of Volcanology and Geothermal Research* **83**, 1–45.

Humphreys, M. C. S., Blundy, J. D. & Sparks, R. S. J. (2006). Magma evolution and open-system processes at Shiveluch Volcano: insights from phenocryst zoning. *Journal of Petrology* **47**, 2303–2334.

Jakobsson, S. P. (1979). Petrology of recent basalts of the Eastern Volcanic Zone, Iceland. *Acta Naturalia Islandica* **26**, 1–138.

Jellinek, A. M., Kerr, R. C. & Griffiths, R. W. (1999). Mixing and compositional stratification produced by natural convection. 1. Experiments and their application to Earth's core and mantle. *Journal of Geophysical Research* **104**, 7183–7201.

Jónsson, J. (1954). Outline of the geology of the Hornafördur region. *Geografiska Annaler: Series A, Physical Geography* **36**, 146–161.

Kerr, A. C., Kent, R. W., Thomson, B. A., Seedhouse, J. K. & Donaldson, C. H. (1999). Geochemical evolution of the Tertiary Mull volcano, western Scotland. *Journal of Petrology* **40**, 873–908.

Lacasse, C., Sigurdsson, H., Carey, S. N., Jóhannesson, H., Thomas, L. E. & Rogers, N. W. (2007). Bimodal volcanism at the Katla subglacial caldera, Iceland: insights into the geochemistry and petrogenesis of rhyolitic magmas. *Bulletin of Volcanology* **69**, 373–399.

Le Maitre, R.W., Bateman, P., Dudek, A., Keller, J., Lameyre, J., Le Bas, M. J., Sabine, P. A., Schmid, R., Sorensen, H., Streckeisen, A., Woolley, A. R. & Zanettin, B. (1989). *A Classification of Igneous Rocks and Glossary of Terms*. Blackwell Scientific, pp. 130–171.

Lesher, C. E. (2010). Self-diffusion in silicate melts: theory, observations and applications to magmatic systems. In: Zhang, Y. & Cherniak, D. J. (eds) *Diffusion in Minerals and Melts. Mineralogical Society of America and Geochemical Society, Reviews in Mineralogy and Geochemistry* **72**, 269–309.

Leuthold, J., Müntener, O., Baumgartner, L. P. & Putlitz, B. (2014). Petrological constraints on the recycling of mafic crystal mushes and intrusion of braided sills in the Torres del Paine mafic complex (Patagonia). *Journal of Petrology* **55**, 917–949.

Marsh, B. D. (1981). On the crystallinity, probability of occurrence, and rheology of lava and magma. *Contributions to Mineralogy and Petrology* **78**, 85–98.

Martin, E., Paquette, J. L., Bosse, V., Ruffet, G., Tiepolo, M. & Sigmarsson, O. (2011). Geodynamics of rift–plume interaction in Iceland as constrained by new $^{40}Ar/^{39}Ar$ and *in situ* U–Pb zircon ages. *Earth and Planetary Science Letters* **311**, 28–38.

Mattson, S. R., Vogel, T. A. & Wilband, J. T. (1986). Petrochemistry of the silicic–mafic complexes at Vesturhorn and Austurhorn, Iceland: evidence for zoned/stratified magma. *Journal of Volcanology and Geothermal Research* **28**, 197–223.

Moorbath, S., Sigurdsson, H. & Goodwin, R. (1968). K–Ar ages of the oldest exposed rocks in Iceland. *Earth and Planetary Science Letters* **4**, 197–205.

Murphy, M. D., Sparks, R. S. J., Barclay, J., Carroll, M. R., Lejeune, A. M., Brewer, T. S., Macdonald, R., Black, S. & Young, S. (1998). The role of magma mixing in triggering the current eruption at the Soufrière Hills volcano, Montserrat, West Indies. *Geophysical Research Letters* **25**, 3433–3436.

Murphy, M. D., Sparks, R. S. J., Barclay, J., Carroll, M. R. & Brewer, T. S. (2000). Remobilization of andesite magma by intrusion of mafic magma at the Soufrière Hills volcano, Montserrat, West Indies. *Journal of Petrology* **41**, 21–42.

Newman, S. & Lowenstern, J. B. (2002). VolatileCalc: a silicate melt–$H_2O$ solution model written in Visual Basic for Excel. *Computers and Geosciences* **28**, 597–604.

Petrelli, M., Perugini, D. & Poli, G. (2006). Time-scales of hybridization of magmatic enclaves in regular and chaotic flow fields: petrologic and volcanologic implications. *Bulletin of Volcanology* **68**, 285–293.

Poli, G., Tommasini, S. & Halliday, A. N. (1996). Trace element and isotopic exchange during acid–basic magma interaction processes. In: *Geological Society of America Special Papers* **315**, 225–232.

Preston, R. J. (2001). Composite minor intrusions as windows into subvolcanic magma reservoir processes: mineralogical and geochemical evidence for complex magmatic plumbing systems in the British Tertiary Igneous Province. *Journal of the Geological Society, London* **158**, 47–58.

Rosenberg, C. L. & Handy, M. R. (2005). Experimental deformation of partially melted granite revisited: implications for the continental crust. *Journal of Metamorphic Geology* **23**, 19–28.

Sæmundsson, K. (1979). Outline of the geology of Iceland. *Jokull* **29**, 7–28.

Sato, H. (1975). Diffusion coronas around quartz xenocrysts in andesite and basalt from Tertiary volcanic region in north eastern Shikoku, Japan. *Contributions to Mineralogy and Petrology* **50**, 49–64.

Sisson, T. W., Grove, T. L. & Coleman, D. S. (1996). Hornblende gabbro sill complex at Onion Valley, California, and a mixing origin for the Sierra Nevada batholith. *Contributions to Mineralogy and Petrology* **126**, 81–108.

Słaby, E., Martin, H., Hamada, M., Smigielski, M., Domonik, A., Götze, J., Hoefs, J., Hałas, S., Simon, K., Devidal, J.-L., Moyen, J.-F. & Jayananda, M. (2012). Evidence in Archaean alkali feldspar megacrysts for high-temperature interaction with mantle fluids. *Journal of Petrology* **53**, 67–98.

Sparks, R. S. J. & Marshall, L. A. (1986). Thermal and mechanical constraints on mixing between mafic and silicic magmas. *Journal of Volcanology and Geothermal Research* **29**, 99–124.

Sparks, R. S. J., Sigurdsson, H. & Wilson, L. (1977). Magma mixing: a mechanism for triggering acid explosive eruptions. *Nature* **267**, 315–318.

Streck, M. J. (2008). Mineral textures and zoning as evidence for open system processes. In: Putirka, K. D. & Tepley, F. J., III (eds) *Minerals, Inclusions and Volcanic Processes. Mineralogical Society of America and Geochemical Society, Reviews in Mineralogy and Geochemistry* **69**, 595–622.

Sun, S.-s. & McDonough, W. F. (1989). Chemical and isotopic systematics of oceanic basalts: implications for mantle composition and processes. In: Saunders, A. D. & Norry, M. J. (eds) *Magmatism in the Ocean Basins. Geological Society, London, Special Publications* **42**, 313–345.

Thorarinsson, S. B. & Tegner, C. (2009). Magma chamber processes in central volcanic systems of Iceland: constraints from layered gabbro of the Austurhorn intrusive complex. *Contributions to Mineralogy and Petrology* **158**, 223–244.

Thoroddsen, Th. (1896). Fra det sydostlige Island. *Geografisk Tidskrift (Copenhagen)* **13**, 3–37.

Tomiya, A. & Takahashi, E. (2005). Evolution of the magma chamber beneath Uso volcano since 1663: a natural laboratory for observing changing phenocryst compositions and textures. *Journal of Petrology* **46**, 2395–2426.

Tormey, D. R., Grove, T. L. & Bryan, W. B. (1987). Experimental petrology of normal MORB near the Kane Fracture Zone: 22°–25°N, mid-Atlantic ridge. *Contributions to Mineralogy and Petrology* **96**, 121–139.

Turnbull, R., Weaver, S., Tulloch, A., Cole, J., Handler, M. & Ireland, T. (2010). Field and geochemical constraints on mafic–felsic interactions, and processes in high-level arc magma chambers: an example from the Halfmoon Pluton, New Zealand. *Journal of Petrology* **51**, 1477–1505.

Villiger, S., Müntener, O. & Ulmer, P. (2007). Crystallization pressures of mid-ocean ridge basalts derived from major element variations of glasses from equilibrium and fractional crystallization experiments. *Journal of Geophysical Research* **112**, 1–18.

Wager, L. R. & Bailey, E. B. (1953). Basic magma chilled against acid magma. *Nature* **172**, 68–69.

Walker, G. P. L. (1960). Zeolite zones and dike distribution in relation to the structure of the basalts of Eastern Iceland. *Journal of Geology* **68**, 515–528.

Walker, G. P. L. (1963). The Breiddalur central volcano, eastern Iceland. *Quarterly Journal of the Geological Society of London* **119**, 29–63.

Walker, G. P. L. (1964). Geological investigation in eastern Iceland. *Bulletin of Volcanology* **27**, 3–15.

Walker, G. P. L. (1974). The structure of eastern Iceland. In: Kristjannson, L. (ed.) *Geodynamics of Iceland and the North Atlantic Area*. Reidel, pp. 177–188.

Walker, G. P. L. (1975). A new concept of the evolution of the British Tertiary intrusive centres. *Journal of the Geological Society, London* **131**, 121–141.

Wallace, G. S. & Bergantz, G. W. (2005). Reconciling heterogeneity in crystal zoning data: An application of shared characteristic diagrams at Chaos Crags, Lassen Volcanic Center, California. *Contributions to Mineralogy and Petrology* **149**, 98–112.

Wiebe, R. A. (1996). Mafic–silicic layered intrusions: the role of basaltic injections on magmatic processes and the evolution of silicic magma chambers. *Transactions of the Royal Society of Edinburgh: Earth Sciences* **87**, 233–242.

Zellmer, G. F., Rubin, K. H., Grönvold, K. & Jurado-Chichay, Z. (2008). On the recent bimodal magmatic processes and their rates in the Torfajökull–Veidivötn area, Iceland. *Earth and Planetary Science Letters* **269**, 388–398.

Zhang, Y. (2010). Diffusion in minerals and melts: theoretical background. In: Zhang, Y. & Cherniak, D. J. (eds) *Diffusion in Minerals and Melts. Mineralogical Society of America and Geochemical Society, Reviews in Mineralogy and Geochemistry* **72**, 5–59.